High-Voltage-Stress Induced Degradation and Radiation Response of GaN-Based HEMTs

By

Pengfei Wang

Dissertation

Submitted to the Faculty of the

Graduate School of Vanderbilt University

in partial fulfillment of the requirements

for the degree of

DOCTOR OF PHILOSOPHY

in

Electrical Engineering

May 31, 2021

Nashville, Tennessee

Approved:

Daniel M. Fleetwood, Ph.D.

En Xia Zhang, Ph.D.

Ronald D. Schrimpf, Ph.D.

Robert A. Reed, Ph.D.

Sokrates Pantelides, Ph.D.

Copyright © 2021 by Pengfei Wang
All Rights Reserved

ACKNOWLEDGEMENTS

First and foremost, I would like to thank my advisor, Prof. Daniel M. Fleetwood, for his invaluable guidance in my academic growth and research pursuits. His profound knowledge and religious research attitude inspire me. It would be impossible to get my PhD degree without his support. I would also like to thank Prof. Ronald D. Schrimpf for sharing his deeply understanding in semiconductor device physics through the countless discussions on my research. I consider myself especially indebted to Prof. En Xia Zhang for her boundless support to my work. She is patient and always there to help. I would thank Prof. Robert A. Reed and Prof. Sokrates Pantelides for all the helpful discussions in our group meetings.

I would like to thank my colleagues in the Radiation Effects and Reliability group, including lots of them who have already graduated, for their valuable suggestions and friendship. Thank you to collaborators from the Air Force Research Laboratory, Dr. Brian S. Poling and Dr. Eric R. Heller. I would also like to thank Air Force Research Laboratory and Air Force Office of Scientific Research through the Hi-REV program and the Defense Threat Reduction Agency through its Basic Research program for supporting this work.

At last, I would like to express my thanks to my wife, Shuang Xie, and our parents for their unconditional love and support.

TABLE OF CONTENTS

ACKNOWLEDGEMENTS .... **iii**

LIST OF FIGURES .... **vi**

LIST OF TABLES .... **xi**

Chapter I. Introduction **1**

1.1 Wide Bandgap Semiconductors 1
1.1.1 History 1
1.1.2 Applications 2

1.2 Properties of GaN 4
1.2.1 Crystal structure 4
1.2.2 Electron velocity field relationship 6
1.2.3 Polarization effect 7

1.3 Overview of dissertation 10

Chapter II. HEMT **11**

2.1 History and basic structure 11

2.2 Formation mechanisms of 2DEGs 12

2.3 Advantages of InAlN/GaN HEMT 15

2.4 Models of electrical degradation 16

Chapter III. Radiation effects and low frequency noise **19**

3.1 Radiation effects 19
3.1.1 Total ionizing dose 19
3.1.2 Displacement damage 22

3.2 Low frequency noise 23

Chapter IV. High voltage stress of GaN HEMTs **25**

4.1 Experimental details 25

4.2 Experimental results and analysis 29
4.2.1 Stepped drain-bias stress 29
4.2.2 Elevated-temperature stress 35

4.3 Conclusions 40

Chapter V. Radiation response of GaN-based HEMTs **41**

5.1 Experimental details 41

5.2 Experimental results and analysis 44
5.2.1 Radiation response 44
5.2.2 Bias-stress effects in InAlN/GaN HEMTs 50

5.2.3 Combined high-field stress and irradiation 52
5.3 Conclusions 55
Chapter VI. Low frequency noise of GaN-based HEMTs 56
6.1 Temperature dependent noise results and discussion 56
6.2 Gate-voltage dependent noise results and discussion 65
6.3 Conclusions 69
Chapter VII. Conclusions 70
References 72

LIST OF FIGURES

Fig. 1-1. SiC device application requirements and market size (after [6]). 3

Fig. 1-2. GaN device application requirements and market size (after [6])............................... 3

Fig. 1-3. Two crystal structures of GaN: (a) wurtzite and (b) zinc-blende (after [8]). 5

Fig. 1-4. Temperature dependence of electron Hall mobility for GaN with a background ionized impurity concentration of 10^{17} cm^{-3} (after [12]). 6

Fig. 1-5. Electron drift velocity as a function of applied electric field for GaN with a background ionized impurity concentration of 10^{17} cm^{-3} (after [13])....................................... 7

Fig. 1-6. Schematic structure of hexagonal wurtzite GaN with different polarities (after [14]).. 9

Fig. 1-7. Surface charges and direction of internal electric field and polarization filed for spontaneous and piezoelectric polarization in III-nitrides for Ga- and N-face orientation (after [18]). 9

Fig. 1-8. (A) Device structure schematic, and (B) band diagram of heterostructure showing different types of charges (after [6]). 10

Fig. 2-1. Energy band diagram as proposed by Dr. Takashi Mimura (after [21])..................... 12

Fig. 2-2. Basic cross section of a HEMT device (after [25]).. 12

Fig. 2-3. Energy band of AlGaN/GaN heterojunction as a function of AlGaN layer thickness. The donor-like surface state is at the level E_{DS} (after [26])..................................... 14

Fig. 2-4. (a) Bandgap as a function of the lattice constant, and (b) lattice-matched InAlN/GaN heterostructure (after [11]). 16

Fig. 2-5. Schematic of inverse piezoelectric effect (after [35]). 18

Fig. 2-6. The transmission electron microscope image of the drain-side edge of the gate after experiencing strong electric field (after [36]). 18

Fig. 3-1. Schematic energy band diagram for a MOS device under positive bias, indicating

major physical processes for radiation induced charge generation (after [38]). 21

Fig. 3-2. Drain current vs. gate voltage for the CGH40006P as a function of total ionizing dose using 10 keV X-rays up to a dose of 1 Mrad(SiO_2). Note a negative shift in threshold voltage. This plot shows the worst-case threshold voltage shift of the two Cree devices tested for TID. The arrow indicates the direction in increasing radiation (after [44]). 21

Fig. 3-3. Spatial distribution of the initial defect configuration to the primary knock-on atom energy in Si material (after [46]). 22

Fig. 3-4. Schematic variation of S_V with frequency (after [53]). 23

Fig. 3-5. Excess voltage noise power spectral density S_{vd} (corrected for background noise) as a function of frequency for AlGaN/GaN HEMTs at 300 K. $V_{gs} - V_{th} = 0.5$ V, and $V_{ds} =$ 0.05 V. 24

Fig. 4-1. (a) Wolfspeed CGH40010F GaN HEMT; (b) test board. 26

Fig. 4-2. Agilent B1505A power device analyzer. 27

Fig. 4-3. Test Equity model 140 temperature chamber. 28

Fig. 4-4. $I_d - V_d$ curves for a representative Wolfspeed GaN HEMT. 29

Fig. 4-5. (a) $I_d - V_d$ curves for AlGaN/GaN HEMTs at V_d = 500mV before and after the OFF-state bias stressing sequence for which (b) threshold-voltage shift and (c) peak transconductance G_M normalized to the value for an unstressed device for a series of drain biases up to 100 V and gate bias of −4 V (OFF state). For drain biases of 30 V to 100 V, the device was stressed for one h for an additional step increment of 2V additional bias on the drain. No temperature change occurs during these OFF-state bias stresses. 31

Fig. 4-6. Threshold-voltage shift (left y-axis) and peak transconductance normalized to that of an unstressed device (right y-axis) for Group A devices stressed sequentially at 10 V, 15 V, and 20 V drain bias and −1.5 V gate bias (ON state) in room ambient without temperature control. The package temperature is 56 ^oC when devices are stressed at the maximum drain bias of 20 V ($I_d \sim 0.83$ A). DC measurements are performed at room temperature after devices are cooled for ~ 30 min. 32

Fig. 4-7. Threshold-voltage shift (left y-axis) and peak transconductance normalized to that

of an unstressed device (right y-axis) for Group B devices stressed at 30 V drain bias (I_d ~ 1.25 A) and −0.5 V gate bias (ON state) at a package temperature of 20 °C. DC measurements are performed at 20 °C. 33

Fig. 4-8. Threshold-voltage shift (left y-axis) and peak transconductance normalized to that of an unstressed device (right y-axis) for Group A devices stressed sequentially at drain biases up to 40 V and −2.5 V gate bias (semi-ON state) in room ambient without temperature control. The package temperature is 46 °C when devices are stressed at the maximum drain bias of 40 V (I_d ~ 0.16 A). DC measurements are performed at room temperature after devices are cooled for ~ 30 min. 34

Fig. 4-9. (a) $I_d – V_g$ curves for AlGaN/GaN HEMTs at V_d = 50 mV before and after OFF-state bias stressing at a package temperature of 125 °C. Also shown are (b) threshold-voltage shift (left y-axis) and peak transconductance normalized to that of an unstressed device (right y-axis) for Group B devices stressed at 80 V drain bias (I_d ~ 60 μA) and -4 V gate bias (OFF state) at a package temperature of 125 °C. DC measurements are performed at 27 °C after devices are cooled for ~ 30 min. 36

Fig. 4-10. (a) $I_d – V_g$ curves for AlGaN/GaN HEMTs at V_d = 50 mV before and after ON-state bias stressing at a package temperature of 79 °C. Also shown are (b) threshold-voltage shift (left y-axis) and peak transconductance normalized to that of an unstressed device (right y-axis) for Group B devices stressed at 30 V drain bias (~7% above rated operating voltage limits; I_d ~ 1.1 A) and −0.5 V gate bias (ON state) at a package temperature of 79 °C. DC measurements are performed at 27 °C after devices are cooled for ~ 30 min. The dashed lines in Fig. 4-10(b) indicate points in the stressing sequence where noise measurements are performed, as discussed in Chapter VI. 37

Fig. 4-11. V_{th} shift (left y-axis) and peak transconductance normalized to that of an unstressed device (right y-axis) for Group B devices stressed at 30 V drain bias (I_d ~ 1.12 A) and −0.5 V gate bias (ON state) at a package temperature of 105 °C. DC measurements are performed at 27 °C after devices are cooled for ~ 30 min. 39

Fig. 4-12. (a) $I_d – V_g$ curves for AlGaN/GaN HEMTs at V_d = 50 mV before and after semi-ON state bias stressing at a package temperature up to 125 °C. Also shown are (b)

threshold-voltage shift (left y-axis) and peak transconductance normalized to that of an unstressed device (right y-axis) for Group B devices stressed sequentially at drain biases up to 40 V (30% above rated voltage limits) with −2.5 V gate bias (semi-ON state) at a package temperature up to 125 °C. I_d ~ 228 mA at 125 °C. DC measurements are performed at 27 °C after devices are cooled for ~ 30 min. 40

Fig. 5-1. Schematic diagram of InAlN/GaN HEMT structures (After [96]). 42

Fig. 5-2. 10-keV ARACOR 4100 X-ray irradiator. 43

Fig. 5-3. Pelletron accelerator at Vanderbilt University. 43

Fig. 5-4. I_d-V_g curves for (a) the CGH 40006P and (b) CGH 40010F AlGaN/GaN HEMTs before and after X-ray irradiations with all pins grounded. 45

Fig. 5-5. Comparison of (a) threshold voltage shifts and (b) peak G_M normalized to the value of an unirradiated device as a function of TID and annealing time for CGH40006P and CGH40010F GaN-based HEMTs. 46

Fig. 5-6. I_d–V_g curves at V_d = 0.5 V for InAlN/GaN HEMTs before and after X-ray irradiation up to 1 Mrad(SiO_2) with all pins grounded. 47

Fig. 5-7. I_d-V_g curves for (a) CGH40006P and (b) CGH40010F GaN-based HEMTs before and after 1.8-MeV proton irradiation up to a fluence of 10^{14}/cm^2 with all pins grounded. 48

Fig. 5-8. (a) V_{th} shifts and (b) normalized peak transconductance as a function of proton fluence CGH40006P and CGH40010F GaN-based HEMTs before and after 1.8-MeV proton irradiation up to 10^{14}/cm^2 with all pins grounded. 49

Fig. 5-9. (a) V_{th} shifts and (b) normalized peak G_M vs. time for InAlN/GaN HEMTs stressed under ON (V_{gs} = 1 V), Semi-ON (V_{gs} = -3 V), and OFF (V_{gs} = -5 V) conditions (V_{ds} = 20 V). Post-stress annealing was performed at room temperature with all pins grounded. Error bars represent the standard deviations of the responses of identical devices. 51

Fig. 5-10. (a) Threshold voltage shifts and (b) normalized peak transconductance of InAlN/GaN HEMTs as a function of time during high field stress and irradiation. Devices are first stressed and then irradiated for biases of V_{ds}= 8 V and V_{gs} = 1 V. 53

Fig. 5-11. (a) Threshold voltage shifts and (b) normalized peak G_M of InAlN/GaN HEMTs

as a function of irradiation and time during high field stress. Devices are first irradiated and then stressed at biases of V_{ds}= 8 V and V_{gs} = 1 V. 54

Fig. 6-1. Low frequency noise measurement system. 56

Fig. 6-2. Excess voltage noise power spectral density S_{vd} (corrected for background noise) as a function of frequency for the AlGaN/GaN HEMTs before and after ON state bias stress at 300 K. $V_{gs} - V_{th}$ = 0.5 V, and V_{ds} = 0.05 V. 57

Fig. 6-3. Temperature dependence of (a) threshold voltage and (b) peak transconductance for AlGaN/GaN HEMTs before and after 39 hours under ON-state bias stress conditions. 59

Fig. 6-4. Normalized excess drain-voltage noise $S_V f/T$ from 85 K to 400 K, for f = 30 Hz. Here $V_{gs} - V_{th}$ = 0.5 V, V_d = 0.05 V. The temperature range corresponds to an activation energy scale on the upper x-axis derived from Eq. (6.4). The stress bias conditions are (a) OFF state, (b) ON state and (c) semi-ON state. 62

Fig. 6-5. Experimental (from Eq. (6.1)) and calculated (from Eq. (6.2)) frequency exponents α for (a) unstressed devices and (b) devices stressed in the ON state, verifying the applicability of the Dutta-Horn model in these cases. Similar agreement between measured and calculated values of α were observed for all tested devices in this study. 63

Fig. 6-6. S_{Vd} as a function of f for (a) CGH 40006P and (b) CGH 40010F GaN-based HEMTs before and after proton irradiation up to 1 x 10^{14}/cm^2 with all pins grounded. $V_g - V_{th}$ = 0.5 V, and V_d = 0.05 V during the noise measurements. 66

Fig. 6-7. S_{Vd} at 30 Hz as a function of $V_g - V_{th}$ for (a) CGH 40006P and (b) CGH 40010F GaN-based HEMTs before and after proton irradiation up to 10^{14}/cm^2 with all pins grounded. V_d = 0.05 V during the noise measurements. 67

Fig. 6-8. S_{Vd} at 30 Hz as a function of $V_g - V_{th}$ for ON state irradiation (a) after and (b) before ON stress of InAlN/GaN HEMTs. V_d = 0.05 V during the noise measurements. 68

LIST OF TABLES

Table 1-1. Parameters of the crystal structure and the band structure of wurtzite GaN, AlN, and InN (after [11]). 5

Table 3-1. Maximum energies of particles (after [37]). 19

Table 4-1. Guide to experiments reported. All characterizations are performed at 23.5 ±3.5 ^{o}C.......... 28

Chapter I. Introduction

1.1 Wide Bandgap Semiconductors

1.1.1 History

The proposal to develop power devices from wide bandgap (WBG) semiconductors can be traced to an analysis published in 1982 [1]. The analysis predicted a reduction in the specific on-resistance of unipolar power devices by a factor of 13.6 by replacing silicon with GaAs, the most mature semiconductor technology at that time. The development of SiC and GaN power devices has been motivated by the opportunity to create unipolar devices with high blocking voltage capability.

The growth and commercial supply of 6 H and 4 H SiC wafers by CREE in the 1990s made the development of SiC power device feasible. The first high voltage SiC power device reported in 1992, was a 400 V Schottky rectifier without edge termination [2]. The breakdown voltage was enhanced to 1000 V using the argon-implanted termination [3]. This was a milestone as the first verification of the low specific on-resistance of the drift region in SiC devices. The demonstration of SiC power MOSFETs was delayed by interface problems between the semiconductor and the gate oxide [4]. The fabrication of a 1 kV trench-gate SiC power MOSFET was reported in 1997 [5]. These devices lacked the shielding of the gate oxide that is necessary for reliable operation. The second era for SiC power devices began in 2000. Major investments in product development occurred in the United States, Europe, and Japan. The technology allows introduction of first SiC Schottky power rectifier in 2001 [6]. These devices became ideal companions to silicon IGBTs for H-bridge motor-control

application. The introduction of the SiC power MOSFET into the market in 2011 with 1200 V rated devices [6], which offered very favorable reduced switching losses when compared with silicon IGBTs in inverter circuits. The ability to increase the circuit operating frequency by using the SiC power MOSFETs reduced the size and cost of the passive elements offsetting the higher device cost. The 1700 V rated SiC power MOSFET product was introduced in 2015. SiC power MOSFET with higher voltage ratings can be expected to become available in the future.

There was initial push to establish products with lower voltage ratings of 20 – 200 V. This strategy must overcome the significant strides made for silicon devices by using the charge coupling concept to create the split-gate silicon trench MOSFET [7]. The application of the GaN technology to create very compact, lightweight, chargers for mobile devices, such as cellphones and laptops, has provided market traction for these devices. One major factor in favor of the lateral GaN devices is availability of low cost 6 in. and 8 in. GaN-on-Si wafers [6].

1.1.2 Applications

The primary applications for SiC power devices have been identified to be: (1) power supplies for data centers; (2) renewable energy sources – solar and wind power; (3) motor drives; (4) rail transportation; and (5) electric and hybrid-electric vehicle. The market for these applications is shown in Fig. 1-1 with the device ratings required for each case and the highest circuit operating frequency [6]. The manufactures have released products with voltage ratings of 900 V – 1700 V to supply low power residential solar inverters and consumer power factor correction circuits. Devices with higher voltage ratings, larger than 3300 V, serve the needs of heating ventilating and air conditioning and the wind power applications.

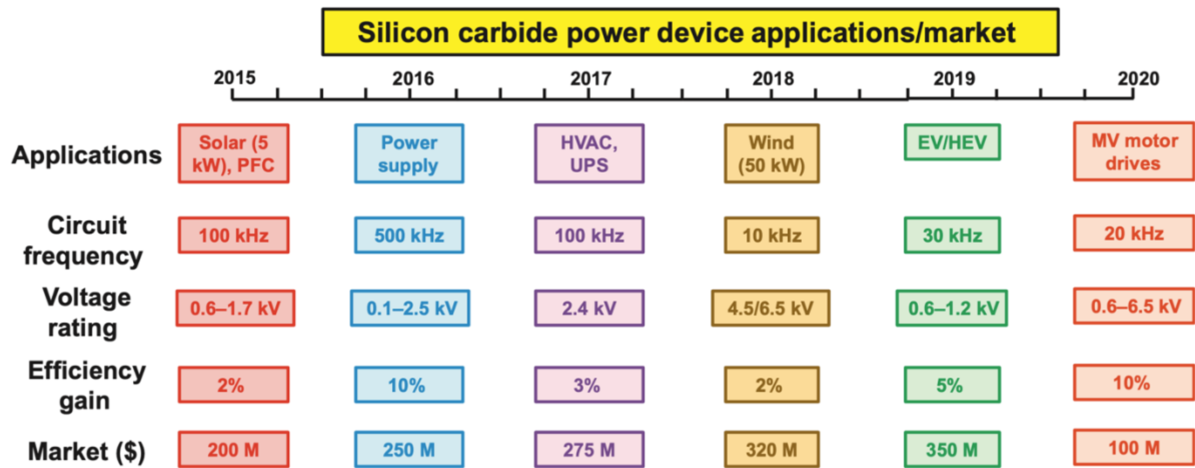

Fig. 1-1. SiC device application requirements and market size (after [6]).

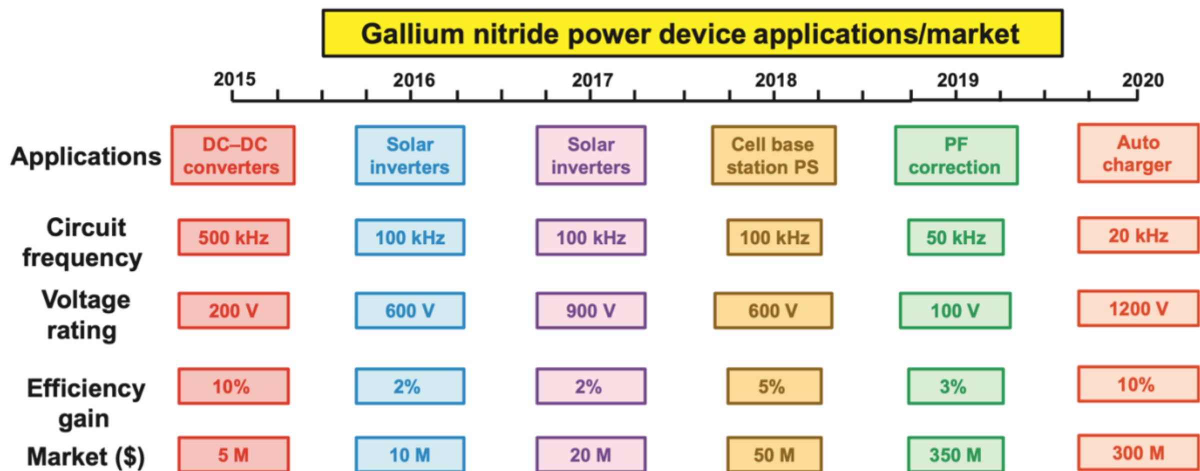

Fig. 1-2. GaN device application requirements and market size (after [6]).

With great advances made in GaN power devices, the applications are (1) DC-DC converters; (2) solar inverters for residential use; (3) cell phone base station power supplies; (4) Power factor correction in consumer applications; and (5) charging stations for electric vehicles. Fig. 1-2 shows the market for these applications with the device ratings required for

each case and the highest circuit operating frequency [6]. Devices with voltage less than 200 V have been deployed for low power DC-DC converters used for powering cell phones and laptops. Devices with 600 V ratings have been used to commercialize a compact solar-power generator for residential use.

1.2 Properties of GaN

1.2.1 Crystal structure

Group III nitride semiconductor materials contain mainly the binary compounds of AlN, GaN, and InN, and the ternary and quaternary alloys (AlGaN, InGaN, and AlInGaN) composed by them. Nitride semiconductor crystals are usually in two different structures, the hexagonal wurtzite and the cubic zinc-blende in Fig. 1-3 [8]. Both covalent bonds and ionic bonds exist between the compound semiconductor crystal atoms. All nitrides are strong ionic crystals, and the wurtzite structure is the dominant and thermodynamically stable under room temperature and atmospheric pressure, where the zinc-blende structure is metastable. Wurtzite III nitrides are employed in the majority of nitride semiconductor researches up to date, while little attention has been paid to zinc-blend III nitrides. The crystal structure and band structure parameters for wurtzite GaN, AlN, and InN are included in Table 1-1 [9] [10] [11].

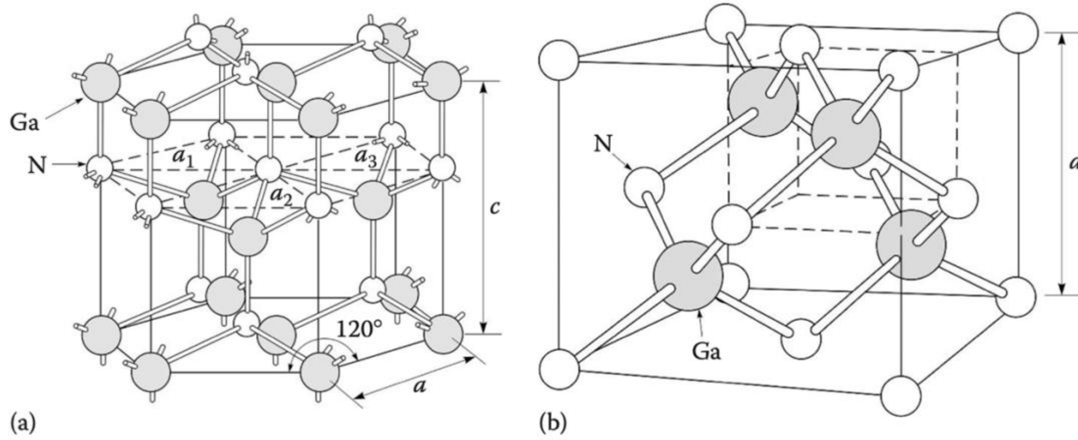

Fig. 1-3. Two crystal structures of GaN: (a) wurtzite and (b) zinc-blende (after [8]).

Table 1-1. Parameters of the crystal structure and the band structure of wurtzite GaN, AlN, and InN (after [11]).

	GaN	AlN	InN
Lattice constants a (nm)	0.3189	0.3112	0.3533
Lattice constants c (nm)	0.5185	0.4982	0.5693
Room temperature band gap E_g (300 K) (eV)	3.39	6.026	1.970 (Wu et al. 2003) 0.641 (Bougrov et al. 2001)
Temperature characteristic of band gap $E_g = E_g(0) - AT^2/(T+B)$ (eV)	$E_g(0) = 3.47$ eV $A = 7.7 \times 10^{-4}$ $B = 600$ (Siklitsky)	$E_g(0) = 6.13$ eV $A = 1.799 \times 10^{-3}$ $B = 1462$ (Wu et al. 2003)	$E_g(0) = 1.994$ eV, $A = 2.45 \times 10^{-4}$, $B = 624$ (Wu et al. 2003) or $E_g(0) = 0.69$ eV, $A = 4.1 \times 10^{-4}$, $B = 454$ (Bougrov et al. 2001)
Electron affinity (eV)	4.1	0.6	5.8
Effective densities of states of conduction band N_C (cm^{-3})	$N_C = 4.3 \times 10^{14} \times T^{3/2}$ N_C (300) $= 2.3 \times 10^{18}$	$N_C = 1.2 \times 10^{15} \times T^{3/2}$ N_C (300) $= 6.3 \times 10^{18}$	$N_C = 1.76 \times 10^{14} \times T^{3/2}$ N_C (300) $= 9 \times 10^{17}$
Effective densities of states of valence band N_V (cm^{-3})	$N_V = 8.9 \times 10^{15} \times T^{3/2}$ N_V (300) $= 4.6 \times 10^{19}$	$N_V = 9.4 \times 10^{16} \times T^{3/2}$ N_V (300) $= 4.8 \times 10^{20}$	$N_V = 10^{16} \times T^{3/2}$ N_V (300) $= 5.3 \times 10^{19}$
Electron effective mass	$0.20 m_0$	$0.40 m_0$	$0.11 m_0$
Hole effective mass	$m_{hh} = 1.4 m_0$ (heavy hole) $m_{lh} = 0.3 m_0$ (Light hole) $m_{sh} = 0.6 m_0$ (split-off hole)	k_z:$m_{hz} = 3.53 m_0$ k_x:$m_{hx} = 10.42 m_0$ (heavy hole) k_z:$m_{lz} = 3.53 m_0$ k_x:$m_{lx} = 0.24 m_0$ (light hole) k_z:$m_{soz} = 0.25 m_0$ k_x:$m_{sox} = 3.81 m_0$ (split-off hole)	$m_{hh} = 1.63 m_0$ (heavy hole) $m_{lh} = 0.27 m_0$ (light hole) $m_{sh} = 0.65 m_0$ (split-off hole)

1.2.2 Electron velocity-field relationship

The low field electron mobility of GaN can be determined by the Hall measurements, showing an increase followed by a decrease with higher temperature shown in Fig. 1-4 [12], which is caused by the weakened ionized impurity scattering and enhanced lattice vibration scattering at higher temperature. The dislocations, doping and compensation also have an impact on the low field mobility. The mobility dispersion is strongly correlated to the GaN dislocation density. The higher the dislocation density in GaN, the lower mobility it has. The electron velocity field relationship for GaN is often studied by the Monte Carlo method to establish the analytical model and can be obtained experimentally from the I-V characteristics of samples using high voltage pulse signals. Fig. 1-5 shows the theoretical electron velocity field curves of GaN with a background ionized impurity concentration of 10^{17} cm^{-3} obtained from the full band Monte Carlo simulation [13].

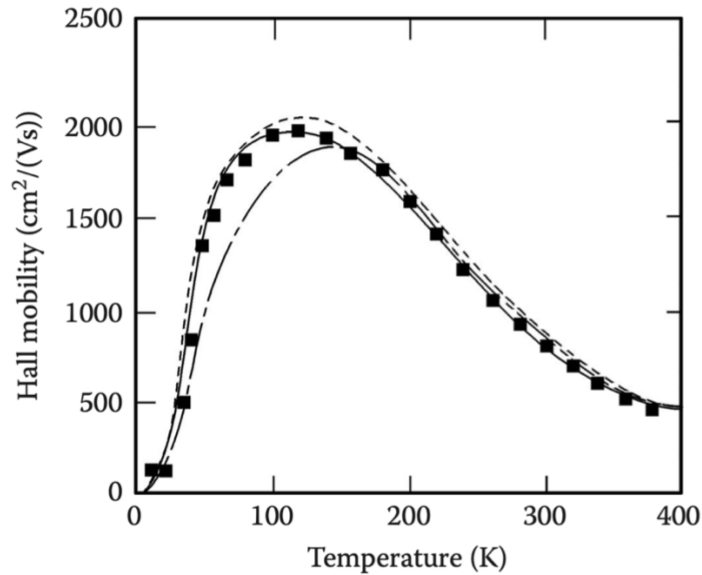

Fig. 1-4. Temperature dependence of electron Hall mobility for GaN with a background ionized impurity concentration of 10^{17} cm^{-3} (after [12]).

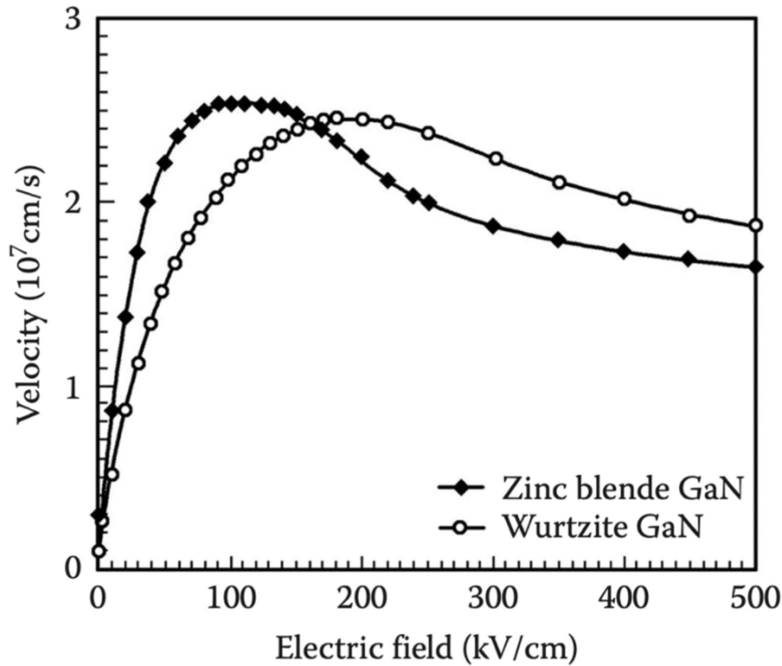

Fig. 1-5. Electron drift velocity as a function of applied electric field for GaN with a background ionized impurity concentration of 10^{17} cm^{-3} (after [13]).

1.2.3 Polarization effect

Both wurtzite and zinc-blende structure crystals are noncentrosymmetrical crystals with polar axes. Wurtzite structure nitrides have only one polar axis, namely the *c*-axis [11]. The crystal is formed by the stacking of bilayers in different sequences along the two opposite directions parallel to the c-axis shown in Fig. 1-6 [14]. The polarity is irrelevant with whether the surface of GaN is terminated by Ga or N. Different polarity differs greatly in physical and chemical properties such as reaction to acid and alkali, surface adsorption, Schottky barrier [15], and band offsets [16] at heterointerfaces, and therefore the two polarity are not same. Few direct methods of precision are available for predicting the material polarity in nitride thin film epitaxial growth, which requires experimental techniques such as the convergent beam electron diffraction, chemical etching and circular polarization spin photoelectric effect.

According to current reports [11], surface polarity varies with substrates, nucleation layers, growth conditions, and growth techniques. The lattice deformation induces a separation of the centers of positive and negative charges in the crystal to form dipole moments with applied stress, the accumulation of which gives rise to polar charges on the crystal surface, hence the piezoelectric polarization [6]. Since wurtzites have poorer crystal symmetry than zinc-blendes, their positive and negative charge centers do not coincide even without stress, thereby inducing the spontaneous polarization along the polar axis [11]. In the absence of strain, the spontaneous polarization charge for GaN is 2.1 x 10^{13} cm^{-2} [14] [17].

AlGaN is expected to have higher polarization charge. Piezoelectric polarization is induced by a mechanical perturbation such as crystal stain between AlGaN and GaN. AlGaN/GaN high electron mobility transistor (HEMT) is made use of the spontaneous polarization charge difference and piezoelectric polarization due to crystal stain, which results in high electron density in two-dimensional electron gas (2DEG) [6]. Since the sign of piezoelectric polarization depends on the crystal strain, this can either aid or oppose the spontaneous polarization. Fig. 1-7 shows the sign of different polarization and the direction of electric field for GaN grown on a substrate [18]. These properties are used for the fabrication of HEMT device structures as shown in Fig. 1-8 [6], so the 2DEG is not induced by doping but instead facilitated by spontaneous and piezoelectric electric field in the AlGaN layer.

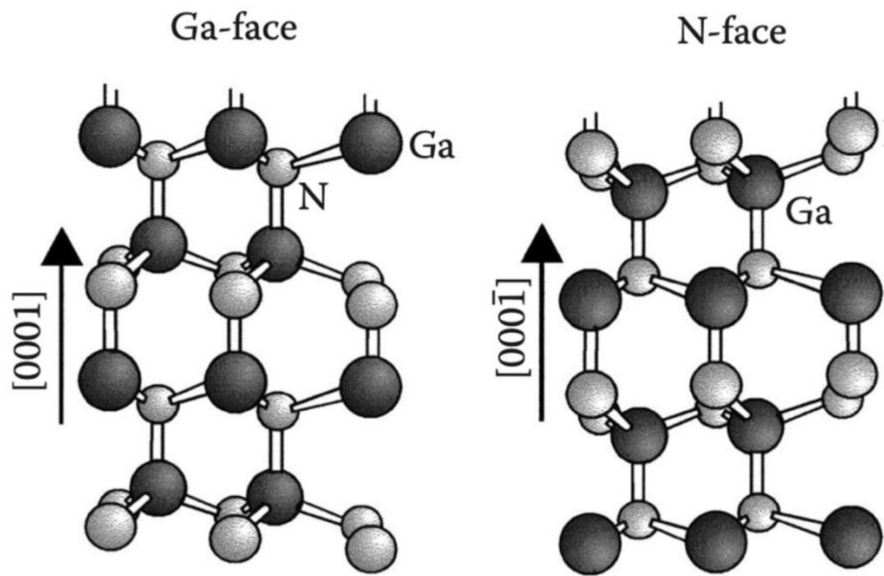

Fig. 1-6. Schematic structure of hexagonal wurtzite GaN with different polarities (after [14]).

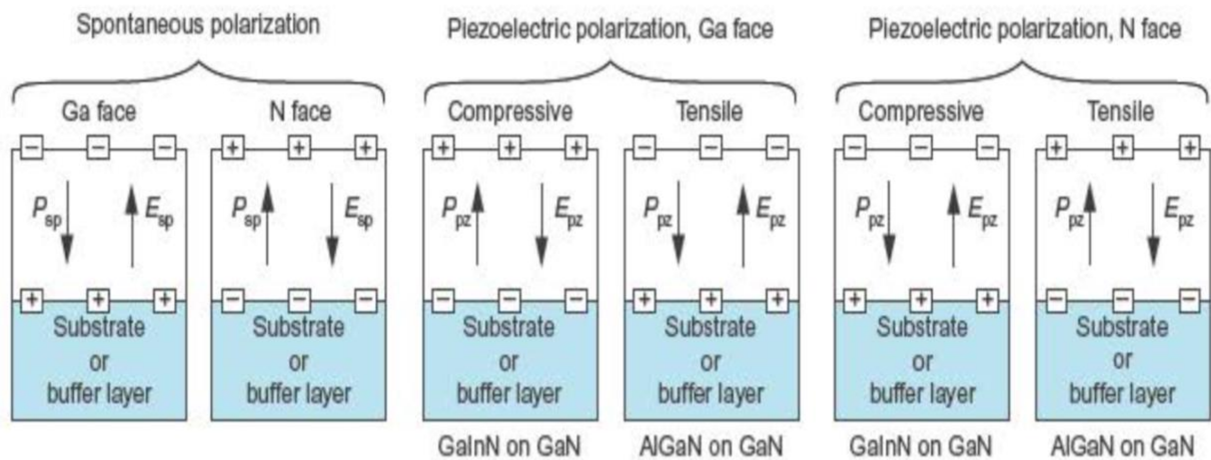

Fig. 1-7. Surface charges and direction of internal electric field and polarization filed for spontaneous and piezoelectric polarization in III-nitrides for Ga- and N-face orientation (after [18]).

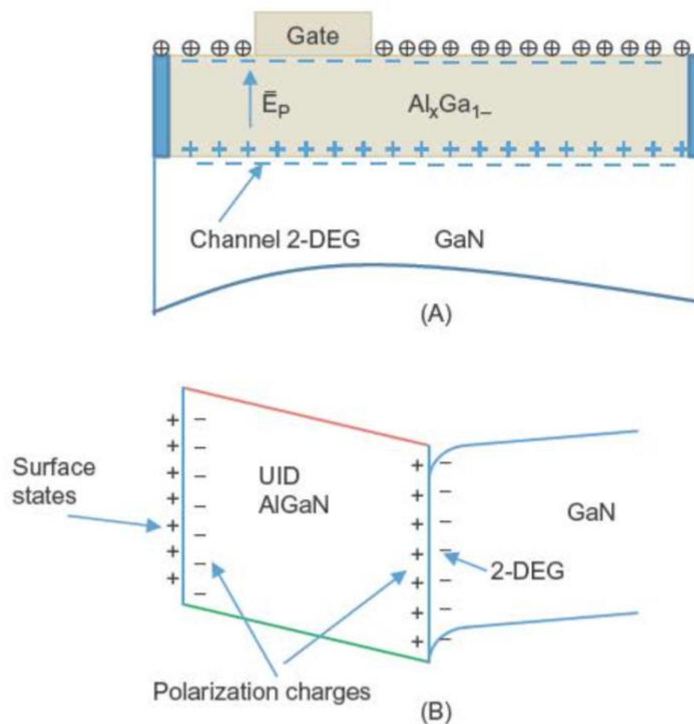

Fig. 1-8. (A) Device structure schematic, and (B) band diagram of heterostructure showing different types of charges (after [6]).

1.3 Overview of dissertation

This PhD thesis focuses on the reliability and radiation effects of GaN HEMTs. Chapter I provides a background of wide bandgap semiconductors and properties of GaN. Chapter II introduces detailed information of HEMTs and three major models of electrical degradation of the operating HEMT. Chapter III goes over the basic mechanism of total ionizing dose effects, displacement damage and low frequency noise. Chapter IV focuses on the high voltage, elevated temperature stress of AlGaN/GaN HEMTs, and Chapter V reports the effects of 10-keV X-ray irradiation and 1.8 MeV proton irradiation on GaN HEMTs. Chapter VI presents and discusses the low frequency noise results in GaN HEMTs. The last chapter concludes the thesis.

Chapter II. HEMT

2.1 History and basic structure

The working of HEMT uses the concept of modulation doping, which was first demonstrated in 1978 by Ray Dingle and his collaborators in Bell Labs [19]. From the early device research, the high-speed switching characteristics of HEMT devices became evident in 1981 when Fujitsu demonstrated a ring oscillator switching at a delay as low as 17.1 ps [20]. This first HEMT integrated circuit used both enhancement and depletion-mode logic. The energy band diagram of the HEMT was proposed by Dr. Takashi Mimura in 1987 as shown in the Fig. 2-1 [21]. With more stabilized technology and the improvements in manufacturing technologies, HEMTs became essential components of the devices with lowest noise characteristics [22]. In early 1990s, HEMTs were first demonstrated using heterojunctions based on nitride semiconductors, such as AlGaN/GaN HEMTs. HEMTs have been demonstrated in several material systems in the AlGaAs/GaAs and AlGaN/GaN systems [23] [24]. Nowadays, HEMTs are omnipresent in applications ranging from cryogenic low noise amplifiers, radio telescope to detect microwave signals from a dark nebula, broadcasting satellite receivers, cell phone handsets and automotive radars. Fig. 2-2 shows the structural cross section of a HEMT [25]. The heart of HEMT is the formation of 2DEG in a quantum well.

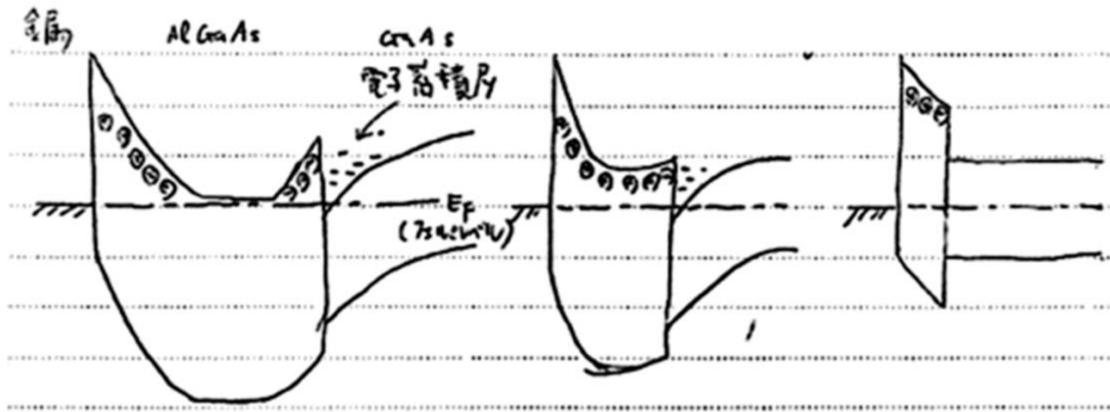

Fig. 2-1. Energy band diagram as proposed by Dr. Takashi Mimura (after [21]).

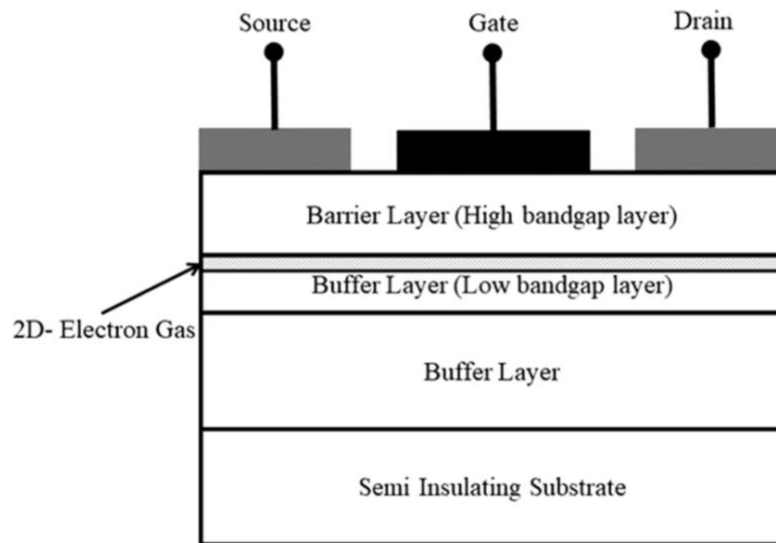

Fig. 2-2. Basic cross section of a HEMT device (after [25]).

2.2 Formation mechanisms of 2DEGs

In the conventional AlGaAs/GaAs material system, 2DEG electrons result mainly from the donor ionization in AlGaAs and GaAs. However, for AlGaN/GaN heterostructures, 2DEGs of sheet densities of the order of 10^{13} cm^{-2} are available even without intentional

doping [11]. In 1999, Smorchkova et al. observed that a critical thickness of AlGaN layer for the formation of the 2DEG in AlGaN/GaN heterostructure samples of different AlGaN layer thickness, where the 2DEG density increases rapidly with further increase in AlGaN thickness and then saturates [26]. Accordingly, they proposed a model in which the 2DEG originates mainly from the ionization of donor-like AlGaN surface traps. In the Fig. 2-3, as the AlGaN layer thickness increases before the formation of the 2DEG, the polarization field raises the surface potential (the height of the conduction band edge E_C with respect to the Fermi level E_F at AlGaN surface), and a surface donor-like trap with the energy level E_{DS} below the conduction band rises accordingly [26]. When E_{DS} aligns with the Fermi level, the 2DEG emerges as electrons are released by surface donor trap ionization with a reduced AlGaN built-in field. As the AlGaN layer grows thicker, the 2DEG density tends to saturate approaching the density of the positive polar charge at the AlGaN/GaN interface with E_{DS} kept aligning with the Fermi level. This model interprets the variation of the 2DEG density with AlGaN thickness, and proposes the contribution of surface charges to the 2DEG formation where unintentional doping fails to provide enough electrons for the 2DEGs [26].

In 2001, Koley and Spencer studied the surface potential of GaN epilayers with different doping and $Al_{0.35}Ga_{0.65}N$/GaN heterostructures having different AlGaN layer thickness by scanning Kelvin probe microscopy [27]. They found that the surface potential of GaN is greater than the energy difference of E_C to E_F inside GaN and decreases with increasing n-type doping of GaN, but the surface potential of $Al_{0.35}Ga_{0.65}N$/GaN decreases with the increase in AlGaN layer thickness, which is completely opposite to the surface potential change illustrated by the model of surface donor state ionization as shown in Fig. 2-3 [27]. So, it is proposed the presence of negatively charged acceptor-like traps at the GaN surface

and in the AlGaN barrier layer. Based on this model, the acceptor-like traps are negatively charged when the AlGaN layer of AlGaN/GaN heterojunction is thin, so the surface potential is high and no 2DEG is present. As the AlGaN layer thickness increases, the acceptor-like traps release electrons and the surface potential is lowered, and so the 2DEG emerges and grows in density resulting from both the accumulation of electron released from the acceptor-like traps and the weakening of the surface depletion effect [27]. Therefore, the variation of 2DEG density and surface potential of AlGaN/GaN heterostructure with AlGaN content and thickness can be attributed to the co-work of the surface state and the polarization effect [11].

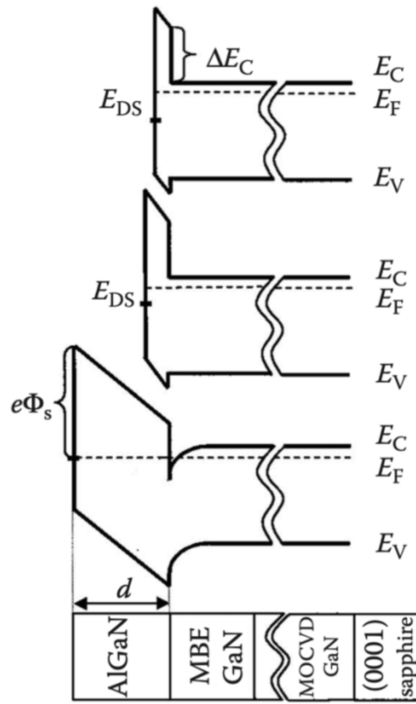

Fig. 2-3. Energy band of AlGaN/GaN heterojunction as a function of AlGaN layer thickness. The donor-like surface trap is at the level E_{DS} (after [26]).

2.3 Advantages of InAlN/GaN HEMT

The AlGaN/GaN HEMT has strong spontaneous and piezoelectric polarization. The inverse piezoelectric effect may arise from too strong an electric field in the device at high voltage, resulting in material degradation and in worse cases microcracks [11]. Therefore, it is desired to find an HEMT structure that can eliminate the piezoelectric polarization without seriously affecting the 2DEG density so as to avoid the negative influence of strong inverse piezoelectric effect on the device reliability. The nearly lattice matched InAlN/GaN heterostructure has become a highly favored structure for GaN HEMTs lately.

Fig. 2-4 shows the InAlN bandgap as a function of the lattice constant and the structure of the InAlN/GaN heterojunction [11]. InAlN with an indium content of 17% can be lattice matched to GaN, and the generated $In_{0.17}Al_{0.83}$/GaN heterostructure has the spontaneous polarization and very little piezoelectric polarization, thus significantly diminishing the inverse piezoelectric effect in strong electric field [11] [25]. Although the strictly lattice-matched InAlN/GaN eliminates the lattice mismatch strain in the barrier and has only spontaneous polarization and no piezoelectric polarization as compared to AlGaN/GaN, the former has a strong total polarization effect than the latter because $In_{0.17}Al_{0.83}$ has very strong spontaneous polarization. With good barrier crystalline quality, AlGaN/GaN generally needs a barrier thickness of around 25 nm to obtain a 2DEG density of approximately $1.0 - 1.8 \times 10^{13}$ cm^{-2}, while the lattice-matched InAlN/GaN with only a 5–15-nm-thick unintentionally doped InAlN barrier can achieve high conductivity characteristics with a 2DEG density higher than 2.5×10^{13} cm^{-2} and a sheet resistance lower than 220 Ω/sq [28] [29] [30]. As for the HEMT characteristics, the InAlN/GaN HEMT with only 13-nm-thick InAlN can yield a maximum output current up to 2.0 A/mm while the AlGaN/GaN HEMTs on sapphire, SiC

and Si substrates generally achieve only about 0.8–1.6 A/mm [31]. InAlN/GaN HEMTs also exhibit better current driving capability and apparent superiority in device scaling, very desirable characteristics for high-frequency power devices [31] [32]. InAlN/GaN HEMTs with InGaN back barrier were reported to achieve f_T of 290–300 GHz at a gate length of 30 nm [32], and even up to 370 GHz at a gate length of 20 nm [33].

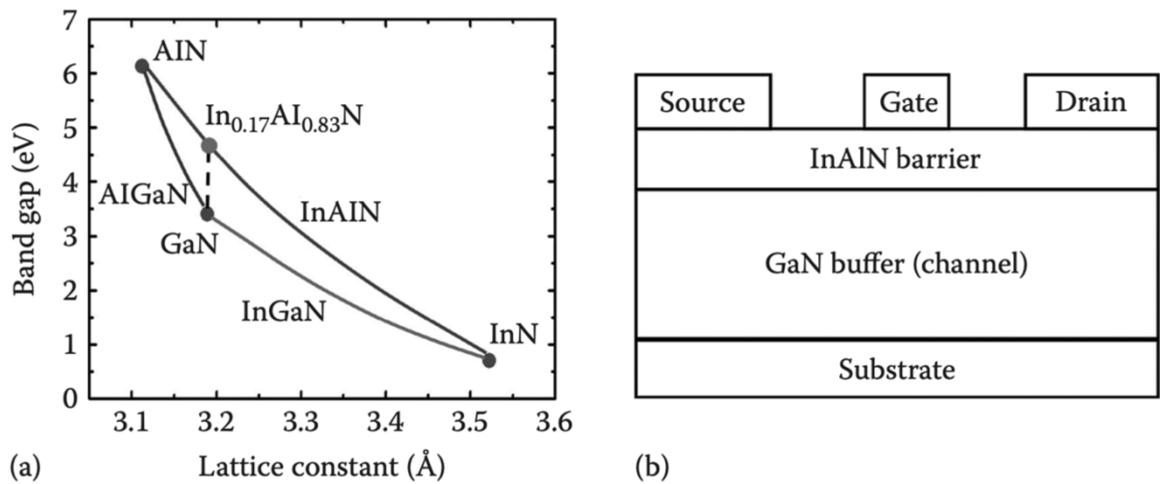

Fig. 2-4. (a) Bandgap as a function of the lattice constant, and (b) lattice-matched InAlN/GaN heterostructure (after [11]).

2.4 Models of electrical degradation

The major means to investigate the degradation mechanisms of the operating HEMT is the analysis of degradation characteristics, with electrical stress applied on the device. Studies show that the GaN HEMT failure is due mainly to the strong electric field in the large-signal operation with three major models of the failure mechanism: the hot electron injection, the gate electron injection, and the inverse piezoelectric effect [11]. In the hot electron injection model, the channel electrons in HEMT devices are accelerated by the strong electric field

under on-state, off-state, or radio frequency (RF) electrical stress, and some become high-energy hot electrons. These hot electrons transfer in real space to spill over the quantum wells in the channel and are captured by surface traps or buffer layer traps, thus resulting in a reduced channel electron density with decreased leakage current and transconductance. Such high-energy hot electrons also collide with crystal lattice to produce new defects that aggravate the degradation [11].

Trew et al. suggested that with the effect of the electric field peak at the gate edge near the drain, the gate electrons are injected onto the barrier layer surface and then the gate-drain leakage current is generated via the hopping conduction between surface traps [34]. The gate current charges the surface traps, leading to a raised barrier layer potential and reduced density of the channel electrons, thus resulting in a drop of drain current and transconductance. Gate electron injection may both induce irreversible degradation of the Schottky gate on long-term basis and play an assisting role in the irreversible degradation of GaN HEMTs caused by hot electron injection or inverse piezoelectric effect.

Fig. 2-5 shows the schematic diagram of the inverse piezoelectric effect model [35]. At the gate edge on the drain side exists a strong electric field, under the effect of which the crystal lattices are stretched, owing to the inverse piezoelectric effect, until the lattice structures are broken to generate lattice defects. The transmission electron microscope image in Fig. 2-6 shows that the device exposed to the strong electric field for a long time develops a tiny crack under the drain-side gate edge, because the crystal lattices are strained, until they are broken under the inverse piezoelectric effect [36]. All three models discussed above can be employed to explain device degeneration, but none of them can individually account for all the degeneration phenomena.

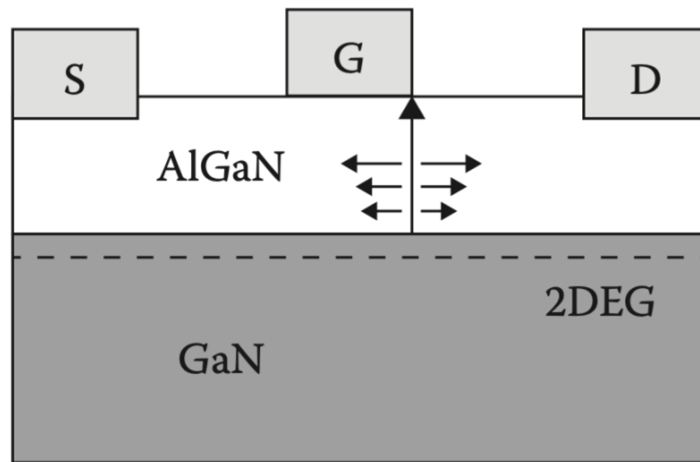

Fig. 2-5. Schematic of inverse piezoelectric effect (after [35]).

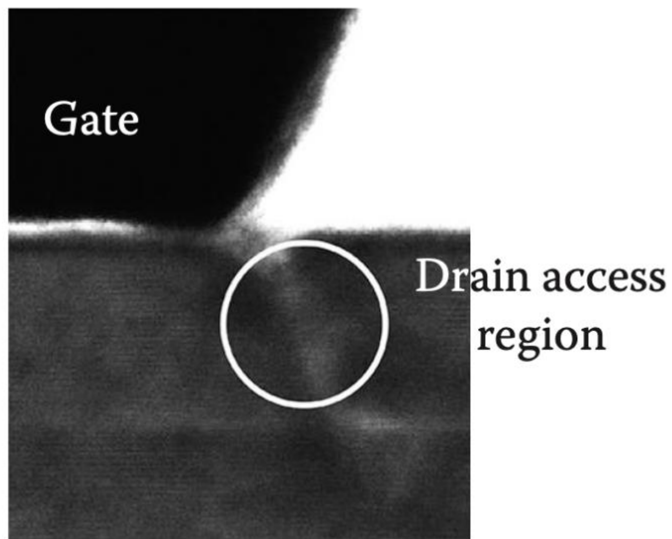

Fig. 2-6. The transmission electron microscope image of the drain-side edge of the gate after experiencing strong electric field (after [36]).

Chapter III. Radiation effects and low frequency noise

3.1 Radiation effects

Space radiation environment can be classified into two groups: the particles trapped by planetary magnetospheres in "belts", including protons, electrons, and heavier ions and transient particles including protons and heavy ions of all the elements of the periodic table. Table 3-1 shows the maximum energy of space radiation particles [37].

Table 3-1. Maximum energies of particles (after [37]).

Particle Type	Maximum Energy
Trapped Electrons	10s of MeV
Trapped Protons & Heavy Ions	100s of MeV
Solar Protons	GeV
Solar Heavy Ions	GeV
Galactic Cosmic Rays	TeV

3.1.1 Total ionizing dose

When MOS devices are exposed to high energy ionizing radiation, electron-hole pairs can be created. The oxide is the most sensitive part for ionizing irradiation. Fig. 3-1 shows a schematic energy diagram of a MOS device under positive bias applied to the gate and

physical mechanisms that contribute to the radiation response [38]. The effect related to the ionizing radiation is the generation of electron-hole pairs in the oxide [39] [40]. Because the electrons are more mobile than the holes in SiO_2, most of the electrons are rapidly swept out of the oxide, and holes are trapped in micro-structural defects and pre-existing traps. Part of the electrons will also recombine with holes. The fraction of electron-hole pairs that escape recombination is called the electron-hole yield or charge yield, which depends on the strength of the electric field in the oxide and the energy of the incident particle. Holes may transport to the Si/ SiO_2 interface by hopping via localized traps in the oxide. At the interface, some holes are neutralized by electrons tunneling from silicon or thermal emission from the trap sites, and others get trapped at deep traps to form oxide trap charges, which can cause a shift in the threshold voltage and increase the leakage current of a circuit. Meanwhile, protons can be released in the oxide as holes transport to the Si/ SiO_2 interface. Those protons can drift to the interface under positive gate bias where they can react with Si-H to form H_2, leaving silicon dangling bonds at the interface. These interface traps can cause shift of threshold voltage, decrease of carrier mobility, or even failure of integrated circuits.

GaN HEMTs are more tolerant to ionizing radiation [41] [42] [43] compare to Si-based MOS devices because of the higher surface trap density in GaN and usually absence of oxide layer. However, significant threshold voltage shifts have been observed for GaN HEMTs during 10-keV X-ray irradiation recently [44] [45]. Fig. 3.2 shows a threshold voltage shift of -0.1 V when exposed to 1 Mrad(SiO_2) with 10-keV X-rays for GaN HEMTs [44].

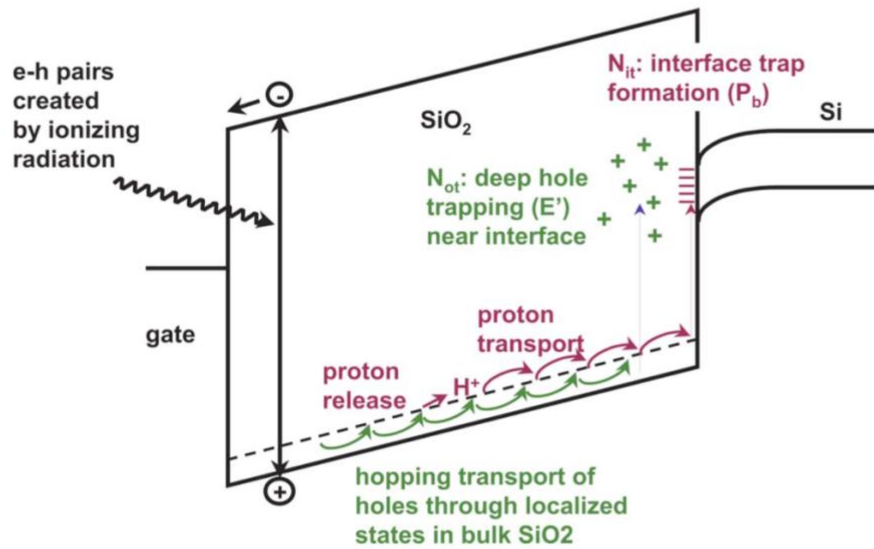

Fig. 3-1. Schematic energy band diagram for a MOS device under positive bias, indicating major physical processes for radiation induced charge generation (after [38]).

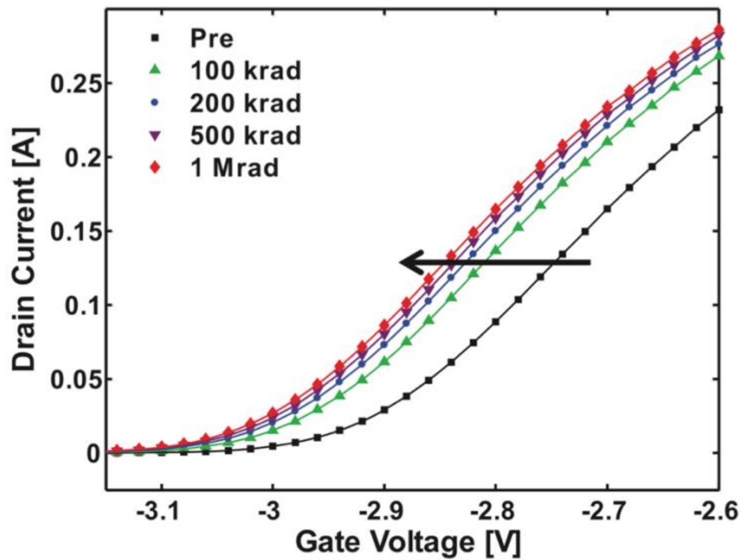

Fig. 3-2. Drain current vs. gate voltage for the CGH40006P as a function of total ionizing dose using 10 keV X-rays up to a dose of 1 Mrad(SiO_2). Note a negative shift in threshold voltage. This plot shows the worst-case threshold voltage shift of the two Cree devices tested for TID. The arrow indicates the direction in increasing radiation (after [44]).

3.1.2 Displacement damage

Displacement damage is the result of a non-ionizing process where an atom is displaced. The Vacancies and interstitials are the primary lattice defects. The combination of a vacancy and an adjacent interstitial is known as a close pair or a Frenkel pair. Fig. 3-3 shows the spatial distribution of the initial vacancy-interstitial pairs for the example of proton irradiated Si [46] [47]. Displaced atoms may cause new energy levels into the bandgap, which would change the property of devices [48] [49] [50].

Compared with total ionizing dose effects, a bigger concern for GaN HEMTs is displacement damage. After irradiation, GaN HEMTs typically exhibit threshold voltage shift, increased junction leakage, transconductance degradation and noise enhancement [45] [51]. 1.8 MeV protons are commonly used to study displacement damage in GaN HEMTs, due to much larger non-ionizing energy loss than higher energy protons [43] [52].

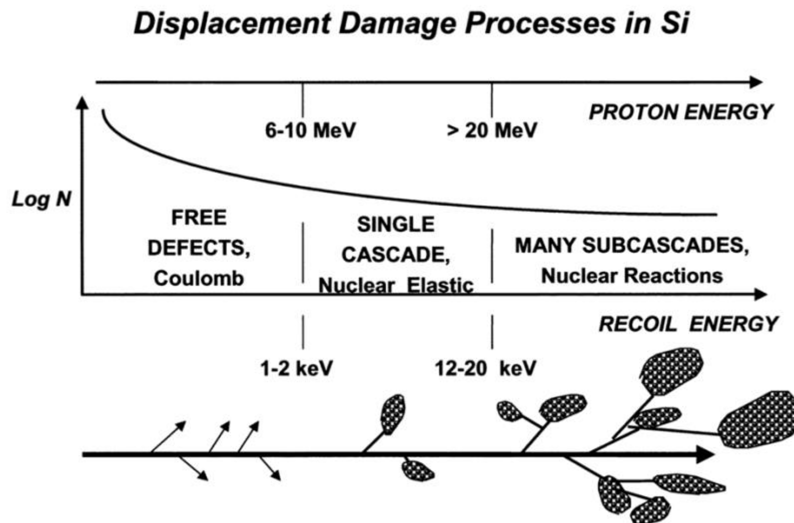

Fig. 3-3. Spatial distribution of the initial defect configuration to the primary knock-on atom energy in Si material (after [46]).

3.2 Low frequency noise

The current will fluctuate, and the spectral density varies over a range of frequencies when a constant voltage is applied to a semiconductor device. Fig. 3-4 shows a typical noise spectrum in a MOS transistor, in which the drain voltage power spectral density S_V is plotted as a function of frequency, showing the dominance of $1/f$ noise at low frequency and thermal noise at higher frequencies [53]. Fig. 3-5 shows an example spectrum of low frequency noise in AlGaN/GaN HEMTs.

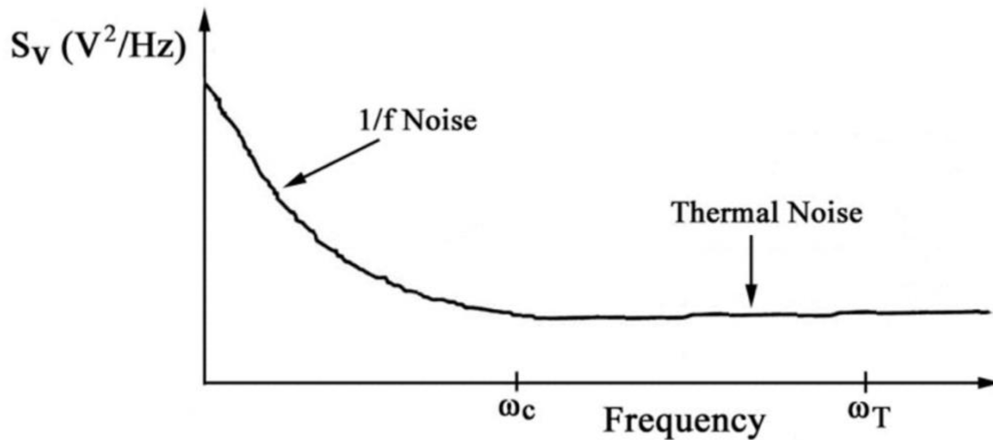

Fig. 3-4. Schematic variation of S_V with frequency (after [53]).

A variety of mechanisms have been considered to be responsible for noise. Here, we consider the effects by the trapping and de-trapping of electrons in defects near the GaN HEMTs channel [54] [55] [56]. The number fluctuation theory states that noise is generated by fluctuations in the number of carriers due to charge trapping in surface traps, where free carriers are randomly trapped by trap centers with different lifetimes. Dutta and Horn [57] have shown that noise magnitude of metal films typically has a strong temperature

dependence. They also demonstrated that the temperature dependence of the low frequency noise is due to a thermally activated random process with a distribution of activation energies, which varies with temperature.

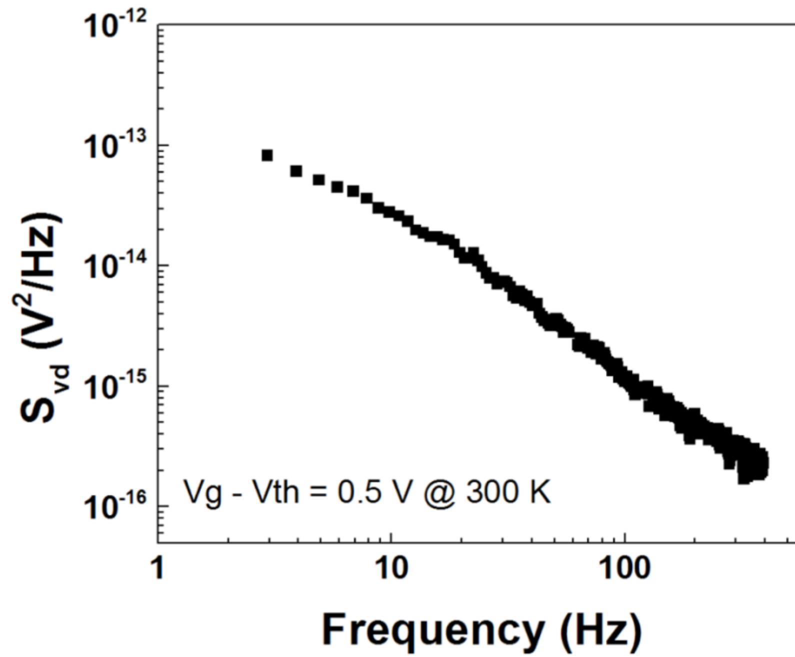

Fig. 3-5. Excess voltage noise power spectral density S_{vd} (corrected for background noise) as a function of frequency for AlGaN/GaN HEMTs at 300 K. $V_{gs} – V_{th}$ = 0.5 V, and V_{ds} = 0.05 V.

Chapter IV. High voltage stress of GaN HEMTs

AlGaN/GaN-based HEMTs are promising devices for high-power, high-voltage and high-temperature applications [58] [59] [60] [61]. Very high electric fields can be reached in these devices; the resulting hot-carrier effects can limit the long-term reliability of GaN-based HEMTs [62] [63] [64]. Several types of defects can cause hot-carrier induced degradation due to donor-like and acceptor-like defects [65] [66] [67] [68]. Elevated temperature during stress can accelerate the degradation of AlGaN/GaN HEMTs [69] [70]. Depending on the device geometry and efficiency of heat dissipation by the packaging, the core device often has a much higher temperature than ambient due to self-heating [71] [72] [73] [74] [75].

In this chapter, effects of hot-carrier stress at temperatures up to 125 ^{o}C are evaluated for industrial-quality GaN HEMTs biased in the ON, semi-ON, and OFF states. Both donor-like and acceptor-like defects can play significant roles in the device degradation, with densities depending on stress time, temperature, and bias condition. The worst-case transconductance degradation is observed under ON bias condition at elevated temperatures consistent with the results of for university-fabricated devices [69], in contrast with earlier-generation devices that often showed worst-case response under semi-ON bias conditions [76] [77] [78] [79] [80].

4.1 Experimental details

Commercial AlGaN/GaN HEMTs are fabricated by Wolfspeed, Inc. The rated device operating voltage is 28 V, the drain-source breakdown voltage is 120 V, and the thermal resistance is 8 ^{o}C /W [81]. Fig. 4-1(a) shows a Wolfspeed CGH40010F GaN-based HEMT,

Adapted with permission from P. F. Wang *et al.*, *IEEE Trans. Dev. Mater. Reliab.*, vol. 20, no. 2, pp. 420-428, Jun. 2020.

and Fig. 4-1(b) shows the test board. DC measurements were performed using an Agilent B1505A parametric analyzer (PA) as shown in Fig. 4-2 for shorter-term stresses and GW Instek GPD-3303S DC power supply for longer-term stresses [81]. Due to PA and DC supply power limitations, the applied drain bias was limited to = 40 V during semi-ON state stress and = 20 V for ON state stress.

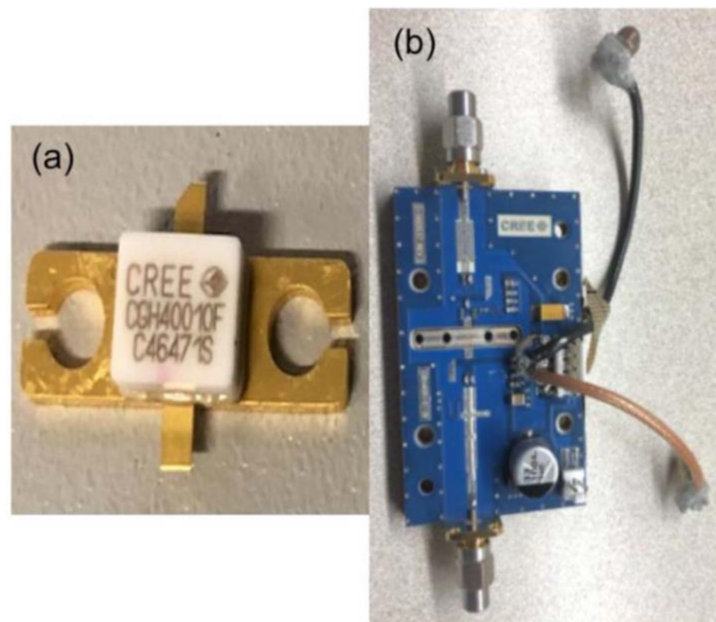

Fig. 4-1. (a) Wolfspeed CGH40010F GaN HEMT; (b) test board.

Device groups A and B were stressed at drain voltages and times under ON (Group A: gate voltage $V_{gs} = -1.5$ V; -0.5 V for Group B), semi-ON ($V_{gs} = -2.5$ V), and OFF ($V_{gs} = -4$ V) bias. Group A was stressed and tested at room temperature with no temperature control to provide a baseline response. The package temperature often increased due to self-heating during high-current stress. Group B was stressed in a Test Equity Model 140 Temperature Chamber as shown in Fig. 4-3 under controlled conditions. The ambient temperature was

chosen to add to self-heating (where applicable) to raise the package temperature as high as 125 ºC, as determined by an OMEGA HH501BJK Thermometer attached to the back of the test board. Device heated significantly by current and/or ambient were cooled for ~ 30 minutes before measuring $I_d - V_g$ characteristics. For convenience, a summary of experiments is provided in Table 4-1. At least two devices of each type were evaluated for each set of stressing and measurement conditions.

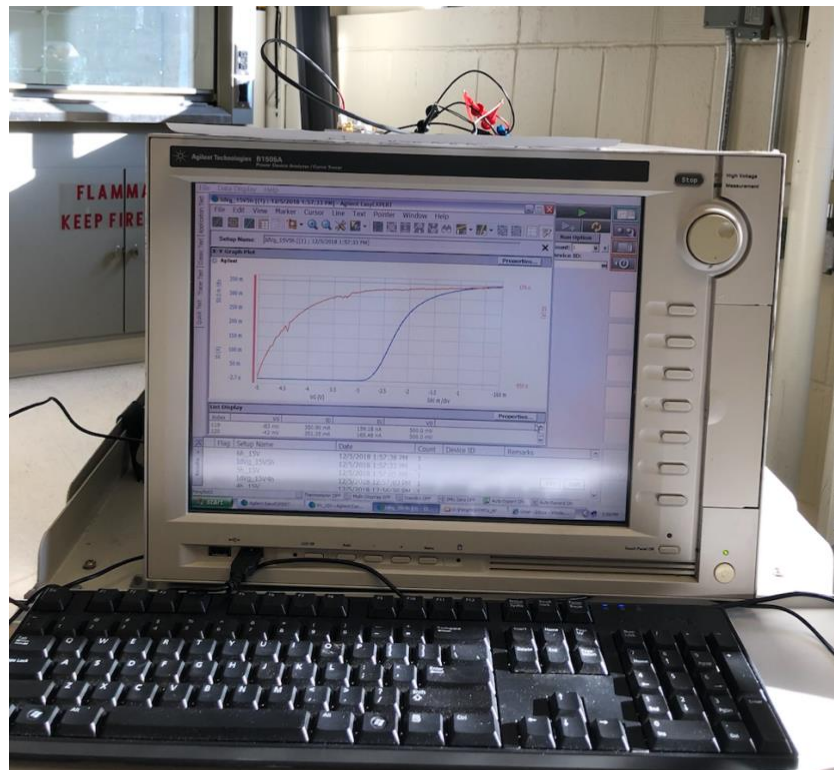

Fig. 4-2. Agilent B1505A power device analyzer.

Fig. 4-3. Test Equity model 140 temperature chamber.

Table 4-1. Guide to experiments reported. All characterizations are performed at 23.5 ±3.5 ^{o}C.

Gate Bias (Fig. #)	**Temperature Control (Fig. #)**	**Maximum Drain Voltage (Fig. #)**	**Maximum Stress Temperature (Fig. #)**
OFF (-4 V) (3, 7)	No (3) Yes (7)	100 V (3) 80 V (7)	Room T (3) 125 ^{o}C (7)
ON (-1.5 V) (4) ON (-0.5 V) (5, 8, 9)	No (4) Yes (5, 8, 9)	20 V (4) 30 V (5, 8, 9)	56 ^{o}C (4) 20 ^{o}C (5) 79 ^{o}C (8) 105 ^{o}C (9)
Semi-ON -2.5 V (6,10)	No (6) Yes (10)	40 V (6, 10)	46 ^{o}C (6) 125 ^{o}C (10)

Fig. 4-4 shows $I_d - V_d$ characteristics for a typical device. The peak transconductance G_M is calculated at the maximum first-derivative point of the $I_d - V_g$ curve with a constant value of V_d (500 mV in Fig. 4-5 and 50 mV for the remainder of the results shown); an effective value of V_{th} is the gate voltage axis intercept of the linear extrapolation of the $I_d - V_g$ curve at that point [82] [83]. At least two devices of each type were measured. Representative results are shown below.

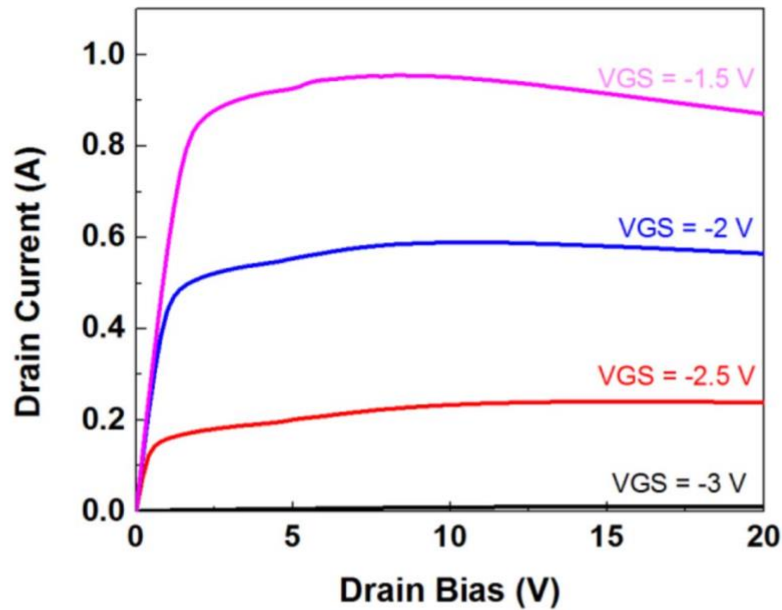

Fig. 4-4. $I_d - V_d$ curves for a representative Wolfspeed GaN HEMT.

4.2 Experimental results and analysis

4.2.1 Stepped drain-bias stress

Fig. 4-5 shows (a) drain current-gate voltage ($I_d - V_d$) curves, (b) threshold voltage V_{th} shifts, and (c) normalized peak transconductance G_M as a function of time for Group A devices stressed under OFF-state bias conditions in room ambient without temperature

control. The results of Fig. 4-5(a) show increasingly larger degradation in drive current at progressively higher drain-voltage stresses. Fig. 4-5(b) shows positive V_{th} shifts of up to ~ 220 mV at drain biases up to ~ 52 V, consistent with activation of acceptor-like defects and/or passivation of donor-like defects via electron capture at positively charged centers that were activated during processing [65]. Increasingly negative shifts are observed at higher drain biases, approaching −25 mV at V_d = 100 V.

Results at voltages above V_d = 52 V in Fig. 4-5(c) are consistent with activation of donor-like defects and/or passivation of acceptor-like defects via electron capture at positively charged centers that were activated during processing [65]. Fig. 4-5(c) shows that less than ~ 10% degradation in peak transconductance occurs during the full stressing sequence, suggesting that the charged defects responsible for the Vth shifts observed in Fig. 4-5(b) are not located closely enough to the two-dimensional electron gas to scatter carriers strongly [65] [69].

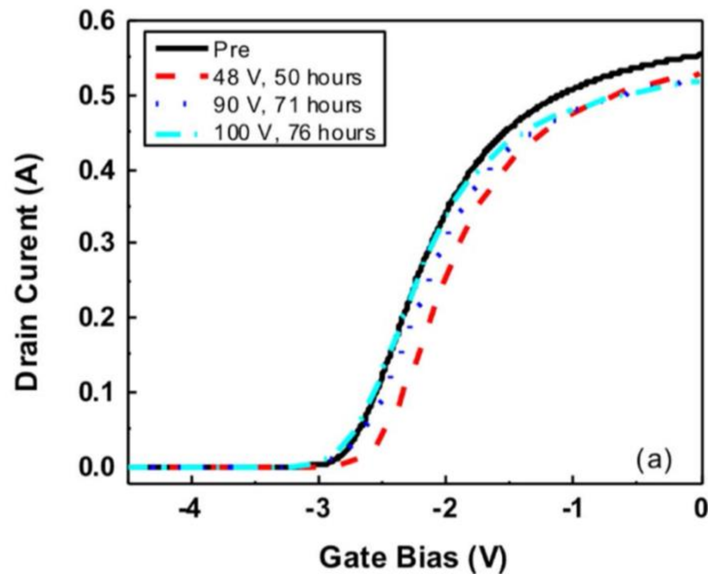

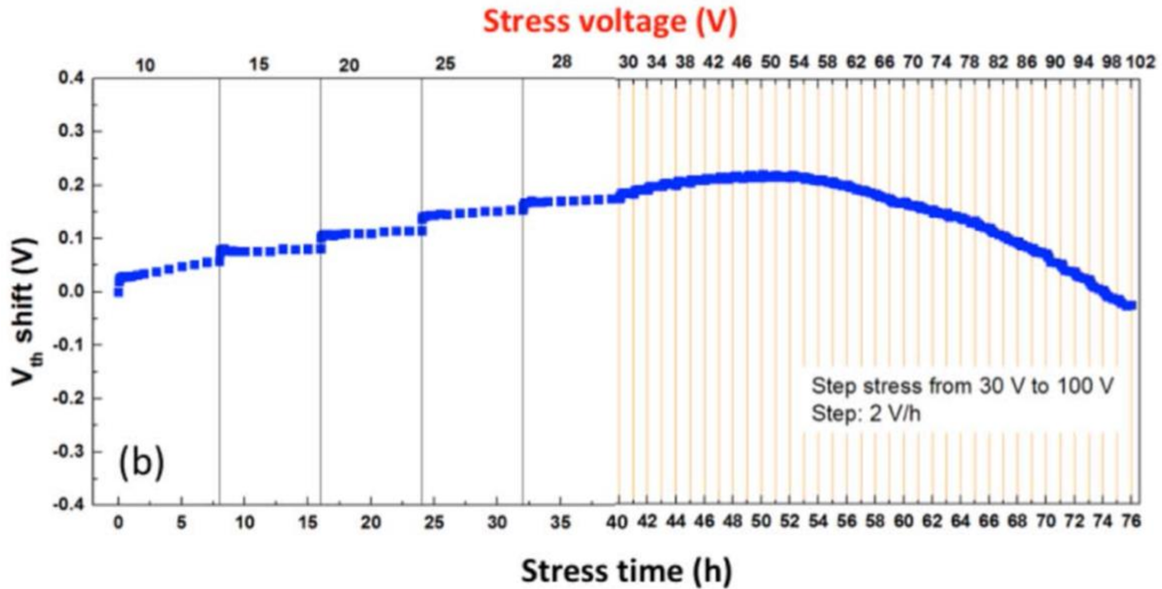

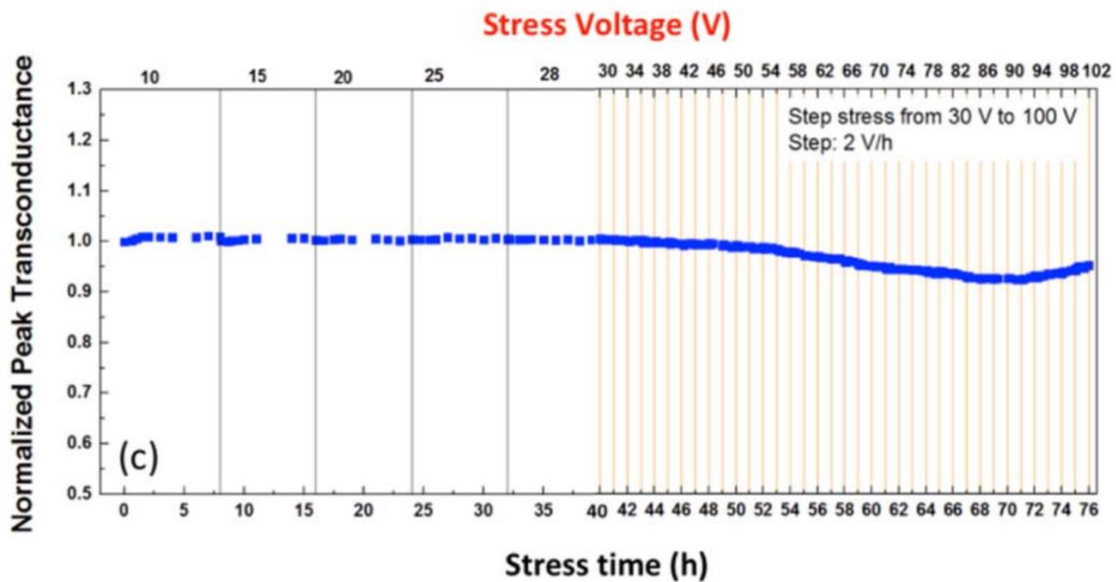

Fig. 4-5. (a) $I_d - V_d$ curves for AlGaN/GaN HEMTs at V_d = 500mV before and after the OFF-state bias stressing sequence for which (b) threshold-voltage shift and (c) peak transconductance G_M normalized to the value for an unstressed device for a series of drain biases up to 100 V and gate bias of −4 V (OFF state). For drain biases of 30 V to 100 V, the device was stressed for one h for an additional step increment of 2V additional bias on the drain. No temperature change occurs during these OFF-state bias stresses.

Fig. 4-6 shows results for stepped drain voltage stresses for AlGaN/GaN HEMTs under ON-state bias conditions at room temperature. Devices were stressed at a constant gate bias of −1.5 V, with drain biases increasing from 10 V to 20 V. The package temperature was 56 °C when devices were stressed at a drain bias of 20 V. Values of V_{th} shift negatively by ~ 30 mV and the normalized peak transconductance increases slightly after this sequence of ON-state bias stresses. This decrease in V_{th} and increase in peak transconductance suggests that passivation of acceptor-like defects may have occurred during this stressing sequence.

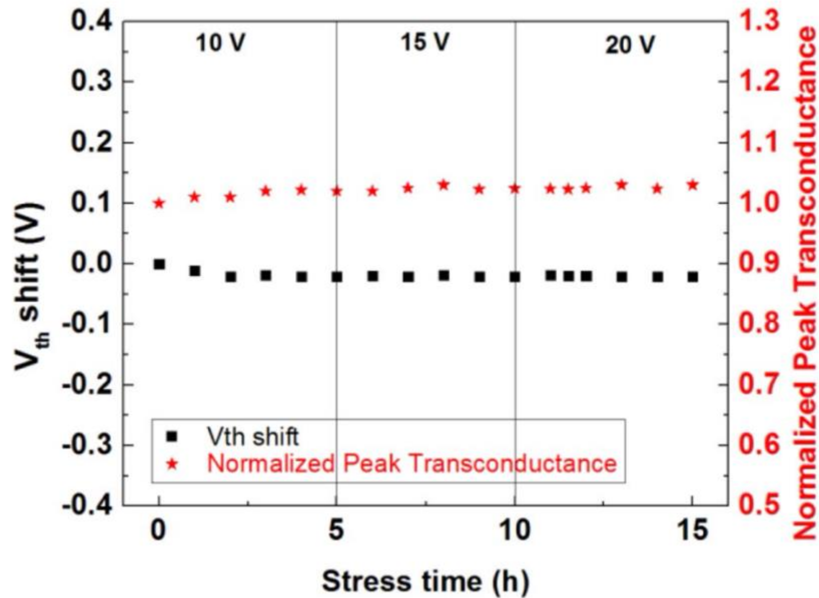

Fig. 4-6. Threshold-voltage shift (left y-axis) and peak transconductance normalized to that of an unstressed device (right y-axis) for Group A devices stressed sequentially at 10 V, 15 V, and 20 V drain bias and −1.5 V gate bias (ON state) in room ambient without temperature control. The package temperature is 56 °C when devices are stressed at the maximum drain bias of 20 V (I_d ~ 0.83 A). DC measurements are performed at room temperature after devices are cooled for ~ 30 min.

To determine the relative importance of the high current and resulting heating on the inferred defect passivation in Fig. 4-6, V_{th} shifts and peak transconductance are shown for similar devices stressed under ON-state bias conditions (V_{gs} = −0.5 V; V_{ds} = 30 V) with a thermoelectric (TE) cooling system at a package temperature of 20 °C in Fig. 4-7. There is no significant V_{th} shift or change in peak transconductance in Fig. 4-7, even though the stressing current is higher in Fig.4-7 (V_{ds} =30V) than in Fig.4-6 (V_{ds} =20V). This strongly suggests that the passivation of acceptor-like defects inferred in Fig. 4-6 is thermal in origin, and due most likely to the significant heating that occurs in Fig. 4-6 but not Fig. 4-7.

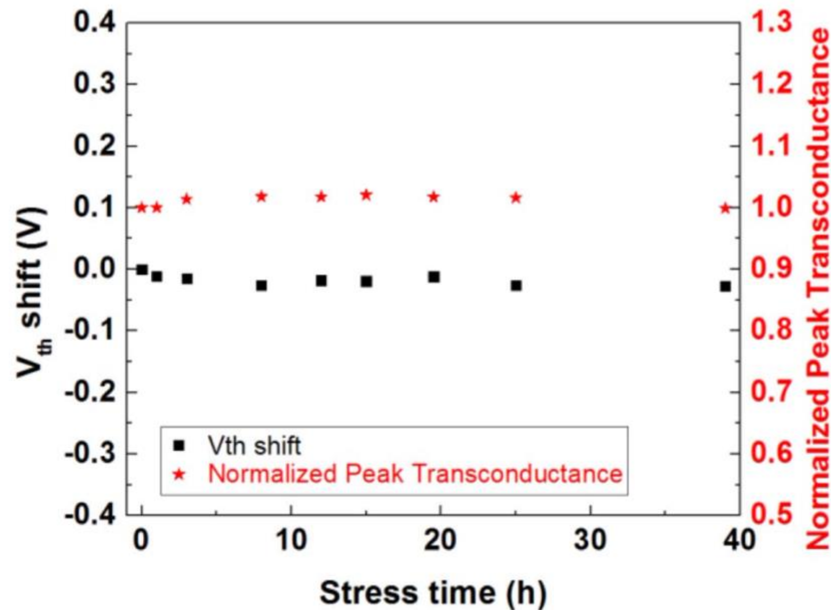

Fig. 4-7. Threshold-voltage shift (left y-axis) and peak transconductance normalized to that of an unstressed device (right y-axis) for Group B devices stressed at 30 V drain bias (I_d ~ 1.25 A) and −0.5 V gate bias (ON state) at a package temperature of 20 °C. DC measurements are performed at 20 °C.

Fig. 4-8 shows results for stepped drain voltage stresses for AlGaN/GaN HEMTs under semi-ON state bias conditions at room temperature. Devices were stressed at a constant gate bias of −2.5 V, with drain biases increasing from 10 V to 40 V. The package temperature was 46 °C when devices were stressed at the maximum drain bias of 40 V in this testing sequence. No significant Vth shifts or peak transconductance degradation are observed after any of these semi-ON state bias stresses.

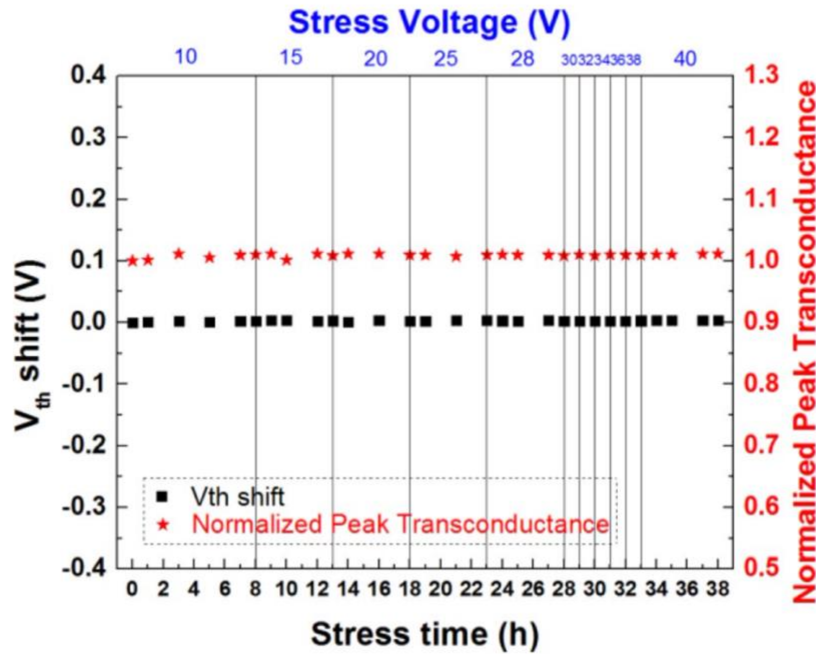

Fig. 4-8. Threshold-voltage shift (left y-axis) and peak transconductance normalized to that of an unstressed device (right y-axis) for Group A devices stressed sequentially at drain biases up to 40 V and −2.5 V gate bias (semi-ON state) in room ambient without temperature control. The package temperature is 46 °C when devices are stressed at the maximum drain bias of 40 V (I_d ~ 0.16 A). DC measurements are performed at room temperature after devices are cooled for ~ 30 min.

4.2.2 Elevated-temperature stress

To evaluate the effects of elevated temperature on defect activation and/or passivation, Fig. 4-9 shows results for devices stressed at OFF-state bias (V_{GS} = −4 V; V_{DS} = 80 V) in an enclosed temperature chamber at a package temperature of 125 °C. Small negative Vth shifts are observed in Fig. 4-9(b). No significant degradation in G_M is observed. The V_{th} shifts are consistent with the activation of donor-like defects at elevated temperatures. Consistent with the results in Fig. 4-5, the charged donor-like defects responsible for the V_{th} shifts observed in Fig. 4-9 are not located closely enough to the 2DEG to scatter carriers strongly [65] [69].

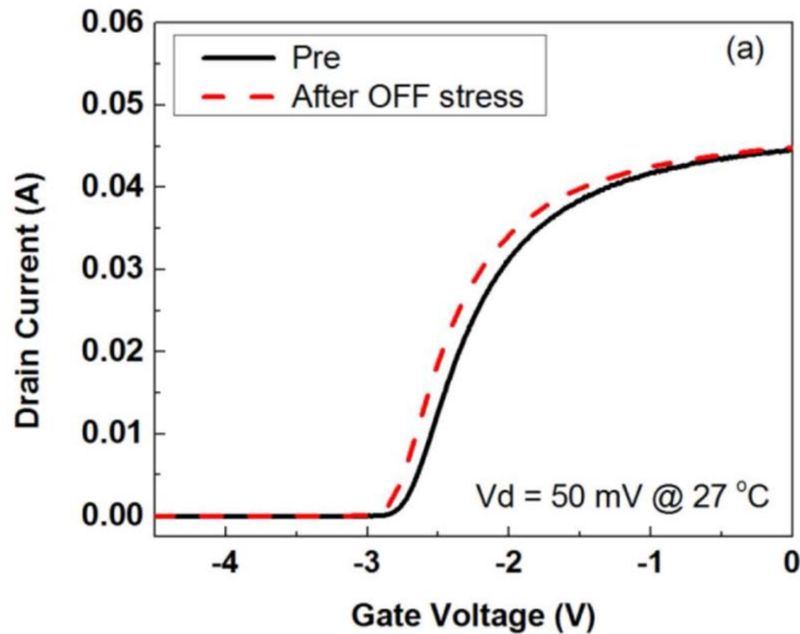

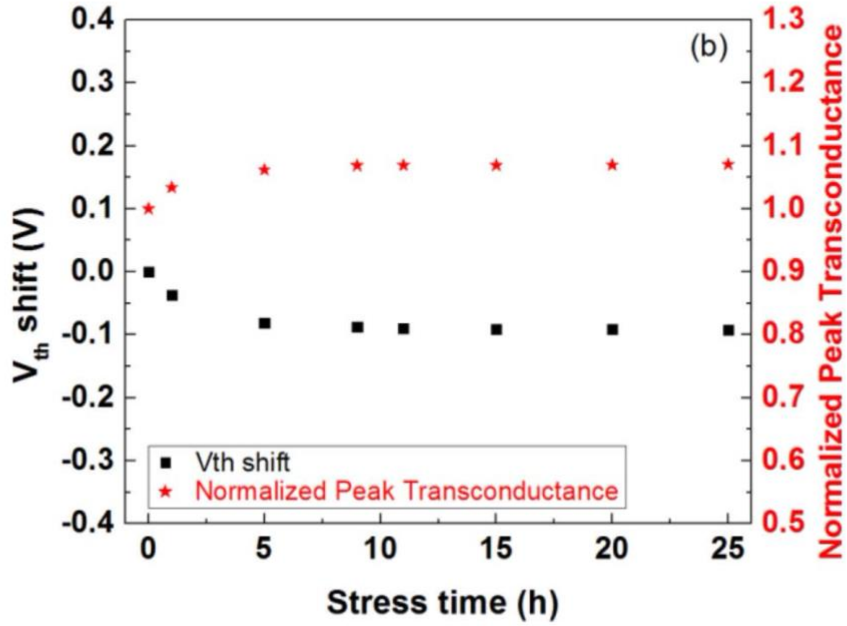

Fig. 4-9. (a) $I_d - V_g$ curves for AlGaN/GaN HEMTs at V_d = 50 mV before and after OFF-state bias stressing at a package temperature of 125 °C. Also shown are (b) threshold-voltage shift (left y-axis) and peak transconductance normalized to that of an unstressed device (right y-axis) for Group B devices stressed at 80 V drain bias (I_d ~ 60 μA) and -4 V gate bias (OFF state) at a package temperature of 125 °C. DC measurements are performed at 27 °C after devices are cooled for ~ 30 min.

Fig. 4-10 shows (a) $I_d - V_g$ curves and (b) threshold voltage shifts and peak transconductance as functions of time for AlGaN/GaN HEMTs stressed under ON-state bias conditions (V_{GS} = −0.5 V; V_{DS} = 30 V) in an enclosed temperature chamber at a package temperature of 79 °C. The results of Fig. 4-10(a) show significant degradation in ON-state current and negative Vth shifts after stresses of 14 and 39 h. Fig. 4-10(b) shows that V_{th} shifts positively by ~ 190 mV at stress times up to 0.5 h, and the peak transconductance increases significantly. At later times, a reversal in V_{th} shifts is observed, followed by increasingly more negative values of V_{th} with increasing stress time, reaching a shift of ~ −210 mV at 39 h. Degradation of more than 35% is observed in peak transconductance.

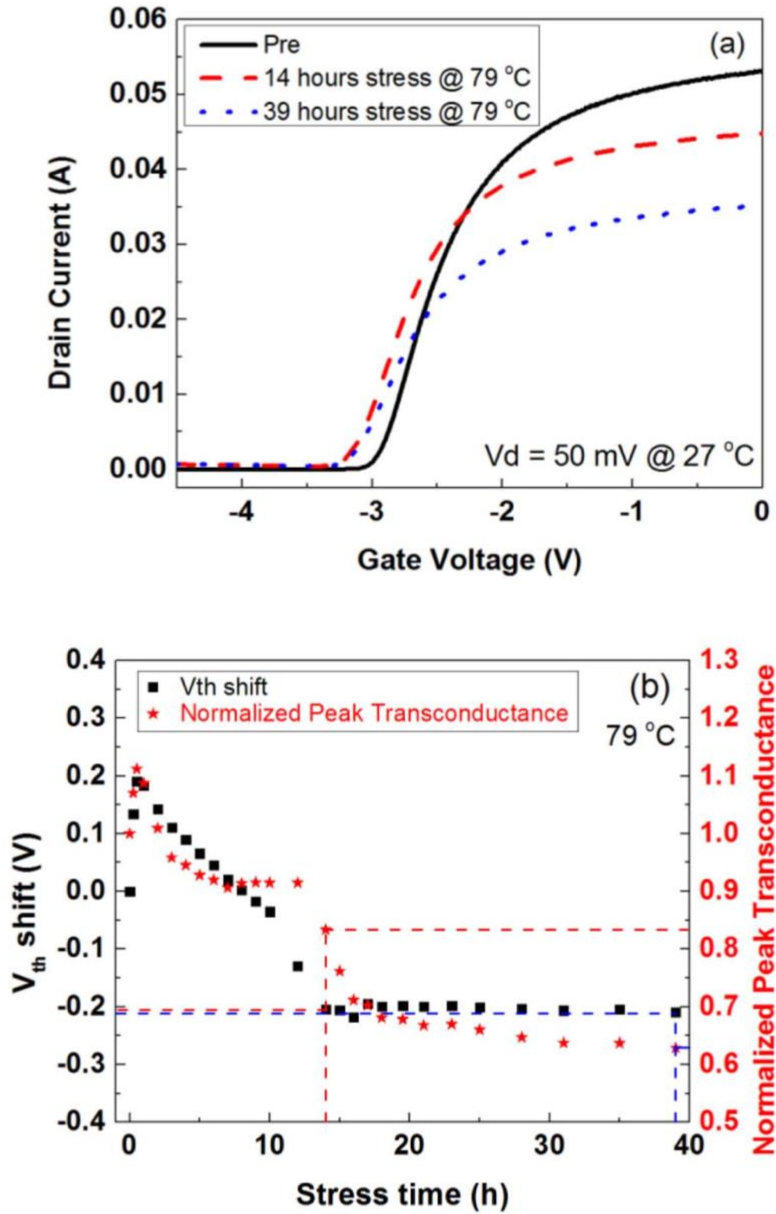

Fig. 4-10. (a) $I_d - V_g$ curves for AlGaN/GaN HEMTs at V_d = 50 mV before and after ON-state bias stressing at a package temperature of 79 °C. Also shown are (b) threshold-voltage shift (left y-axis) and peak transconductance normalized to that of an unstressed device (right y-axis) for Group B devices stressed at 30 V drain bias (∼7% above rated operating voltage limits; I_d ∼ 1.1 A) and −0.5 V gate bias (ON state) at a package temperature of 79 °C. DC measurements are performed at 27 °C after devices are cooled for ∼ 30 min. The dashed lines in Fig. 4-10(b) indicate points in the stressing sequence where noise measurements are performed, as discussed in Chapter VI.

Fig. 4-11 shows a device nominally identical to that of Fig. 4-10, stressed under similar bias conditions (V_{GS} = −0.5 V; V_{DS} = 30 V), but at a higher package temperature of 105 °C. Similar trends are observed in Vth shifts and evolution of peak transconductance as functions of time. No significant recovery of the V_{th} shifts or degradation in peak transconductance was observed after six days of room temperature annealing with all pins grounded, consistent with other studies [64], [65], [67], [69], showing the relative stability of these defects. Taken together, the results of Figs. 4-10 and 4-11 strongly suggest that the initial increases in V_{th} and evolution of peak transconductance result from the passivation of relatively low-energy donor-like defects located near the 2DEG in as-processed devices via electron capture [65]. The large negative V_{th} shifts and significant degradation in peak transconductance at longer stress times evidently are consistent with the subsequent generation of higher-energy donor-like defects with different microstructure, also located near the 2DEG [65], [69]. We discuss the likely nature of these defects in Chapter VI.

Fig. 4-12 shows (a) I_d – V_g curves and (b) threshold voltage shifts and peak transconductance as functions of time for AlGaN/GaN HEMTs stressed under semi-ON state bias conditions. The devices were stressed at a constant gate bias of − 2.5 V. The drain biases was 30 V at package temperatures of 79 °C and 100 °C, and 40 V at 125 °C. Values of V_{th} shift positively by ~ 50 mV after the full stress sequence. No significant degradation occurs in peak transconductance.

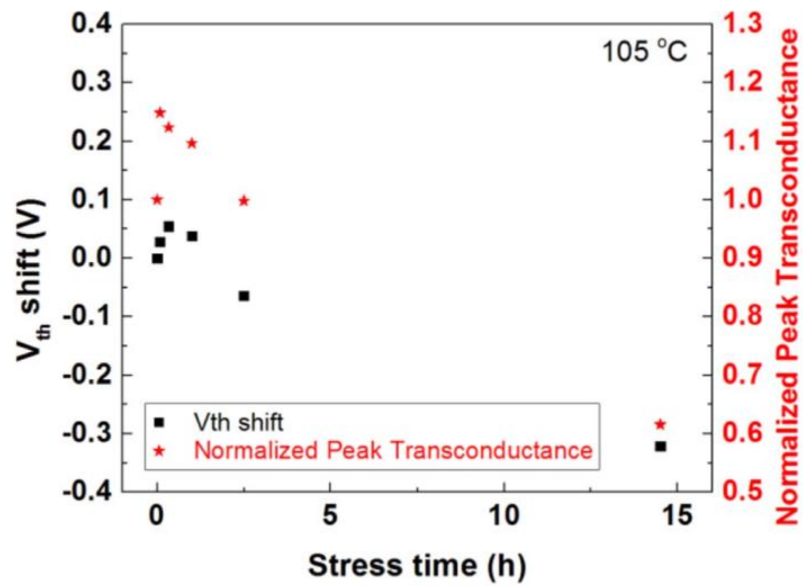

Fig. 4-11. V_{th} shift (left y-axis) and peak transconductance normalized to that of an unstressed device (right y-axis) for Group B devices stressed at 30 V drain bias (I_d ~ 1.12 A) and −0.5 V gate bias (ON state) at a package temperature of 105 °C. DC measurements are performed at 27 °C after devices are cooled for ~ 30 min.

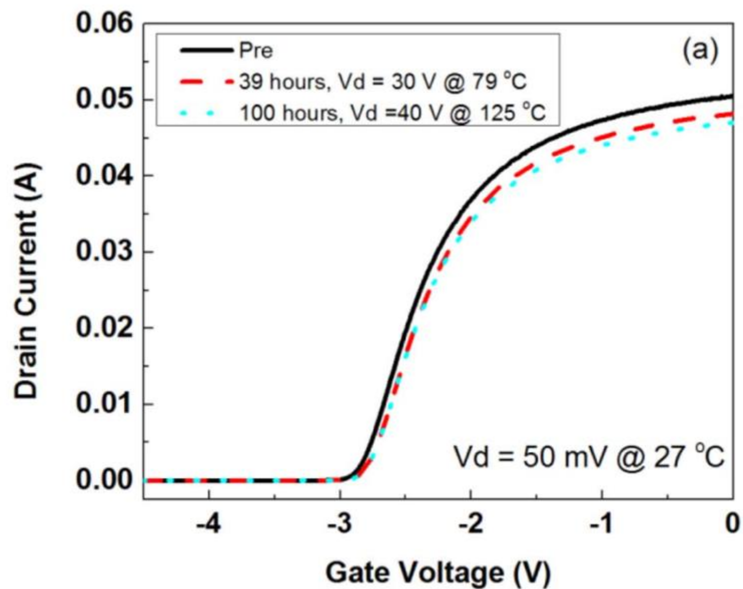

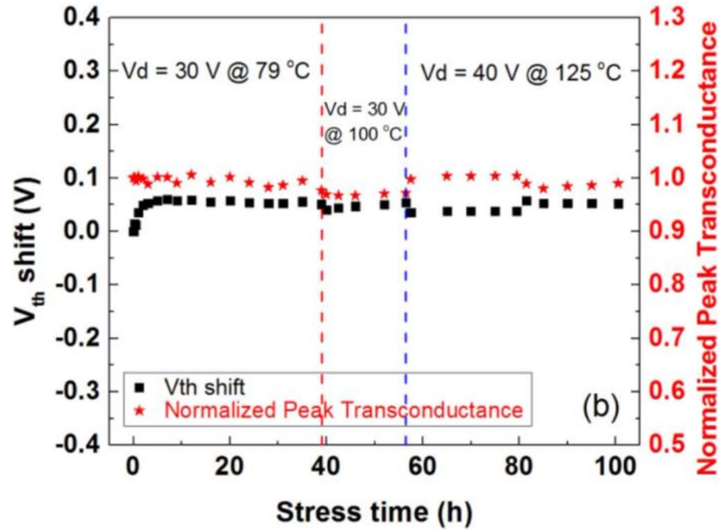

Fig. 4-12. (a) $I_d - V_g$ curves for AlGaN/GaN HEMTs at V_d = 50 mV before and after semi-ON state bias stressing at a package temperature up to 125 °C. Also shown are (b) threshold-voltage shift (left y-axis) and peak transconductance normalized to that of an unstressed device (right y-axis) for Group B devices stressed sequentially at drain biases up to 40 V (30% above rated voltage limits) with −2.5 V gate bias (semi-ON state) at a package temperature up to 125 °C. I_d ~ 228 mA at 125 °C. DC measurements are performed at 27 °C after devices are cooled for ~ 30 min.

4.3 Conclusions

We have investigated hot carrier stress effects at temperature up to 125 °C on industrial-quality GaN HEMTs. For stepped drain-bias stress testing, the direction of the Vth shift changes from positive to negative under OFF-state stress with increasing drain bias. The two different directions of Vth shift indicate that multiple kinds of defects are responsible for high-field and/or high-current stress-induced degradation. Unlike many previous results [63], [68], [78], [79], [80], the worst case for transconductance degradation for these devices under rated device operating conditions is ON bias condition at elevated temperatures.

Chapter V. Radiation response of GaN-based HEMTs

The radiation response and reliability of AlGaN/GaN HEMTs have attracted significant attention in recent years [66], [82], [84], [85], [86], [87], [88]. The sensitivity of AlGaN/GaN HEMTs to irradiation can be greatly enhanced when devices are biased during irradiation and/or high-field stress is applied before the exposure [66]. The lattice mismatch between AlGaN and GaN can lead to significant degradation due to stress-induced gate leakage [89], [90], [91], [92], [93], [94]. Lattice-matched, strain-free InAlN/GaN HEMTs are a potential solution to this problem [95], [96], [97], [98]. In addition, InAlN/GaN HEMTs provide higher two-dimensional electron gas concentrations than conventional AlGaN/GaN HEMTs [98], [99]. Hence, InAlN/GaN HEMTs are a potential alternative technology to AlGaN/GaN HEMTs for terrestrial and space electronics [100], [101], [102].

In this chapter, we evaluate the effects of 10-keV X-ray irradiation, 1.8 MeV proton irradiation, and high-voltage stress on three kinds of GaN HEMTs: two kinds of industrial-grade AlGaN/GaN HEMTs and one research-grade InAlN/GaN HEMT. The observed shifts in threshold voltage indicate the presence of donor-like defects during 10-keV X-ray irradiation and low-fluence proton irradiation. Higher-fluence proton irradiation generates acceptor-like defects. Acceptor-like defects are generated during combined 10-keV X-ray irradiation and high field stress.

5.1 Experimental details

The commercial AlGaN/GaN HEMTs under study were fabricated by Cree/Wolfspeed, Inc., and are listed as model numbers CGH40006P [44] and CGH40010F [81]. Ceramic lids

were removed from packages before irradiation. Research-grade In AlN/GaN HEMTs were fabricated on lattice-matched $In_{0.17}Al_{0.83}N$/GaN epitaxial structures with a 3-µm i-GaN layer, 2-nm AlN spacer layer, 18-nm $In_{0.17}Al_{0.83}N$ barrier layer, and 2-nm GaN cap layer, as shown in Fig. 5-1 [96].

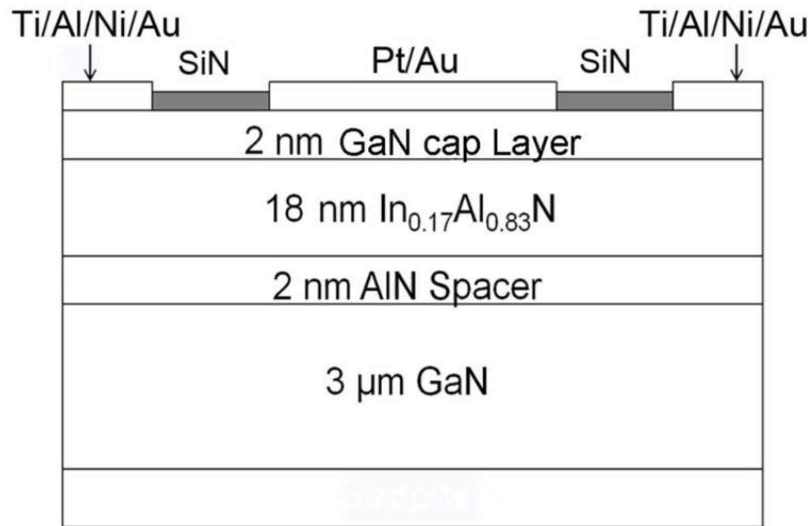

Fig. 5-1. Schematic diagram of InAlN/GaN HEMT structures (After [96]).

GaN HEMTs were irradiated with a 10-keV ARACOR x-ray source at a dose rate of 30.3 krad(SiO_2)/min as shown in Fig. 5-2 [39]. 1.8 MeV proton irradiations were performed up to a fluence of 1014/cm2 at a flux of 3 x 10^{10} protons/cm^2/s using the Pelletron accelerator at Vanderbilt University as shown in Fig. 5-3 [86]. DC measurements were performed using an Agilent B1505A parametric analyzer. The peak transconductance G_M is the maximum first-derivative point of the I_d-V_g curves; the threshold voltage V_{th} reported below is the gate voltage axis intercept of the linear extrapolation of the curve at that point [82], [83].

Fig. 5-2. 10-keV ARACOR 4100 X-ray irradiator.

Fig. 5-3. Pelletron accelerator at Vanderbilt University.

5.2 Experimental results and analysis

5.2.1 Radiation response

Fig. 5-4 compares I_d-V_g characteristics of commercial-grade (a) CGH40006P [44] and (b) CGH40010F [81] GaN-based HEMTs before and after exposure with 10-keV X-rays. All terminals of the device under test (DUT) were grounded during exposure. Changes in V_{th} and normalized peak transconductance G_M are shown in Fig. 5-5. Maximum negative Vth shifts of ~-0.06 V are observed for each device type when irradiated to 2 Mrad(SiO_2). A 1 h post-irradiation anneal reduces the shift to ~ -0.04 V. Less than 3% change is observed in normalized peak G_M. That the values of V_{th} shift negatively with irradiation and peak G_M increases during irradiation suggests that acceptor-like defects introduced during device processing most likely are passivated via the capture of radiation-induced holes [81], [88].

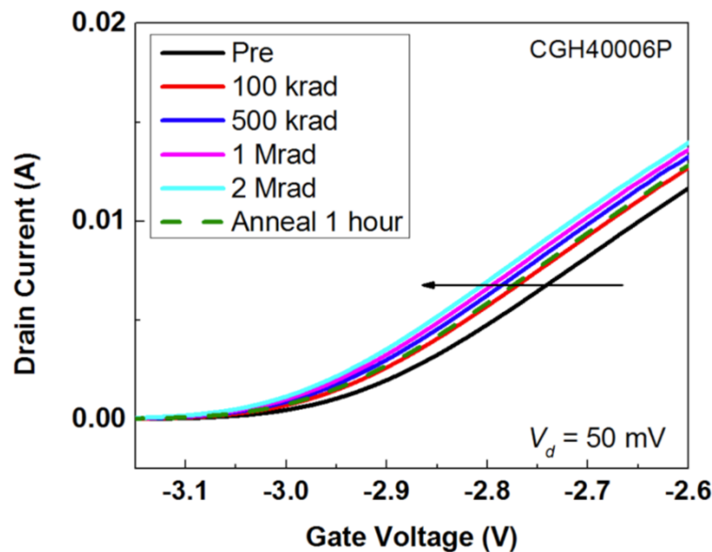

(a)

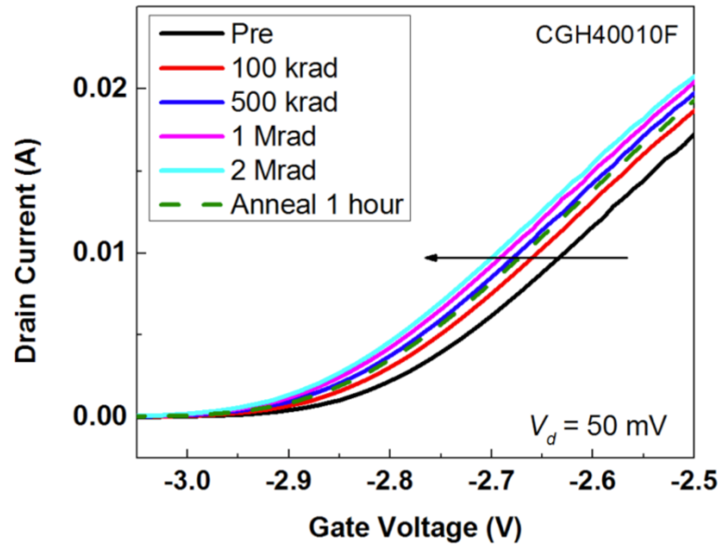

(b)

Fig. 5-4. I_d-V_g curves for (a) the CGH 40006P and (b) CGH 40010F AlGaN/GaN HEMTs before and after X-ray irradiations with all pins grounded.

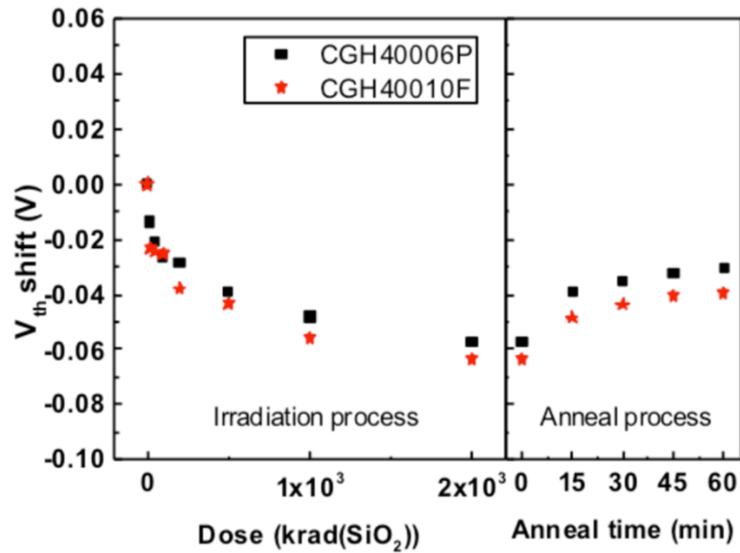

(a)

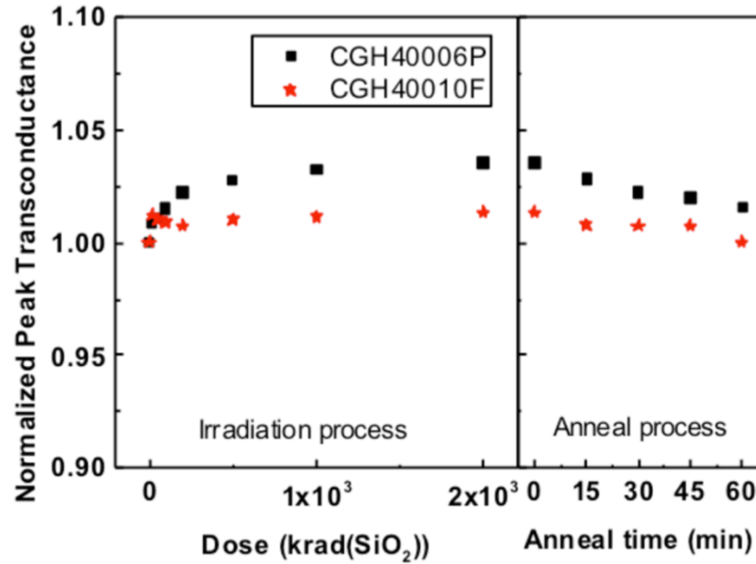

(b)

Fig. 5-5. Comparison of (a) threshold voltage shifts and (b) peak G_M normalized to the value of an unirradiated device as a function of TID and annealing time for CGH40006P and CGH40010F GaN-based HEMTs.

Fig. 5-6 shows ～10-keV X-ray irradiations of InAlN/GaN HEMTs with all pins grounded. No detectable changes are observed in the I_d-V_g characteristics. These results are similar to the responses of early generations of GaN-based HEMTs that showed no detectable change in device characteristics as a result of ionizing radiation exposure [84], [103], [104]. The relative insensitive of these research grade devices to ionizing radiation response may indicate that changes in densities of charged defects during irradiation are small compared with the densities in the as-processed devices, a trend consistent with the evolution of the responses of GaN-based HEMTs across technology generations [86], [88], [103], [104].

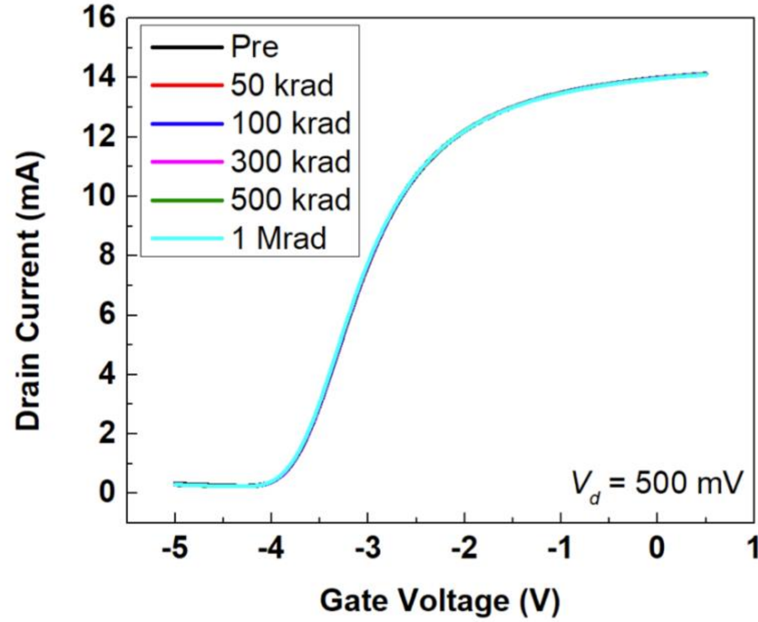

Fig. 5-6. I_d–V_g curves at V_d = 0.5 V for InAlN/GaN HEMTs before and after X-ray irradiation up to 1 Mrad(SiO_2) with all pins grounded.

Fig. 5-7 compares I_d-V_g characteristics for (a) CGH40006P [44] and (b) CGH40010F [81] GaN-based HEMTs before and after exposure with ~ 1.8 MeV protons. Changes in V_{th} and normalized peak transconductance are shown in Fig. 5-8. In Fig. 5-7 for each case, there is an initial negative shift in threshold voltage up to a fluence of $10^{13}/cm^2$ that is followed by a positive shift in threshold voltage up to $10^{14}/cm^2$. At lower fluences, trends in V_{th} shifts and peak G_M are consistent with those observed in Figs. 5-4 and 5-5, again consistent with the ionizing radiation-induced neutralization of acceptor-like defects in the as-processed devices [44], [88]. At higher fluences, however, the threshold voltage shifts positively, and the peak G_M degrades significantly. This response is consistently observed in GaN-based HEMTs at higher proton fluences, and has been attributed to the creation of N-vacancy-related acceptor defects as a result of proton-irradiation-induced displacement damage [44], [87], [105]. The

radiation-induced shifts are not large enough in Figs. 5-7 and 5-8 to be of significant concern for practical space environments [66], [86], [88].

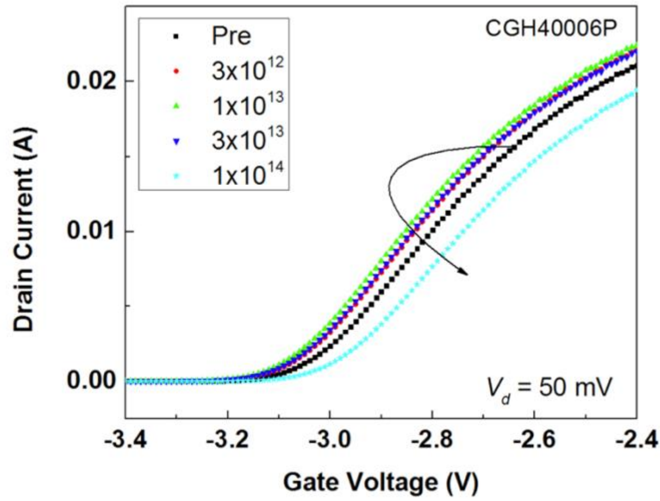

(a)

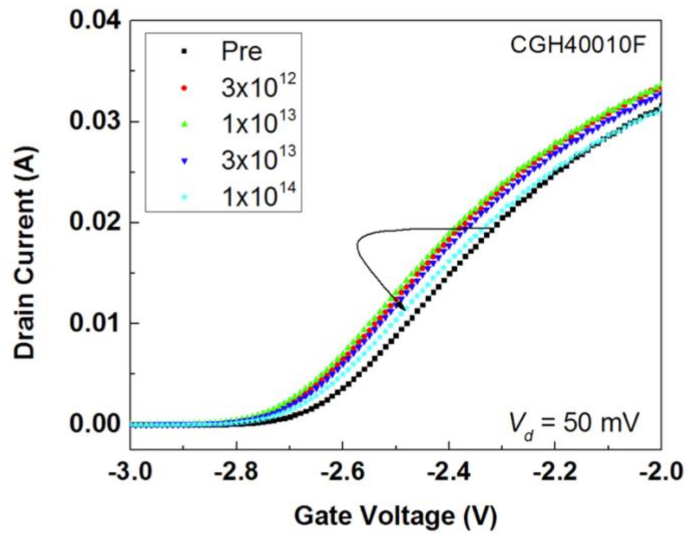

(b)

Fig. 5-7. I_d-V_g curves for (a) CGH40006P and (b) CGH40010F GaN-based HEMTs before and after 1.8-MeV proton irradiation up to a fluence of $10^{14}/cm^2$ with all pins grounded.

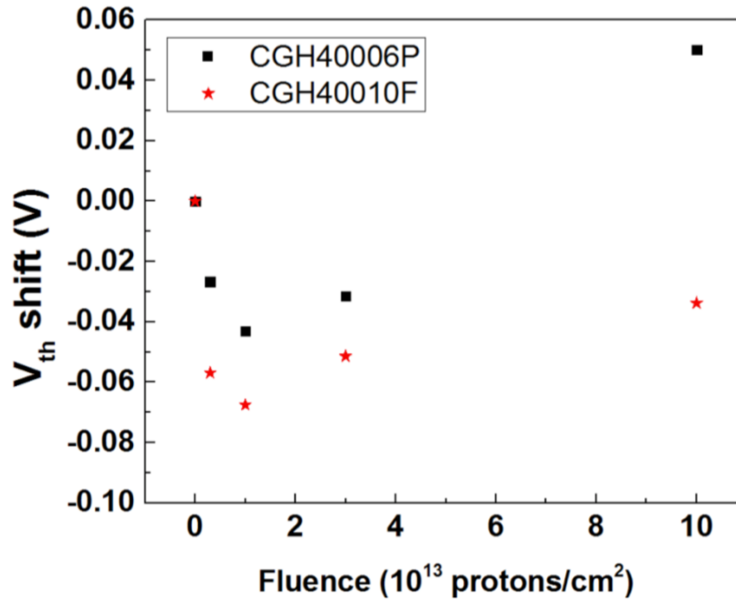

(a)

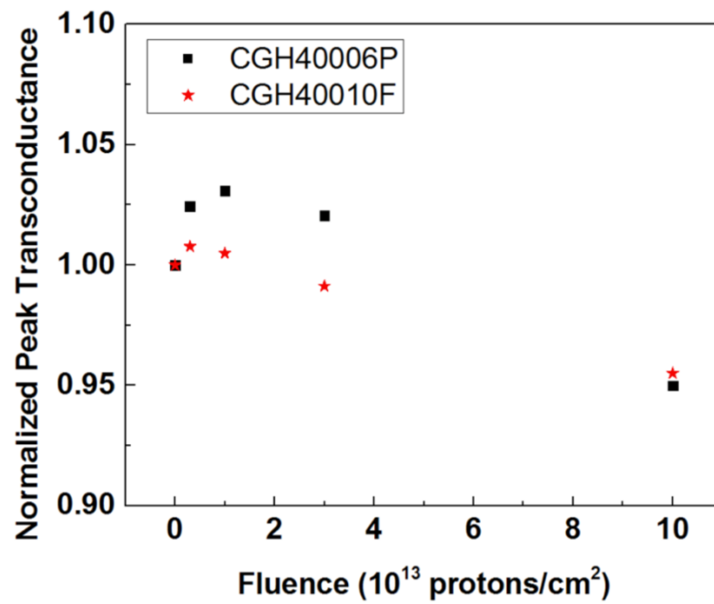

(b)

Fig. 5-8. (a) V_{th} shifts and (b) normalized peak transconductance as a function of proton fluence CGH40006P and CGH40010F GaN-based HEMTs before and after 1.8-MeV proton irradiation up to 10^{14}/cm^2 with all pins grounded.

5.2.2 Bias-stress effects in InAlN/GaN HEMTs

The response of research-grade InAlN/GaN HEMTs subjected to voltage stress with V_{ds} = 20 V at room temperature under representative ON (V_{gs} = 1 V), semi-ON (V_{gs} = -3 V), and OFF (V_{gs} = -5 V) conditions is shown in Fig. 5-9. A large positive Vth shift (～ 1.2 V at a stress time of 12 h) is observed in devices stressed under ON-state bias, and a ～0.4 V Vth shift is observed for OFF and semi-ON state stresses. In Fig. 5-9(b), peak G_M is reduced by up to 65% for InAlN/GaN HEMTs stressed under the worst-case ON bias condition. These large shifts in V_{th} and significant degradation in peak G_M are consistent with the net activation of a significant density of acceptor-like defects under the applied bias conditions. These bias-stress-induced shifts are much larger than those observed at much higher stressing voltages and temperatures for commercial-grade CGH40006P and CGH40010F GaN-based HEMTs in [81]. The shifts are more comparable to those of research-grade GaN-based HEMTs at similar stages of development [65], [67], [106]. Comparing these results with Fig. 5-6 demonstrates that the application of bias stress is more effective in activating or creating defects in these devices than ionizing radiation exposure of 2 Mrad(SiO_2).

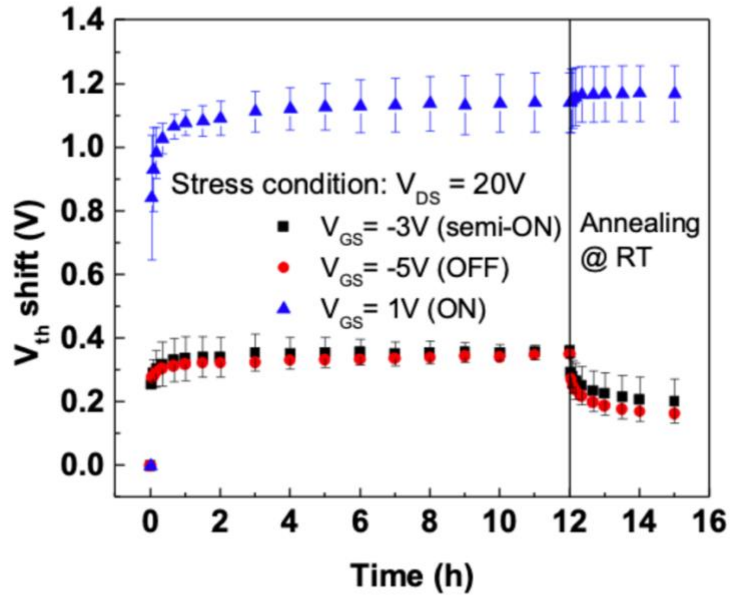

(a)

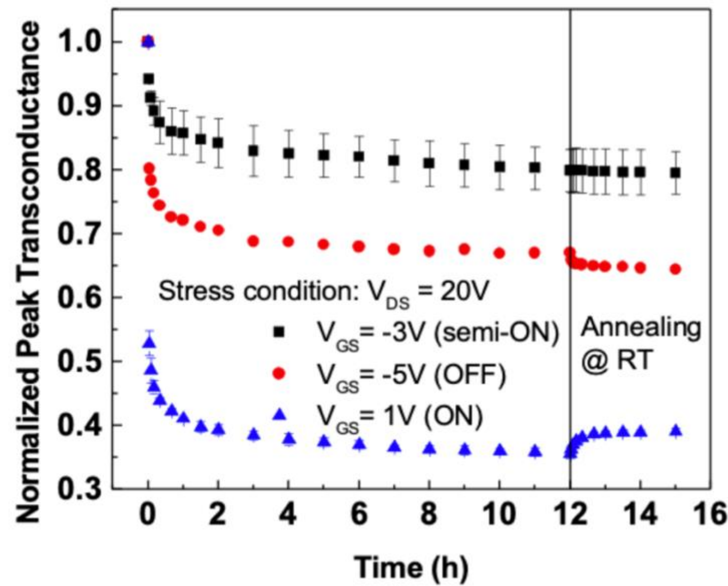

(b)

Fig. 5-9. (a) V_{th} shifts and (b) normalized peak G_M vs. time for InAlN/GaN HEMTs stressed under ON (V_{gs} = 1 V), Semi-ON (V_{gs} = -3 V), and OFF (V_{gs} = -5 V) conditions (V_{ds} = 20 V). Post-stress annealing was performed at room temperature with all pins grounded. Error bars represent the standard deviations of the responses of identical devices.

5.2.3 Combined high-field stress and irradiation

To determine whether there are potential interactions between radiation- and stress-induced defects, Figs. 5-10 and 5-11 show the responses of InAlN/GaN HEMTs to sequential bias stress and 10-keV X-ray irradiation. Devices were biased in the ON condition through the full sequence (V_{ds} = 8 V and V_{gs} = 1 V). A significantly lower drain voltage was selected for this study to limit stress-induced degradation to amounts of more practical interest. In Fig. 5-10, devices were first subjected to ON-state stress for 5 h and then irradiated to 1 Mrad(SiO_2). This combination of bias stress and irradiation to a 0.05 V shift in V_{th} and a 15% degradation in peak G_M, consistent with the net activation of acceptor-like defects. Fig. 5-11 reverses the order of the irradiation and bias stress. After irradiation bias stress, devices show a -0.1 V shift in V_{th} and an 8% improvement in peak G_M, consistent with the net passivation of acceptor-like defects. Such a complex interplay was also observed for AlGaN/GaN HEMTs subjected to bias stress and then proton irradiation, and vice versa [66]. In that case, enhanced degradation in commercial-grade devices was also observed when devices are first stressed and then irradiated, for reasons that are not yet understood [66]. These results suggest this behavior may be more general in nature, and certainly warrants additional study.

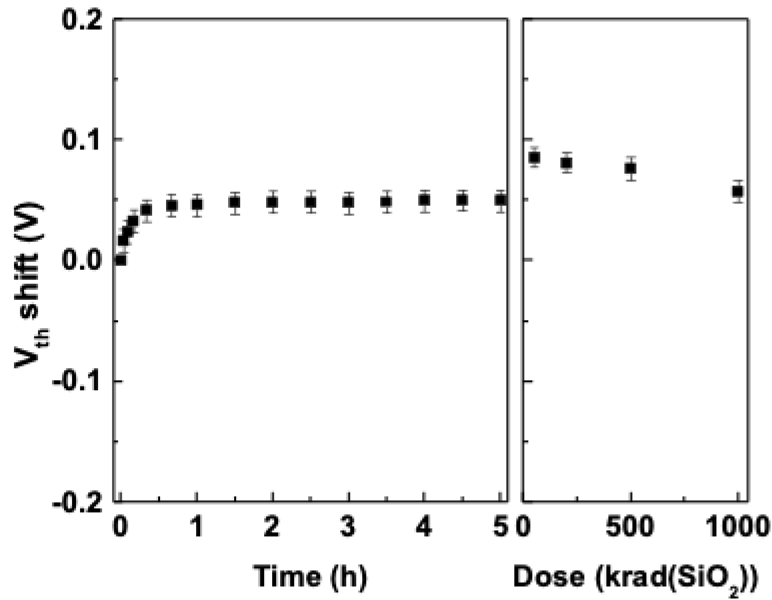

(a)

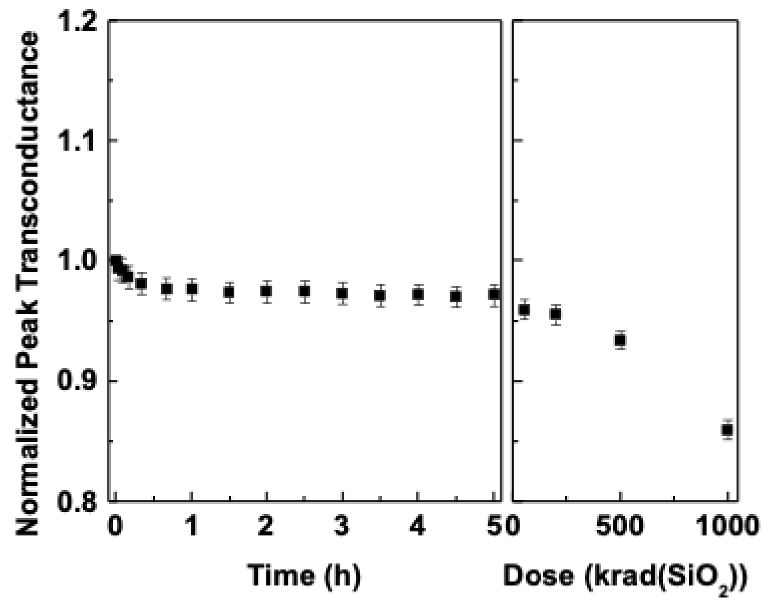

(b)

Fig. 5-10. (a) Threshold voltage shifts and (b) normalized peak transconductance of InAlN/GaN HEMTs as a function of time during high field stress and irradiation. Devices are first stressed and then irradiated at biases of V_{ds}= 8 V and V_{gs} = 1 V.

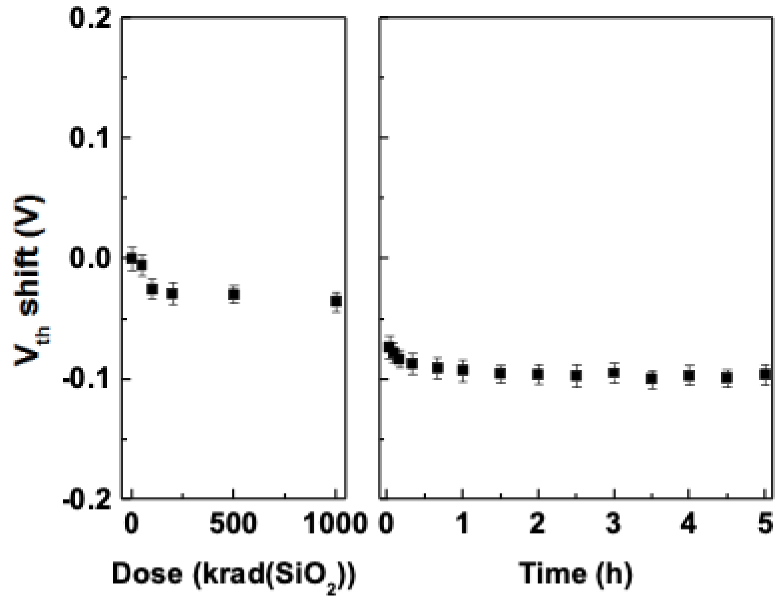

(a)

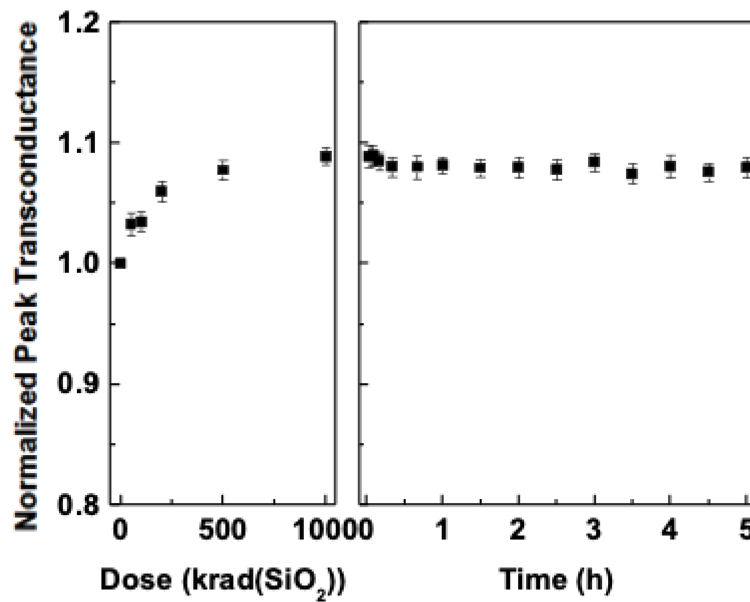

(b)

Fig. 5-11. (a) Threshold voltage shifts and (b) normalized peak G_M of InAlN/GaN HEMTs as a function of irradiation and time during high field stress. Devices are first irradiated and then stressed at biases of V_{ds}= 8 V and V_{gs} = 1 V.

5.3 Conclusions

Commercial AlGaN/GaN HEMTs from the same manufacturer show similar responses to 10-keV X-ray irradiation and 1.8-MeV proton irradiation. Devices show negative threshold voltage shifts during 10-keV X-ray irradiation, and during proton irradiation at low fluences. At higher fluences, devices behave positive V_{th} shifts. We have investigated the combined effects of X-ray irradiation and hot carrier stress on research-grade InAlN/GaN HEMTs. Both the bias during X-ray irradiation and the application of high-field stress before X-ray exposure can significantly increase the sensitivity of InAlN/GaN HEMTs. The ionization-equivalent dose for 1.8 MeV protons at a fluence of 10^{13} /cm^2 is much larger, ~ 20 Mrad(SiO_2) [105], [106]. This indicates that either the rate of donor-like defect activation during the proton irradiation is lower than during 10-keV X-ray irradiation, or that compensating acceptor-like defects are also generated during 1.8-MeV proton irradiation.

Chapter VI. Low frequency noise of GaN-based HEMTs

To obtain insight into the defects in the devices, low frequency noise measurements are performed using a Stanford Research SR 760 FFT spectrum analyzer [107], [108], [109], [110]. Fig. 6-1 shows the low frequency noise measurement setup [111], [112], [113], [114].

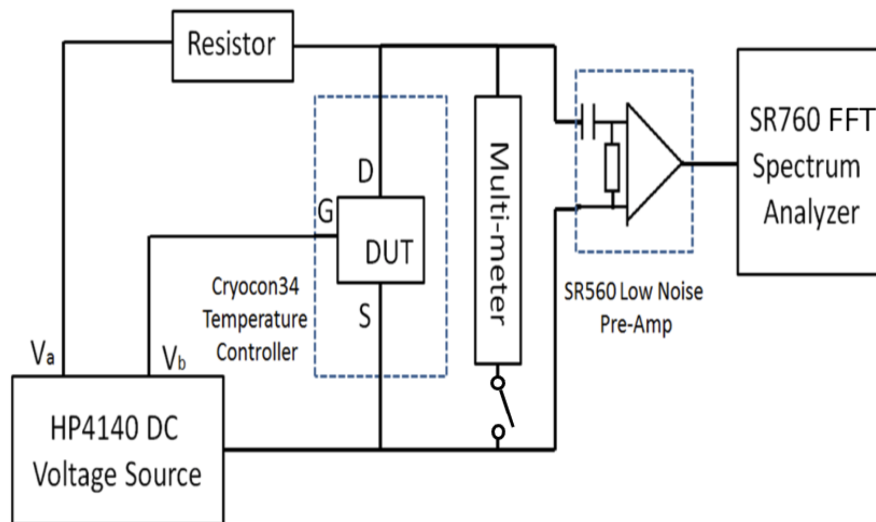

Fig. 6-1. Low frequency noise measurement system.

6.1 Temperature dependent noise results and discussion

Fig. 6-2 shows the excess drain voltage noise power spectral density S_V (corrected for background noise) as a function of frequency at constant $V_{gs} - V_{th}$ =0.5 V and V_{ds} = 0.05 V before and after ON state bias stress (V_{GS} = -0.5 V, V_{DS} = 30 V at a package temperature of

Adapted with permission from P. F. Wang *et al.*, *IEEE Trans. Dev. Mater. Reliab.*, vol. 20, no. 2, pp. 420-428, Jun. 2020.

79 °C for 39 hours) at 300 K for a Wolfspeed CGH40010F AlGaN/GaN HEMT. The biases chosen in this work ensure that the noise originates primarily from the gated portion of the channel [57] [107]. The frequency exponent α is defined as

$$\alpha = -\partial(\ln S_V) / \partial(\ln f). \tag{6.1}$$

As shown in Fig. 6-2, the noise varies approximately inversely with frequency above 10 Hz. The deviation of the spectra from a 1/*f* power law is consistent with the inferred non-uniformity in defect energy distribution [107], as we now demonstrate.

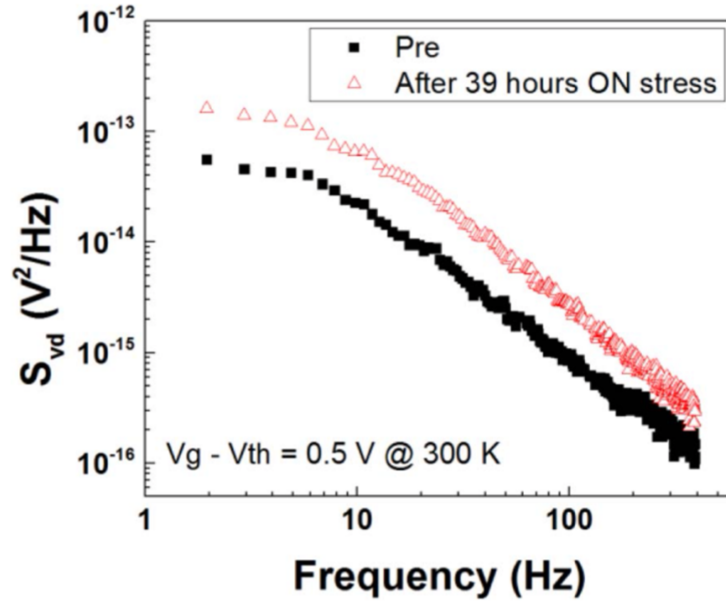

Fig. 6-2. Excess voltage noise power spectral density S_{vd} (corrected for background noise) as a function of frequency for the AlGaN/GaN HEMTs before and after ON state bias stress (V_{GS} = -0.5 V, V_{DS} = 30 V at a package temperature of 79 °C for 39 hours) at 300 K. $V_{gs} - V_{th}$ = 0.5 V, and V_{ds} = 0.05 V.

Dutta and Horn have shown that, if the noise is caused by a random thermally-activated process having a broad distribution of energies *D(E)* relative to *kT*, where *k* is the Boltzmann

constant and T is the temperature, the frequency and temperature dependences of the noise are related causally via [115], [116], [117], [118]:

$$\alpha(\omega,T) = 1 - \frac{1}{\ln(\omega\tau_0)}\left(\frac{\partial \ln S_V(T)}{\partial \ln T} - 1\right). \tag{6.2}$$

Here $\omega = 2\pi f$, and t_0 is the characteristic time of the process leading to the noise (here taken to be ~ 3×10^{-14} s [87], [107]). From measurements of the temperature dependence of S_V , we estimate the defect-energy distributions $D(E_0)$ [119], [120], [121], [122] via

$$D(E_0) \propto \omega/(kT) * S_V, \tag{6.3}$$

Where

$$E_0 \approx -kT\ln(\omega\tau_0) \tag{6.4}$$

is the effective defect activation energy.

Fig. 6-3 shows the (a) threshold voltage and (b) peak transconductance as a function of measurement temperature for AlGaN/GaN HEMTs before and after ON state bias stress (V_{GS} = -0.5 V, V_{DS} = 30 V at a package temperature of 79 °C for 39 hours). As the temperature increases from ~ 80 K to ~ 400 K in Fig. 6-3(a), V_{th} decreases by ~ 670 ± 30 mV (~ 2 mV/K) for both the stressed and unstressed devices in Fig. 6-3(a); values of peak transconductance decrease by ~ 67% ± 3% in Fig. 6-3(b). These rates of decrease of V_{th} and peak transconductance with temperature are typical for Schottky gate GaN-based HEMTs [123], [124], [125], [126]. The rates of change with temperature observed for these devices are largely unaffected by stress-induced defects.

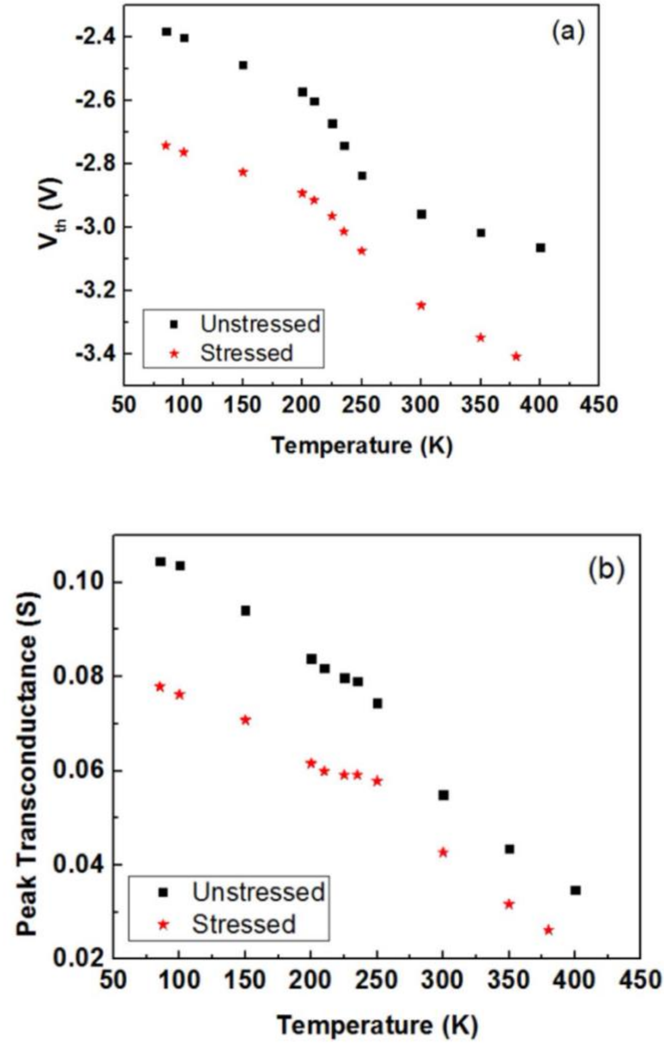

Fig. 6-3. Temperature dependence of (a) threshold voltage and (b) peak transconductance for AlGaN/GaN HEMTs before and after 39 hours under ON-state bias stress conditions (V_{GS} = -0.5 V, V_{DS} = 30 V at a package temperature of 79 ^{o}C).

Fig. 6-4 shows the excess drain-voltage noise power spectral density S_{Vd} (corrected for background noise) as a function of temperature, before and after devices were stressed under (a) OFF (V_{GS} = -4 V, V_{DS} = 80 V at a package temperature of 125 ^{o}C for 25 hours), (b) ON (V_{GS} = -0.5 V, V_{DS} = 30 V at a package temperature of 79 ^{o}C for 14 hours and 39 hours totally), and (c) Semi-ON (V_{GS} = -2.5 V, V_{DS} = 30 V at a package temperature of 79 ^{o}C for 39 hours,

and V_{DS} = 40 V at a package temperature of 125 °C for additional 44 hours) bias conditions. The temperature range (bottom x-axis) is related to the activation energy scale (top x-axis) via Eq. (6.3). This relation is justified by the results of Fig. 6-5, which shows that the measured values of frequency exponent α from the noise data for unstressed and stressed (V_{GS} = -0.5 V, V_{DS} = 30 V at a package temperature of 79 °C for 39 hours) devices are in general agreement with Eq. (6.2), justifying the use of the Dutta-Horn model [57], [107].

Returning to Fig. 6-4, for cases (a)-(c) the pre-stress noise decreases between 80 K and ~ 225 K. A large peak in noise magnitude is centered at ~ 320 K. This latter peak is consistent with the deviation from power-law response in Fig. 6-2, since the frequency dependence, temperature dependence, and gate-voltage dependence of the noise are affected similarly by non-uniformities in the defect energy distribution [107], [112], [127].

Only in the ON state condition in Fig. 6-4(b) are significant increases in noise magnitude observed for the stressed devices. In Fig. 6-4(b) a large increase in noise over the full range of temperatures is observed during the first 14 h stress, consistent with the generation of a broad range of defects [65]. The increase in effective defect density in Fig. 6-4(b) is consistent with the increase in peak transconductance degradation that occurs over the same stressing interval, consistent with the results of Fig. 4-10(b) and previous studies [65], [67]. These results reinforce the close link between the defects observed during noise measurements and the defects that cause the observed degradation in device response [67], [107], [108].

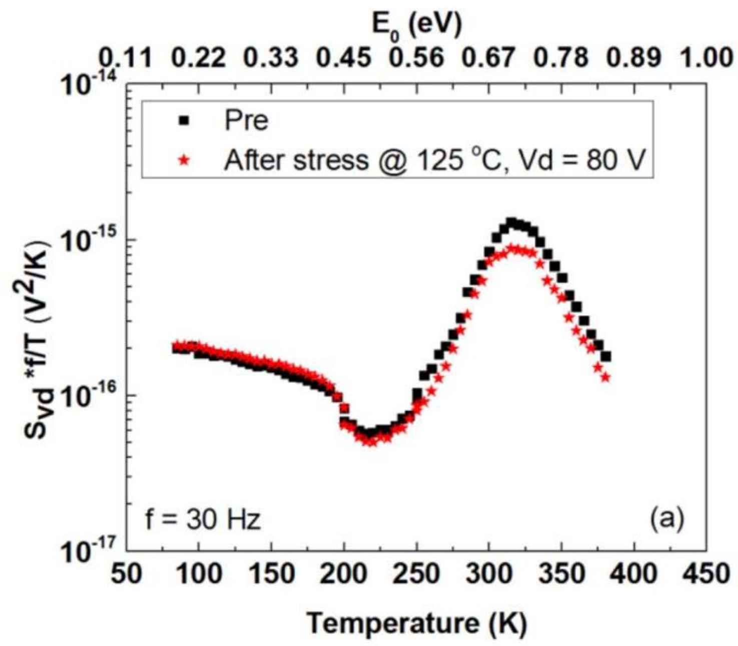
E0 (eV)
0.11 0.22 0.33 0.45 0.56 0.67 0.78 0.89 1.00
Pre
After stress @ 125 °C, Vd = 80 V
Svd *f/T (V2/K)
f = 30 Hz
(a)
Temperature (K)

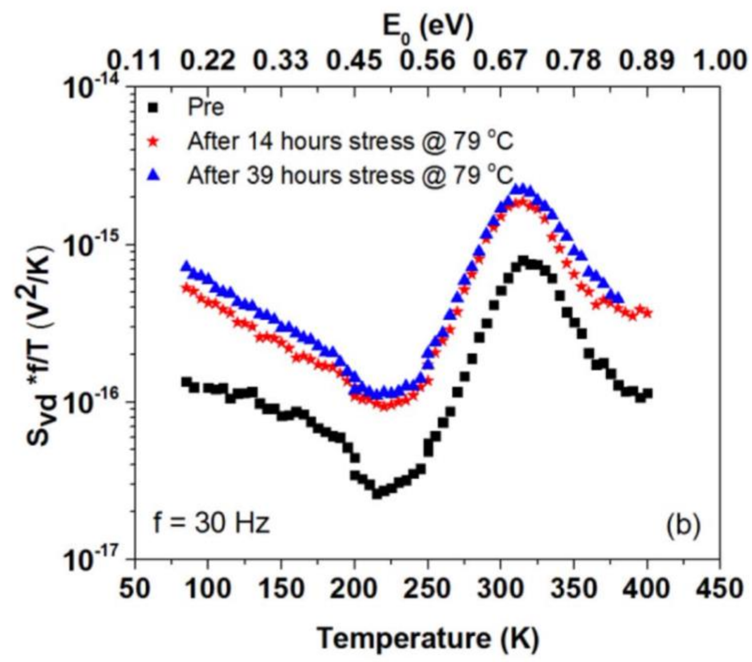
E0 (eV)
0.11 0.22 0.33 0.45 0.56 0.67 0.78 0.89 1.00
Pre
After 14 hours stress @ 79 °C
After 39 hours stress @ 79 °C
Svd *f/T (V2/K)
f = 30 Hz
(b)
Temperature (K)

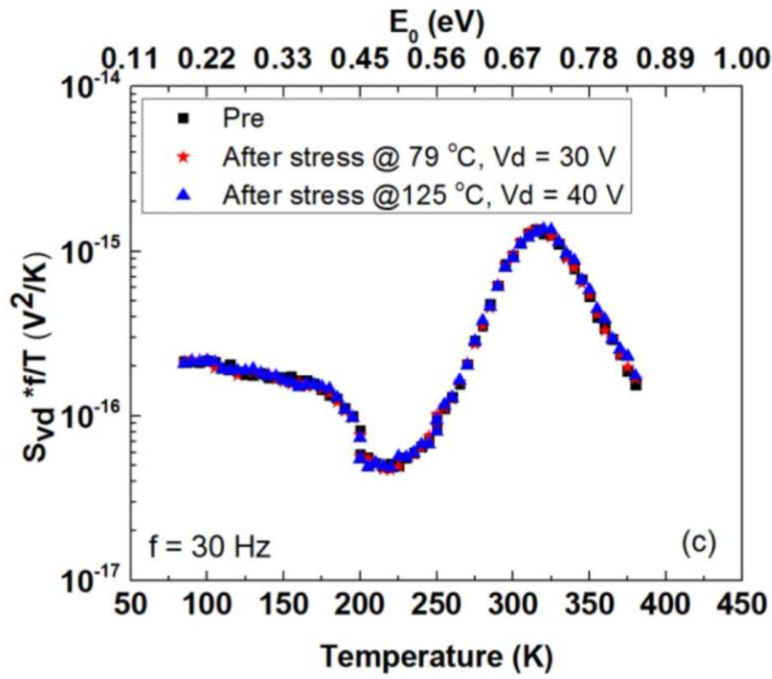

Fig. 6-4. Normalized excess drain-voltage noise $S_V f/T$ from 85 K to 400 K, for f = 30 Hz. Here $V_{gs} - V_{th}$ = 0.5 V, V_d = 0.05 V. The temperature range corresponds to an activation energy scale on the upper x-axis derived from Eq. (6.4). The stress bias conditions are (a) OFF state (V_{GS} = -4 V) for 25 hours, (b) ON state (V_{GS} = -0.5 V) up to 39 hours and (c) semi-ON state (V_{GS} = -2.5 V) up to 100 hours.

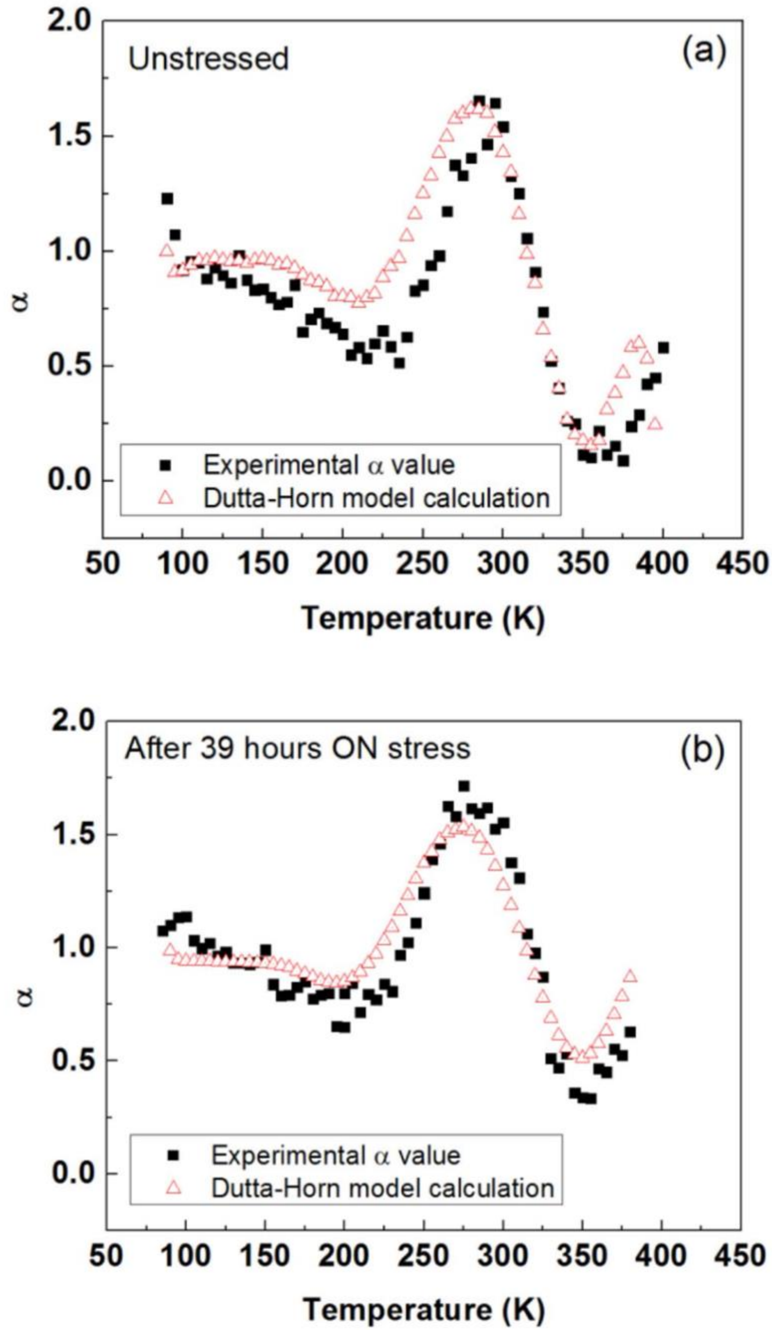

Fig. 6-5. Experimental (from Eq. (6.1)) and calculated (from Eq. (6.2)) frequency exponents α for (a) unstressed devices and (b) devices stressed in the ON state (V_{GS} = -0.5 V, V_{DS} = 30 V at a package temperature of 79 ^{o}C for 39 hours), verifying the applicability of the Dutta-Horn model in these cases. Similar agreement between measured and calculated values of α were observed for all tested devices in this study.

The most prominent defects contributing to low-frequency noise are those associated with the plateaus in noise magnitudes observed at ~ 0.2 eV to ~ 0.4 eV (~ 100-200 K) and the broad peak centered at ~ 0.72 eV ± 0.05 eV (~ 275 ± 10 K), and ranging from ~ 0.5 eV (~ 225 K) to ~ 0.8 eV (~ 375 K). These defects are denoted empirically as *D* and *Ax* centers in early work by Fang *et al.* [77]. We first consider the low temperature plateau at ~ 0.2 eV to ~ 0.4 eV that is often observed in AlGaN/GaN HEMTs. The elevated noise magnitude in this temperature range is often attributed to oxygen-impurity related DX centers, specifically, to fluctuations between the low-temperature equilibrium, charged $(O_N)^-$ state and the excited neutral O_N state [65], [128]. This defect is donor-like, so as the temperature increases, the equilibrium state becomes the neutral O_N state, consistent with the rapid decrease in V_{th} from 200-275 K in Fig. 6-3(a). Hence, the initial rise in noise magnitude that begins in Fig. 6-4 at ~ 0.5 eV likely results from to fluctuations between the neutral (O_N) state to the excited, charged $(O_N)^+$ state [65], [128].

The continuing rise in the large peak centered at ~ 0.7 eV may well result primarily from a second defect. The only relatively common defect occurring in as-grown GaN that exhibits both the appropriate charge state and energy level to account for the large peak centered at ~ 0.72 ± 0.05 eV appears to be the N antisite, N_{Ga} [65], [129] which is an acceptor-like defect. It is therefore likely that both donor-like and acceptor-like defects are contributing to the noise near and above room temperature in these devices.

Given that donor defects dominate the degradation of these devices under stress, it is likely that the O_N-related defects are dominating the device degradation. These are common impurity defects in both the AlGaN and the GaN buffer layers [79], [129]. N_{Ga} acceptor defects evidently play a prominent role in the noise, particularly in the as-processed devices,

but a secondary role in the stress-induced degradation. Consistent with this interpretation, we note that N_{Ga} acceptor defects have been shown to be affected by proton irradiation less significantly than O_N donors in previous work [66].

Defects that are introduced during growth often are initially passivated by hydrogen. During high-field and/or high-current stress, hot electrons can remove hydrogen from the defects. It has been shown in proton irradiation experiments that dehydrogenation of an O_N-H complex can lead to an increase in the low-temperature noise magnitude and an associated decrease in peak transconductance degradation [66], [76]. This dehydrogenation process evidently leads to significant increases in noise magnitudes in these devices after stress, shown in Fig. 6-4(b), and is therefore likely to be the dominant, reliability-limiting mechanism in these devices. We similarly attribute the increases in the ~0.72 eV defect level to hydrogen removal from hydrogenated antisite $N_{Ga} - H_x$, $x = 1 - 3$, defects [66], [67].

6.2 Gate-voltage dependent noise results and discussion

Fig. 6-6 shows the excess low-frequency drain-voltage noise power spectral density S_{vd} at constant $V_g - V_{th} = 0.5$ V and $V_d = 0.05$ V as a function of frequency f for (a) CGH40006P [44] and (b) CGH40010F [81] GaN-based HEMTs before and after proton irradiation. Fig. 6-7 summarizes results measured at 30 Hz for the two kinds of devices. The voltage dependence of the noise of GaN-based HEMTs can be characterized by the slopes of curves, β_1 and β_2, in the low and high-voltage regions of the curves, respectively, as described in detail in [130] and illustrated in Fig. 6-7. Both the noise magnitudes and values of β_1 and β_2 decrease slightly after proton irradiation for each type of device. These small decreases in noise magnitude are often observed near room temperature for GaN-based HEMTs [66], [130], and are consistent

with the conversion of O_N-H impurity complexes in as-processed devices to O_N impurities in irradiated devices, as a result of proton-induced defect dehydrogenation. Hence, this result is consistent with an increase in density of O_N donors during proton irradiation.

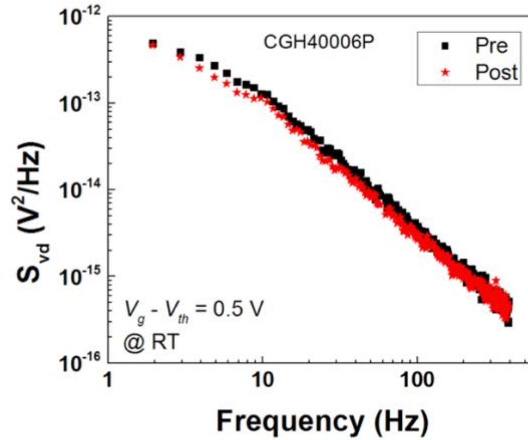

(a)

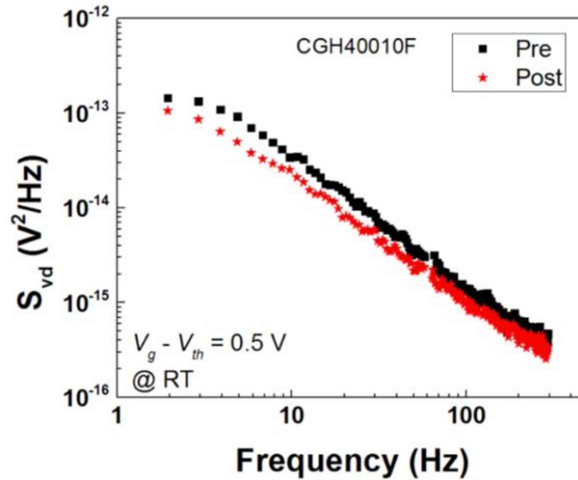

(b)

Fig. 6-6. S_{Vd} as a function of f for (a) CGH 40006P and (b) CGH 40010F GaN-based HEMTs before and after proton irradiation up to 1 x 10^{14}/cm^2 with all pins grounded. V_g - V_{th} = 0.5 V, and V_d = 0.05 V during the noise measurements.

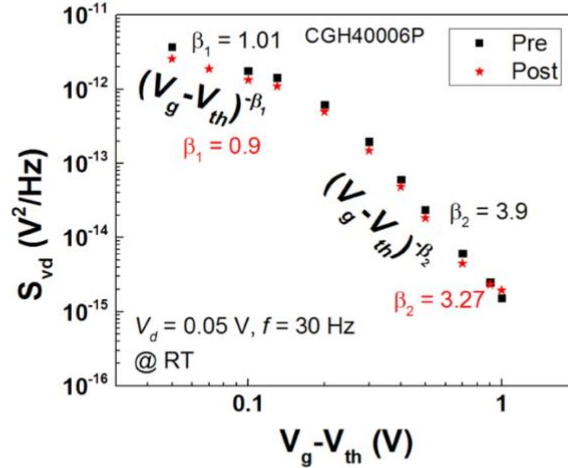

(a)

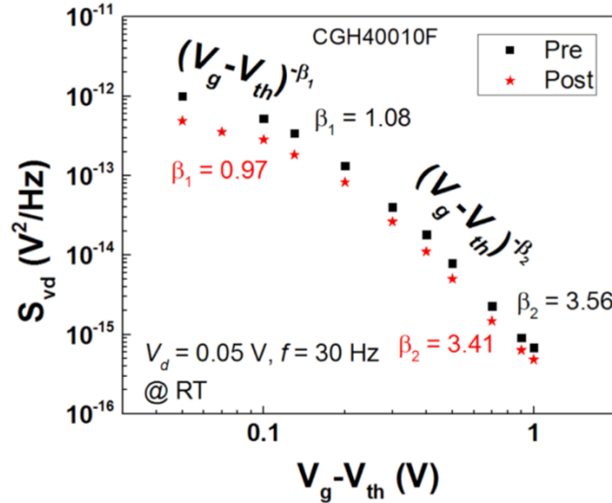

(b)

Fig. 6-7. S_{Vd} at 30 Hz as a function of $V_g - V_{th}$ for (a) CGH 40006P and (b) CGH 40010F GaN-based HEMTs before and after proton irradiation up to 10^{14}/cm^2 with all pins grounded. $V_d = 0.05$ V during the noise measurements.

Fig. 6-8 shows S_{vd} as a function of $V_g - V_{th}$ at 30 Hz at room temperature for InAlN/GaN-based HEMTs for (a) the bias-stress ($V_{GS} = 1$ V, $V_{DS} = 8$ V for 5 hours) and irradiation sequence of Fig. 5-10, and (b) the irradiation and stress ($V_{GS} = 1$ V, $V_{DS} = 8$ V for 5 hours) sequence of Fig. 5-11. The noise magnitudes increase only slightly after irradiation and/or

high field stress in each case. Despite the significant differences in peak G_M in Figs. 5-10(b) and 5-11(b), no significant differences are observed in the room temperature noise magnitudes for the range of accessible measurement frequencies. Hence, either the defects responsible for the reduced degradation do not change charge states on the time scales of these measurements, or the changes in charge state occur so rapidly (e.g., on time scales less than ~1 ms) [107].

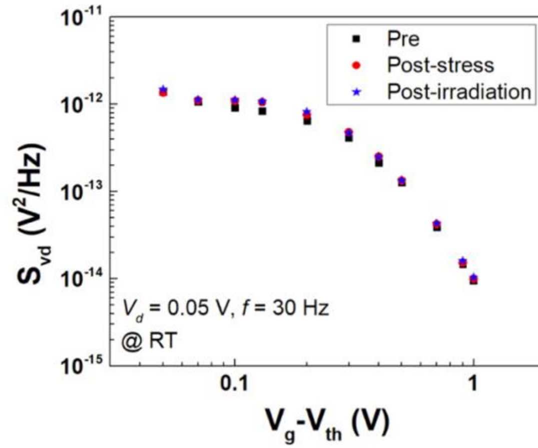

(a)

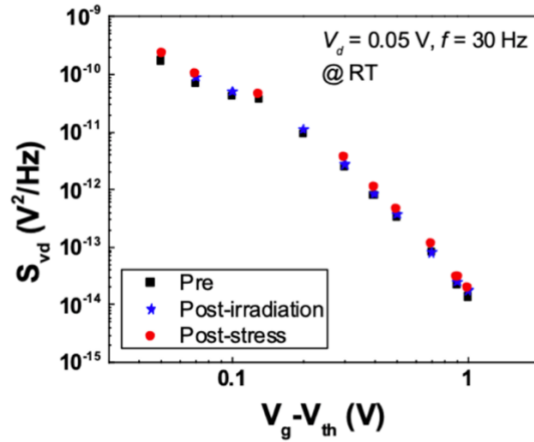

(b)

Fig. 6-8. S_{Vd} at 30 Hz as a function of $V_g - V_{th}$ for ON state irradiation (a) after and (b) before ON stress (V_{GS} = 1 V, V_{DS} = 8 V for 5 hours) of InAlN/GaN HEMTs. V_d = 0.05 V during the noise measurements.

6.3 Conclusions

Temperature dependent noise measurements identify prominent traps at ~ 0.7 eV as N_{Ga} anti-site defects, which are acceptor-like defects. Traps at ~ 0.2 eV to ~ 0.4 eV are identified as O_N-related impurity complexes, which are donor-like. O_N-related donors evidently are the dominant reliability-limiting defect in Wolfspeed CGH40010F AlGaN/GaN HEMTs. Their densities can be significantly increased by the dehydrogenation of O_N-H impurity complexes during ON-bias stress, which evidently is the reliability-limiting mechanism in these devices. Gate-voltage dependent noise results of commercial-grade CGH40006P and CGH40010F GaN-based HEMTs identify that negative V_{th} shifts are due most likely to the activation of O_N defects, and positive V_{th} shifts at higher fluences are due most likely to the generation of V_N-related defects. The positive V_{th} shifts of research-grade InAlN/GaN HEMTs are due most likely to the activation of N_{Ga} anti-site defects, which are acceptor-like.

Chapter VII. Conclusions

This work focuses on the high voltage stress, radiation effects and low frequency noise of commercial and research grade GaN-based HEMTs. We test two commercial AlGaN/GaN HEMTs from Cree/Wolfspeed and one research-grade InAlN/GaN HEMTs under three bias conditions: ON, semi-ON and OFF state. 10-keV X-ray and 1.8 MeV proton irradiation response of GaN-based HEMTs is investigated. Low frequency noise was employed as a diagnostic tool to understand the nature of the defects responsible for the degradation.

Effects of hot-carrier stress at temperatures up to 125 ^{o}C are evaluated for Cree/Wolfspeed CGH40010F GaN-based HEMTs. Both donor-like and acceptor-like defects can play significant roles in the device degradation, with densities depending on stress time, temperature, and bias condition. During stepped drain-bias stress test, V_{th} shift changes from positive to negative under OFF-state stress with increasing drain bias, which indicate that multiple kinds of defects are responsible for high-field and/or high current stress induced degradation. Unlike many previous studies, the worst case for G_M degradation of these devices is ON bias condition at elevated temperatures. These results confirm that a single worst-case bias condition for voltage-stress cannot be defined for all varieties of GaN HEMTs, and that each technology must be characterized in detail. Temperature dependent low-frequency noise measurements identify prominent traps at ~ 0.7 eV as N_{Ga} anti-site defects, which are acceptor-like defects. Traps at ~ 0.2 eV to ~ 0.4 eV are identified as O_N-related defects, which are donor-like. O_N-related donors evidently are the dominant reliability-limiting defect in these devices. Their densities can be significantly increased by the

dehydrogenation of O_N-H complexes during ON-bias stress, which evidently is the reliability-limiting mechanism in these devices.

Two commercial AlGaN/GaN HEMTs from Cree/Wolfspeed show similar responses to ～10-keV X-ray irradiation and 1.8-MeV proton irradiation. Devices show negative threshold voltage shifts during 10-keV X-ray irradiation, and during proton irradiation at low fluences. These negative Vth shifts are due most likely to the activation of O_N defects, which are donor-like. Positive Vth shifts at higher fluences are due most likely to the generation of V_N-related defects, which are acceptor-like. The ionization-equivalent dose for 1.8 MeV protons at a fluence of $10^{13}/cm^2$ is much larger, ~ 20 Mrad(SiO_2). This indicates that either the rate of donor-like defect activation during the proton irradiation is lower than during ~10-keV X-ray irradiation, or that compensating acceptor-like defects are also generated during 1.8-MeV. We have investigated the combined effects of X-ray irradiation and hot carrier stress on research-grade InAlN/GaN HEMTs. Both the bias during X-ray irradiation and the application of high-field stress before X-ray exposure can significantly increase the sensitivity of InAlN/GaN HEMTs. The positive Vth shifts are due most likely to the activation of N_{Ga} anti-site defects, which are acceptor-like.

References

[1] B. J. Baliga, “Semiconductors for high-voltage, vertical channel field-effect transistors,” *J. Appl. Phys.*, vol. 53, no. 3, pp. 1759–1764, 1982.
[2] M. Bhatnagar, P. K. McLarty, and B. J. Baliga, “Silicon-carbide high-voltage (400 V) Schottky barrier diodes,” *IEEE Electron Device Lett.*, vol. 13, no. 10, pp. 501–503, Oct. 1992.
[3] D. Alok, B. Baliga, and P. McLarty, “A simple edge termination for silicon carbide devices with nearly ideal breakdown voltage,” *IEEE Electron Device Lett.,* vol. 15, no. 10, pp. 394-395, 1994.
[4] B. J. Baliga, “Critical nature of oxide/interface quality for SiC power devices,” *Microelect. Eng*., vol. 28, pp. 177-184, 1995.
[5] A. K. Agarwal, J. B. Casady, L. B. Rowland, W. F. Valek, M. H. White, and C. D. Brandt, “1.1 kV 4H–SiC power UMOSFETs,” *IEEE Electron Device Lett*., vol. 18, pp. 586–588, Dec. 1997.
[6] B. J. Baliga, “Wide Bandgap Semiconductor Power Devices: Materials, Physics, Design, and Applications,” *The Netherlands: Elsevier*, 2019.
[7] B. J. Baliga, “Power semiconductor devices having improved high frequency switching and breakdown characteristics,” *U.S. Patent 5998833*, Dec. 7, 1999.
[8] D. B. Holt and B. G. Yacobi, “Extended defects in semiconductors: electronic properties, device effects and structures,” *Cambridge University Press*, 2007.
[9] M. E. Levinshtein, S. L. Rumyantsev, and M. S. Shur, “Properties of Advanced Semiconductor Materials: GaN, AIN, InN, BN, SiC, SiGe,” *John Wiley & Sons*, 2001.
[10] J. Wu, W. Walukiewicz, W. Shan, K. Yu, J. Ager Iii, S. Li, E. Haller, H. Lu, and W. J. Schaff, “Temperature dependence of the fundamental band gap of InN,” *J. Appl. Phys.,* vol. 94, no. 7, pp. 4457-4460, 2003.
[11] Y. Hao, J. F. Zhang, and J. C. Zhang, “Nitride wide bandgap semiconductor material and electronic devices*,*” *CRC Press*, 2016.
[12] S. Dhar, and S. Ghosh, “Low field electron mobility in GaN,” *J. Appl. Phys.,* vol. 86, no. 5, pp. 2668-2676, 1999.
[13] J. Kolnik, İ. H. Oğuzman, K. F. Brennan, R. Wang, P. P. Ruden, and Y. Wang, “Electronic transport studies of bulk zincblende and wurtzite phases of GaN based on an ensemble Monte Carlo calculation including a full zone band structure,” *J. Appl. Phys.,* vol. 78, no. 2, pp. 1033-1038, 1995.
[14] O. Ambacher, J. Smart, J. Shealy, N. Weimann, K. Chu, M. Murphy, W. Schaff, L. Eastman, R. Dimitrov, and L. Wittmer, “Two-dimensional electron gases induced by spontaneous and piezoelectric polarization charges in N-and Ga-face AlGaN/GaN heterostructures,” *J. Appl. Phys.,* vol. 85, no. 6, pp. 3222-3233, 1999.
[15] M. Stutzmann, O. Ambacher, M. Eickhoff, U. Karrer, A. Lima Pimenta, R. Neuberger, J. Schalwig, R. Dimitrov, P. Schuck, and R. Grober, “Playing with polarity,” *Phys. Statist. Solidi (b),* vol. 228, no. 2, pp. 505-512, 2001.

[16] G. Martin, A. Botchkarev, A. Rockett, and H. Morkoc, "Valence-band discontinuities of wurtzite GaN, AlN, and InN heterojunctions measured by x-ray photoemission spectroscopy," *Appl. Phys. Lett.,* vol. 68, no. 18, pp. 2541-2543, 1996.
[17] F. Bernardini, V. Fiorentini, and D. Vanderbilt, "Spontaneous polarization and piezoelectric constants of III-V nitrides," *Physical Review B,* vol. 56, no. 16, pp. R10024, 1997.
[18] E. F. Schubert, T. Gessmann, and J. K. Kim, "Light emitting diodes," *Kirk-Othmer Encyclopedia of Chemical Technology*, 2000.
[19] R. Dingle, H. Störmer, A. Gossard, and W. Wiegmann, "Electron mobilities in modulation-doped semiconductor heterojunction superlattices," *Appl. Phys. Lett.,* vol. 33, no. 7, pp. 665-667, 1978.
[20] T. Mimura, K. Joshin, S. Hiyamizu, K. Hikosaka, and M. Abe, "High electron mobility transistor logic," *Jpn. J. Appl. Phys.,* vol. 20, no. 8, pp. L598, 1981.
[21] T. Mimura, "The early history of the high electron mobility transistor (HEMT)," *IEEE Trans. Microw. Theory Techn.,* vol. 50, no. 3, pp. 780-782, 2002.
[22] T. Mimura, "Development of high electron mobility transistor," *Jpn. J. Appl. Phys.,* vol. 44, no. 12R, pp. 8263, 2005.
[23] M. A. Khan, A. Bhattarai, J. Kuznia, and D. Olson, "High electron mobility transistor based on a GaN-$Al_xGa_{1-x}N$ heterojunction," *Appl. Phys. Lett.,* vol. 63, no. 9, pp. 1214-1215, 1993.
[24] H. Xing, S. Keller, Y. Wu, L. McCarthy, I. Smorchkova, D. Buttari, R. Coffie, D. Green, G. Parish, and S. Heikman, "Gallium nitride based transistors," *J. Appl. Phys.: Condensed Matter,* vol. 13, no. 32, pp. 7139, 2001.
[25] D. Nirmal and J. Ajayan, "Handbook for III-V High Electron Mobility Transistor Technologies, " *CRC Press*, 2019.
[26] I. Smorchkova, C. Elsass, J. Ibbetson, R. Vetury, B. Heying, P. Fini, E. Haus, S. DenBaars, J. Speck, and U. Mishra, "Polarization-induced charge and electron mobility in AlGaN/GaN heterostructures grown by plasma-assisted molecular-beam epitaxy," *J. Appl. Phys.,* vol. 86, no. 8, pp. 4520-4526, 1999.
[27] G. Koley, and M. Spencer, "Surface potential measurements on GaN and AlGaN/GaN heterostructures by scanning Kelvin probe microscopy," *J. Appl. Phys,* vol. 90, no. 1, pp. 337-344, 2001.
[28] O. Katz, D. Mistele, B. Meyler, G. Bahir, and J. Salzman, "InAlN/GaN heterostructure field-effect transistor DC and small-signal characteristics," *Electron. Lett.,* vol. 40, no. 20, pp. 1304-1305, 2004.
[29] M. Gonschorek, J. F. Carlin, E. Feltin, M. Py, and N. Grandjean, "High electron mobility lattice-matched AIInN/GaN field-effect transistor heterostructures," *Appl. Phys. Lett.,* vol. 89, no. 6, pp. 062106, 2006.
[30] K. Jeganathan, M. Shimizu, H. Okumura, Y. Yano, and N. Akutsu, "Lattice-matched InAlN/GaN two-dimensional electron gas with high mobility and sheet carrier density by plasma-assisted molecular beam epitaxy," *J. Cryst. Growth,* vol. 304, no. 2, pp. 342-345, 2007.
[31] C. Gaquiere, F. Medjdoub, J. F. Carlin, S. Vandenbrouck, E. Delos, E. Feltin, N. Grandjean, and E. Kohn, "AlInN/GaN a suitable HEMT device for extremely high power high frequency applications," in *Proc. IEEE/MTT-S Int. Microw. Symp.*, pp. 2145–2148, 2007.

[32] D. S. Lee, B. Lu, M. Azize, X. Gao, S. Guo, D. Kopp, P. Fay, and T. Palacios, "Impact of GaN channel scaling in InAlN/GaN HEMTs," in *IEDM Tech. Dig.,* pp. 457–460, Dec. 2011.
[33] Y. Yue, Z. Hu, J. Guo, B. Sensale-Rodriguez, G. Li, R. Wang, F. Faria, T. Fang, B. Song, and X. Gao, "InAlN/AlN/GaN HEMTs with regrown ohmic contacts and f_T of 370 GHz," *IEEE Electron Device Lett.,* vol. 33, no. 7, pp. 988-990, 2012.
[34] R. J. Trew, Y. Liu, W. W. Kuang, and G. L. Bilbro, "The physics of reliability for high voltage AlGaN/GaN HFETs," in *Proc. IEEE Compound Semicond. Integr. Circuit Symp.*, pp. 103–106, 2006.
[35] J. Joh, L. Xia, and J. A. del Alamo, "Gate current degradation mechanisms of GaN high electron mobility transistors," in *IEDM Tech. Dig*., pp. 385–388, 2007.
[36] J. L Jimenez and U. Chowdhury, "X-band GaN FET reliability," *IEEE Int. Reliability Phys. Symp. Dig*., pp. 429-435, 2008.
[37] J. L. Barth, C. Dyer, and E. Stassinopoulos, "Space, atmospheric, and terrestrial radiation environments," *IEEE Trans. Nucl. Sci.,* vol. 50, no. 3, pp. 466-482, 2003.
[38] J. R. Schwank, M. R. Shaneyfelt, D. M. Fleetwood, J. A. Felix, P. E. Dodd, P. Paillet, and V. Ferlet-Cavrois, "Radiation effects in MOS oxides," *IEEE Trans. Nucl. Sci.,* vol. 55, no. 4, pp. 1833-1853, 2008.
[39] D. M. Fleetwood, "Total ionizing dose effects in MOS and low-dose-rate-sensitive linear-bipolar devices," *IEEE Trans. Nucl. Sci.,* vol. 60, no. 3, pp. 1706-1730, 2013.
[40] D. M. Fleetwood, "Evolution of total ionizing dose effects in MOS devices with Moore's law scaling," *IEEE Trans. Nucl. Sci.,* vol. 65, no. 8, pp. 1465-1481, 2017.
[41] C. W. Wang, B. S. Soong, J. Y. Chen, C. L. Chen, and Y. K. Su, "Effects of gamma-ray irradiation on the microstructural and luminescent properties of radio-frequency magnetron-sputtered GaN thin films," *J. Appl. Phys.,* vol. 88, no. 11, pp. 6355-6358, 2000.
[42] B. Luo, J. Johnson, F. Ren, K. Allums, C. Abernathy, S. Pearton, A. Dabiran, A. Wowchack, C. Polley, and P. Chow, "Influence of ^{60}Co γ-rays on dc performance of AlGaN/GaN high electron mobility transistors," *Appl. Phys. Lett.,* vol. 80, no. 4, pp. 604-606, 2002.
[43] X. Hu, B. K. Choi, H. J. Barnaby, D. M. Fleetwood, R. D. Schrimpf, S. Lee, S. Shojah-Ardalan, R. Wilkins, U. K. Mishra, and R. W. Dettmer, "The energy dependence of proton-induced degradation in AlGaN/GaN high electron mobility transistors," *IEEE Trans. Nucl. Sci.,* vol. 51, no. 2, pp. 293-297, 2004.
[44] N. E. Ives, J. Chen, A. F. Witulski, R. D. Schrimpf, D. M. Fleetwood, R. W. Bruce, M. W. McCurdy, E. X. Zhang, and L. W. Massengill, "Effects of proton-induced displacement damage on gallium nitride HEMTs in RF power amplifier applications," *IEEE Trans. Nucl. Sci.,* vol. 62, no. 6, pp. 2417-2422, 2015.
[45] X. Sun, O. I. Saadat, J. Chen, E. X. Zhang, S. Cui, T. Palacios, D. M. Fleetwood, and T. P. Ma, "Total-ionizing-dose radiation effects in AlGaN/GaN HEMTs and MOS-HEMTs," *IEEE Trans. Nucl. Sci.,* vol. 60, no. 6, pp. 4074-4079, 2013.
[46] S. Wood, N. Doyle, J. Spitznagel, W. Choyke, R. More, J. McGruer, and R. Irwin, "Simulation of radiation damage in solids," *IEEE Trans. Nucl. Sci.,* vol. 28, no. 6, pp. 4107-4112, 1981.
[47] J. Srour, C. J. Marshall, and P. W. Marshall, "Review of displacement damage effects in silicon devices," *IEEE Trans. Nucl. Sci.,* vol. 50, no. 3, pp. 653-670, 2003.

[48] P. Wang, C. J. Perini, A. O'Hara, H. Gong, P. Wang, E. X. Zhang, M. W. McCurdy, D. M. Fleetwood, R. D. Schrimpf, and S. T. Pantelides, "Total Ionizing Dose Effects and Proton-Induced Displacement Damage on MoS_2-Interlayer-MoS_2 Tunneling Junctions," *IEEE Trans. Nucl. Sci.,* vol. 66, no. 1, pp. 420-427, 2018.
[49] H. Gong, W. Liao, E. X. Zhang, A. L. Sternberg, M. W. McCurdy, J. L. Davidson, R. A. Reed, D. M. Fleetwood, R. D. Schrimpf, and P. D. Shuvra, "Proton-induced displacement damage and total-ionizing-dose effects on silicon-based MEMS resonators," *IEEE Trans. Nucl. Sci.,* vol. 65, no. 1, pp. 34-38, 2017.
[50] P. F. Wang, E. X. Zhang, K. H. Chuang, W. Liao, H. Gong, P. Wang, C. N. Arutt, K. Ni, M. McCurdy, and I. Verbauwhede, E. Bury, D. Linten, D. M. Fleetwood, R. D. Schrimpf, and R. A. Reed, "X-ray and proton radiation effects on 40 nm CMOS physically unclonable function devices," *IEEE Trans. Nucl. Sci.,* vol. 65, no. 8, pp. 1519-1524, 2018.
[51] B. D. White, M. Bataiev, S. H. Goss, X. Hu, A. Karmarkar, D. M. Fleetwood, R. D. Schrimpf, W. J. Schaff, and L. J. Brillson, "Electrical, spectral, and chemical properties of 1.8 MeV proton irradiated AlGaN/GaN HEMT structures as a function of proton fluence," *IEEE Trans. Nucl. Sci.,* vol. 50, no. 6, pp. 1934-1941, 2003.
[52] J. F. Ziegler, "The stopping and ranges of ions in matter, " *Elsevier*, 2013.
[53] H. D. Xiong, "Low frequency noise and charge trapping in MOSFETs," PhD. dissertation, Vanderbilt University, Nashville, TN, 2004.
[54] J. H. Scofield, T. P. Doerr, and D. M. Fleetwood, "Correlation between preirradiation 1/f noise and postirradiation oxide-trapped charge in MOS transistors," *IEEE Trans. Nucl. Sci.,* vol. 36, no. 6, pp. 1946-1953, 1989.
[55] T. L. Meisenheimer, and D. M. Fleetwood, "Effect of radiation-induced charge on 1/f noise in MOS devices," *IEEE Trans. Nucl. Sci.,* vol. 37, no. 6, pp. 1696-1702, 1990.
[56] D. M. Fleetwood, T. L. Meisenheimer, and J. H. Scofield, "1/*f* noise and radiation effects in MOS devices," *IEEE Transactions on Electron Devices,* vol. 41, no. 11, pp. 1953-1964, 1994.
[57] P. Dutta, and P. M. Horn, "Low-frequency fluctuations in solids: 1/*f* noise," *Reviews of Modern physics,* vol. 53, no. 3, pp. 497, 1981.
[58] H. Kim *et al*., "Reliability evaluation of high power AlGaN/GaN HEMTs on SiC substrate," *Phys. Stat. Sol. A*, vol. 188, no. 1, pp. 203–206, Nov. 2001.
[59] T. Palacios *et al*., "High-power AlGaN/GaN HEMTs for Ka-band applications," *IEEE Trans. Electron Devices*, vol. 26, pp. 781–783, 2005.
[60] Y. Ohno and M. Kuzuhara, "Application of GaN-based heterojunction FETs for advanced wireless communication," *IEEE Trans. Electron Devices,* vol. 48, pp. 517–523, Mar. 2001.
[61] F. Husna, M. Lachab, M. Sultana, V. Adivarahan, Q. Fareed, and A. Khan, "High-temperature performance of AlGaN/GaN MOSHEMT with SiO_2 gate insulator fabricated on Si (111) substrate," *IEEE Trans. Electron Devices*, vol. 59, no. 9, pp. 2424–2429, Sept 2012.
[62] J. Joh and J. A. Del Alamo, "Mechanisms for electrical degradation of GaN high-electron mobility transistors," *IEDM Tech Dig*., pp. 148–151, 2006.

[63] G. Meneghesso *et al.*, “Reliability of GaN high-electron-mobility transistors: State of the art and perspectives,” *IEEE Trans. Device Mater. Reliab.*, vol. 8, pp. 332–343, 2008.

[64] T. Roy *et al.*, “Temperature-dependence and microscopic origin of low frequency 1/*f* noise in GaN/AlGaN high electron mobility transistors,” *Appl. Phys. Lett.*, vol. 99, no. 20, 2011, Art. no. 203501.

[65] R. Jiang *et al.*, “Multiple defects cause degradation after high field stress in AlGaN/GaN HEMTs,” *IEEE Trans. Device Mater. Rel*., vol. 18, no. 3, pp. 364–376, Sep. 2018.

[66] J. Chen *et al*., “Effects of applied bias and high field stress on the radiation response of GaN/AlGaN HEMTs,” *IEEE Trans. Nucl. Sci*., vol. 62, no. 6, pp. 2423–2430, Dec. 2015.

[67] J. Chen *et al*., “High-field stress, low-frequency noise, and long-term reliability of AlGaN/GaN HEMTs,” *IEEE Trans. Device Mater. Rel*., vol. 16, no. 3, pp. 282–289, Sep. 2016.

[68] Y. S. Puzyrev *et al*., “Dehydrogenation of defects and hot-electron degradation in GaN high-electron-mobility transistors,” *J. Appl. Phys*., vol. 109, no. 3, 2011, Art. no. 034501.

[69] S. Mukherjee, Y. Puzyrev, J. Chen , D. M. Fleetwood, R. D. Schrimpf, and S. T. Pantelides, “Hot-carrier degradation in GaN HEMTs due to substitutional iron and its complexes,” *IEEE Trans. Electron Devices*, vol. 63, no. 4, pp. 1486-1494, Apr. 2016.

[70] S. Arulkumaran, T. Egawa, H. Ishikawa, and T. Jimbo, “High-temperature effects of AlGaN/GaN high-electron-mobility transistors on sapphire and semi-insulating SiC substrates,” *Appl. Phys. Lett.*, vol. 80, pp. 2186–2188, Mar. 2002.

[71] R. Gaska, A. Osinsky, J. W. Yang, and M. S. Shur, “Self-heating in high-power AlGaN-GaN HFETs,” *IEEE Electron Device Lett.*, vol. 19, no. 3, pp. 89–91, Mar. 1998.

[72] K. S. Yuk, G. R. Branner, and D. J. McQuate, “A wideband multiharmonic empirical large-signal model for high-power GaN HEMTs with self-heating and charge-trapping effects,” *IEEE Trans. Microw. Theory Techn.*, vol. 57, no. 12, pp. 3322–3332, Dec. 2009.

[73] S. Martin-Horcajo *et al*., “Impact of device geometry at different ambient temperatures on the self-heating of GaN-based HEMTs,” *Semicond. Sci. Technol*., vol. 29, no. 11, article no. 115013, Nov. 2014.

[74] D. A. Gajewski *et al*.,“Reliability comparison of 28 V-50 V GaN-on-SiC S-band and X-band technologies,” *Microelectron. Reliab*., vol. 84, no. 5, pp. 1-6, May 2018.

[75] F. Al-Neama, N. Kapur, J. Summers, and H. M. Thompson, “Thermal management of GaN HEMT devices using serpentine minichannel heat sinks,” *Applied Thermal Engineering*, vol. 140, pp. 622-636, July 2018.

[76] J. Chen *et al*., “Proton-induced dehydrogenation of defects in AlGaN/GaN HEMTs,” *IEEE Trans. Nucl. Sci*., vol. 60, no. 6, pp. 4080–4086, Dec. 2013.

[77] Z. Q. Fang, D. C. Look, J. Jasinski, M. Benamara, Z. Liliental-Weber, and R. J. Molnar, “Evolution of deep centers in GaN grown by hydride vapor phase epitaxy,” *Appl. Phys. Lett*., vol. 78, pp. 332–334, 2001.

[78] G. Meneghesso, F. Rampazzo, P. Kordos, G. Verzellesi, and E. Zanoni, "Current collapse and high-electric-field reliability of unpassivated GaN/AlGaN/GaN HEMTs," *IEEE Trans. Electron Devices*, vol. 53, no. 12, pp. 2932–2941, Dec. 2006.
[79] Y. Puzyrev *et al.*, "Gate bias dependence of defect-mediated hot-carrier degradation in GaN HEMTs," *IEEE Trans. Electron Devices*, vol. 61, no. 5, pp. 1316–1320, May 2014.
[80] J. Joh and J. A. del Alamo, "Critical voltage for electrical degradation of GaN high-electron mobility transistors," *IEEE Electron Device Lett*., vol. 29, no. 4, pp. 287–289, Apr. 2008.
[81] P. F. Wang, X. Li, E. X. Zhang, R. Jiang, M. W. McCurdy, B. S. Poling, E. R. Heller, R. D. Schrimpf, and D. M. Fleetwood, "Worst-case bias for high voltage, elevated-temperature stress of AlGaN/GaN HEMTs," *IEEE Trans. Device Mater. Rel.*, vol. 20, no. 2, pp. 420-428, Jun. 2020.
[82] A. Kalavagunta *et al*., "Electrostatic mechanisms responsible for device degradation in proton irradiated AlGaN/AlN/GaN HEMTs," *IEEE Trans. Nucl. Sci.,* vol. 55, no. 4, pp. 2106–2112, Aug. 2008.
[83] A. Ortiz-Conde, F. J. García Sánchez, J. J. Liou, A. Cerdeira, M. Estrada, and Y. Yue, "A review of recent MOSFET threshold voltage extraction methods," *Microelectron. Reliab*., vol. 42, no. 4/5, pp. 583–596, Apr. 2002.
[84] A. Y. Polyakov, S. J. Pearton, P. Frenzer, F. Ren, L. Liu, and J. Kim, "Radiation effects in GaN materials and devices," *J. Mater. Chem. C,* vol. 1, p. 877, Sep. 2013.
[85] L. Liu *et al*., "Dependence on proton energy of degradation of AlGaN/GaN high electron mobility transistors," *J. Vac. Sci. Technol. B*, vol. 31, no. 2, p. 022201, Mar. 2013.
[86] A. P. Karmarkar *et al.*, "Proton irradiation effects on GaN-based high electron mobility transistors with Si-doped $Al_xGa_{1-x}N$ and thick GaN cap layers," *IEEE Trans. Nucl. Sci*., vol. 51, no. 6, pp. 3801–3806, Dec. 2004.
[87] Y. S. Puzyrev, T. Roy, E. X. Zhang, D. M. Fleetwood, R. D. Schrimpf, and S. T. Pantelides, "Radiation-induced defect evolution and electrical degradation of AlGaN/GaN high-electron-mobility transistors," *IEEE Trans. Nucl. Sci*., vol. 58, no. 6, pp. 2918–2924, Dec. 2011.
[88] R. Jiang *et al*., "Worst-case bias for proton and 10-keV X-ray irradiation of AlGaN/GaN high electron mobility transistors," *IEEE Trans. Nucl. Sci*., vol. 64, no. 1, pp. 218–225, Jan. 2017.
[89] K. Mukherjee, F. Darracq, A. Curutchet, N. Malbert, and N. Labat, "TCAD simulation capabilities towards gate leakage current analysis of advanced AlGaN/GaN HEMT devices," *Microelectron. Rel*., vols. 76–77, pp. 350–356, Sep. 2017.
[90] Y. Gao, W. A. Sasangka, C. V. Thompson, and C. L. Gan, "Effects of forward gate bias stressing on the leakage current of AlGaN/GaN high electron mobility transistors, " *Microelectron. Rel.*, vols. 100-101, 113432, Sep. 2019.
[91] M. Ruzzarin *et al.*, "Degradation mechanisms of GaN HEMTs with p-type gate under forward gate bias overstress," *IEEE Trans. Electron Devices*, vol. 65, no. 7, pp. 2778–2783, Jul. 2018.
[92] D. Marcon *et al*., "Reliability analysis of permanent degradations on AlGaN/GaN HEMTs," *IEEE Trans. Electron Devices*, vol. 60, no. 10, pp. 3132–3141, Oct. 2013.

[93] S. Turuvekere, N. Karumuri, A. A. Rahman, A. Bhattacharya, A. DasGupta, and N. DasGupta, “Gate leakage mechanisms in AlGaN/GaN and AlInN/GaN HEMTs: Comparison and modeling,” *IEEE Trans. Electron Devices*, vol. 60, no. 10, pp. 3157–3165, Oct. 2013.
[94] J. Kotani, A. Yamada, T. Ishiguro, S. Tomabechi, and N. Nakamura, “Direct observation of nanometer-scale gate leakage paths in AlGaN/ GaN and InAlN/AlN/GaN HEMT structures,” *Phys. Status Solidi A*, vol. 213, no. 4, pp. 883–888, 2016.
[95] J. Ren *et al*., “Hot electrons induced degradation in lattice-matched InAlN/GaN high electron mobility transistors,” *Microelectron. Rel*., vol. 56, pp. 34–36, Jan. 2016.
[96] D. Yan, J. Ren, G. Yang, S. Xiao, X. Gu, and H. Lu, “Surface acceptor-like trap model for gate leakage current degradation in lattice-matched InAlN/GaN HEMTs,” *IEEE Electron Device Lett*., vol. 36, no. 12, pp. 1281–1283, Dec. 2015.
[97] J. Kuzmik, “Power electronics on InAlN/(In) GaN: Prospect for a record performance,” *IEEE Electron Device Lett.*, vol. 22, no. 11, pp. 510–512, Nov. 2001.
[98] Y. Wu and J. A. del Alamo, “Electrical degradation of InAlN/GaN HEMTs operating under on conditions,” *IEEE Trans. Electron Devices*, vol. 63, no. 9, pp. 3487–3492, Sep. 2016.
[99] J. Kuzmik, A. Kostopoulos, G. Konstantinidis, J. F. Carlin, A. Georgakilas, and D. Pogany, “InAlN/GaN HEMTs: A first insight into technological optimization,” *IEEE Trans. Electron Devices*, vol. 53, no. 3, pp. 422–426, Mar. 2006.
[100] S. Petitdidier, Y. Guhel, J. L. Trolet, P. Mary, C. Gaquière, and B. Boudart, “Neutron Irradiation Effects on the Electrical Properties of Previously Electrically Stressed AlInN/GaN HEMTs,” *IEEE Trans. Nucl. Sci.*, vol. 66, no. 5, pp. 810-819, May. 2019.
[101] S. J. Pearton, R. Deist, F. Ren, L. Liu, A. Y. Polyakov, and J. Kim, “Review of radiation damage in GaN-based materials and devices,” *J. Vac. Sci. Technol. A*., vol. 31, no. 5, pp. 050801 1–050801 16, 2013.
[102] H. Y. Kim, C. F. Lo, L. Liu, F. Ren, J. Kim, and S. J. Pearton, “Proton-irradiated InAlN/GaN high electron mobility transistors at 5, 10, and 15 MeV energies,” *Appl. Phys. Lett*., vol. 100, no. 1, pp. 012107-1–012107-3, Jan. 2012.
[103] A. Ionascat-Nedelcescu, C. Carlone, A. Houdayer, H. J. von Bardeleben, J. L. Cantin, and S. Raymond, “Radiation hardness of gallium nitride,” *IEEE Trans. Nucl. Sci*., vol. 46, no. 6, pp. 2733-2738, Dec. 2002.
[104] X. Hu *et al*., “Proton-irradiation effects on AlGaN/AlN/GaN high electron mobility transistors,” *IEEE Trans. Nucl. Sci*., vol. 50, no. 6, pp. 1791–1796, Dec. 2003.
[105] T. Roy, E. X. Zhang, Y. S. Puzyrev, D. M. Fleetwood, R. D. Schrimpf, B. K. Choi, A. B. Hmelo, and S. T. Pantelides, “Process dependence of proton-induced degradation in GaN HEMTs,” *IEEE Trans. Nucl. Sci.,* vol. 57, no. 6, pp. 3060-3065, 2010.
[106] T.Roy *et al*.,“Process dependence of proton-induced degradation in GaN HEMTs,” *IEEE Trans. Nucl. Sci.*, vol. 57, no. 6, pp. 3060–3065, Dec. 2010.
[107] D. M. Fleetwood, “1/*f* noise and defects in microelectronic materials and devices,” *IEEE Trans. Nucl. Sci*., 62, no. 4, pp. 1462–1486, Aug. 2015.

[108] L. K. J. Vandamme, “Noise as a diagnostic tool for quality and reliability of electronic devices,” *IEEE Trans. Electron Dev*., vol. 41, no. 11, pp. 2176–2187, Nov. 1994.

[109] S. L. Rumyantsev *et al*., “Low-frequency noise in GaN/AlGaN heterostructure field-effect transistors at cryogenic temperatures,” *J. Appl. Phys*., vol. 92, no. 8, pp. 4726–4730, 2002.

[110] M. E. Levinshtein, S. L. Rumyantsev, R. Gaska, J. W. Yang, and M. S. Shur, “AlGaN/GaN high electron mobility field effect transistors with low 1/*f* noise,” *Appl. Phys. Lett*., vol. 73, no. 8, pp. 1089–1091, 1998.

[111] M. Gorchichko, Y. Cao, E. X. Zhang, D. Yan, H. Gong, S. E. Zhao, P. Wang, R. Jiang, C. Liang, and D. M. Fleetwood, “Total-ionizing-dose effects and low-frequency noise in 30-nm gate-length bulk and SOI FinFETs with SiO_2/HfO_2 gate dielectrics,” *IEEE Trans. Nucl. Sci.,* vol. 67, no. 1, pp. 245-252, 2019.

[112] C. Liang, R. Ma, Y. Su, A. O’Hara, E. Zhang, M. Alles, P. Wang, S. Zhao, S. Pantelides, and S. J. Koester, “Defects and low-frequency noise in irradiated black phosphorus MOSFETs with HfO_2 gate dielectrics,” *IEEE Trans. Nucl. Sci.,* vol. 65, no. 6, pp. 1227-1238, 2018.

[113] S. E. Zhao, R. Jiang, E. X. Zhang, W. Liao, C. Liang, D. M. Fleetwood, R. D. Schrimpf, R. A. Reed, D. Linten, and J. Mitard, “Capacitance–frequency estimates of border-trap densities in multifin MOS capacitors,” *IEEE Trans. Nucl. Sci.,* vol. 65, no. 1, pp. 175-183, 2017.

[114] P. Wang, C. Perini, A. O’Hara, B. R. Tuttle, E. Zhang, H. Gong, C. Liang, R. Jiang, W. Liao, and D. Fleetwood, “Radiation-induced charge trapping and low-frequency noise of graphene transistors,” *IEEE Trans. Nucl. Sci.,* vol. 65, no. 1, pp. 156-163, 2017.

[115] G. X. Duan, J. A. Hachtel, E. X. Zhang, C. X. Zhang, D. M. Fleetwood, R. D. Schrimpf, R. A. Reed, J. Mitard, D. Linten, and L. Witters, “Effects of negative-bias-temperature-instability on low-frequency noise in SiGe *p* MOSFETs,” *IEEE Trans. Device Mater. Rel.,* vol. 16, no. 4, pp. 541-548, 2016.

[116] K. Li, E. X. Zhang, M. Gorchichko, P. F. Wang, M. Reaz, S. E. Zhao, G. Hiblot, S. Van Huylenbroeck, A. Jourdain, and M. L. Alles, “Impacts of through-silicon vias on total-ionizing-dose effects and low-frequency noise in FinFETs,” *IEEE Trans. Nucl. Sci*., 2021.

[117] S. Bonaldo, S. E. Zhao, A. O’Hara, M. Gorchichko, E. X. Zhang, S. Gerardin, A. Paccagnella, N. Waldron, N. Collaert, and V. Putcha, “Total-ionizing-dose effects and low-frequency noise in 16-nm InGaAs FinFETs with HfO_2/Al_2O_3 dielectrics,” *IEEE Trans. Nucl. Sci.,* vol. 67, no. 1, pp. 210-220, 2019.

[118] D. M. Fleetwood, S. Beyne, R. Jiang, S. E. Zhao, P. Wang, S. Bonaldo, M. W. McCurdy, Z. Tõkei, I. De Wolf, K. Croes, E. X. Zhang, M. L. Alles, R. D. Schrimpf, R. A. Reed, and D. Linten, “Low-frequency noise and defects in copper and ruthenium resistors,” *Appl. Phys. Lett*., vol. 114, no. 20, May 2019, Art. no. 203501.

[119] C. X. Zhang, S. A. Francis, E. X. Zhang, D. M. Fleetwood, R. D. Schrimpf, K. F. Galloway, E. Simoen, J. Mitard, and C. Claeys, “Effect of ionizing radiation on defects and 1/*f* noise in Ge pMOSFETs,” *IEEE Trans. Nucl. Sci.,* vol. 58, no. 3, pp. 764-769, 2011.

[120] S. A. Francis, C. X. Zhang, E. X. Zhang, D. M. Fleetwood, R. D. Schrimpf, K. F. Galloway, E. Simoen, J. Mitard, and C. Claeys, "Comparison of charge pumping and $1/f$ noise in irradiated Ge pMOSFETs," *IEEE Trans. Nucl. Sci.,* vol. 59, no. 4, pp. 735-741, 2012.

[121] C. X. Zhang, E. X. Zhang, D. M. Fleetwood, R. D. Schrimpf, S. Dhar, S. H. Ryu, X. Shen, and S. T. Pantelides, "Origins of low-frequency noise and interface traps in 4H-SiC MOSFETs," *IEEE Electron Device Lett.,* vol. 34, no. 1, pp. 117-119, 2012.

[122] C. X. Zhang, X. Shen, E. X. Zhang, D. M. Fleetwood, R. D. Schrimpf, S. A. Francis, T. Roy, S. Dhar, S. H. Ryu, and S. T. Pantelides, "Temperature dependence and postirradiation annealing response of the $1/f$ noise of 4H-SiC MOSFETs," *IEEE Trans. Electron Devices,* vol. 60, no. 7, pp. 2361-2367, 2013.

[123] Y. Cai, Z. Cheng, Z. Yang, C. W. Tang, K. M. Lau, and K. J. Chen, "High-temperature operation of AlGaN/GaN HEMTs direct-coupled FET logic (DCFL) integrated circuits," *IEEE Electron Device Lett*., vol. 28, no. 5, pp. 328–331, May 2007.

[124] A. M. Darwish, B. D. Huebschman, E. Viveiros, and H. A. Hung, "Dependence of GaN HEMT millimeter-wave performance on temperature," *IEEE Trans. Microw. Theory Tech*., vol. 57, no. 12, pp. 3205–3211, Dec. 2009.

[125] A. Fontsere, A. Perez-Tomas, V. Banu, P. Godignon, J. Millan, H. De Vleeschouwer, J. M. Parsey, and P. Moens, "A HfO_2 based 800V/300°C Au-free AlGaN/GaN-on-Si HEMT technology," in *Proc. Intl. Sympos. Power Semicond. Devices ICs*, pp. 37–40, 2012.

[126] S. Yang, S. Liu, C. Liu, Y. Lu, and K. J. Chen, "Mechanisms of thermally induced threshold voltage instability in GaN-based heterojunction transistors," *Appl. Phys. Lett*., vol. 105, no. 22, article no. 223508, 2014.

[127] J. H. Scofield, N. Borland, and D. M. Fleetwood, "Reconciliation of different gate-voltage dependencies of $1/f$ noise in nMOS and pMOS transistors," *IEEE Trans. Electron Devices*, vol. 41, no. 11, 1946-1952, Dec. 1994.

[128] R. Jiang *et al*., "Degradation and annealing effects caused by oxygen in AlGaN/GaN high electron mobility transistors," *Appl. Phys. Lett*., vol. 109, no. 2, article no. 023511, 2016.

[129] C. G. de Walle and J. Neugebauer, "First-principles calculations for defects and impurities: Applications to III-nitrides," *J. Appl. Phys*., vol. 95, pp. 3851–3879, 2004.

[130] P. Wang *et al*., "$1/f$ noise in as-processed and proton-irradiated AlGaN/GaN HEMTs due to carrier number fluctuations," *IEEE Trans. Nucl. Sci*., vol. 64, no. 1, pp.181–189, Jan. 2017.